UNIVERSIDADE ESTADUAL DE CAMPINAS

Instituto de Física "Gleb Wataghin"

ANDRES FABIAN QUIROGA SOTO

Characterization of NIRS-measured hemodynamic alterations in diseases with vascular malfunction

Caracterização das alterações hemodinâmicas medidas por NIRS em doenças com comprometimento vascular

CAMPINAS

2022

ANDRES FABIAN QUIROGA SOTO

Characterization of NIRS-measured hemodynamic alterations in diseases with vascular malfunction

Caracterização das alterações hemodinâmicas medidas por NIRS em doenças com comprometimento vascular

Tese apresentada à Departamento de Raios Cósmico e Cronologias do Instituto de Física "Gleb Wataghin" da Universidade Estadual de Campinas como parte dos requisitos exigidos para a obtenção do título de Doutor em Ciências, na área de Física.

Thesis presented to the Department of Cosmic Rays and Chronology of the Institute of Physics "Gleb Wataghin" at the University of Campinas as partial fulfillment of the requirements for the degree of Doctor in Science, in the field of Physics.

Supervisor: RICKSON COELHO MESQUITA

ESTE TRABALHO CORRESPONDE À VERSÃO FINAL DA TESE DEFENDIDA PELO ALUNO ANDRES FABIAN QUIROGA SOTO, E ORIENTADA PELO PROF. DR. RICKSON COELHO MESQUITA.

Campinas

2022

Ficha catalográfica
Universidade Estadual de Campinas
Biblioteca do Instituto de Física Gleb Wataghin
Lucimeire de Oliveira Silva da Rocha - CRB 8/9174

Q48c

Quiroga Soto, Andres Fabian, 1987-
Characterization of NIRS-measured hemodynamic alterations in diseases with vascular malfunction / Andres Fabian Quiroga Soto. – Campinas, SP : [s.n.], 2022.

Orientador: Rickson Coelho Mesquita.
Tese (doutorado) – Universidade Estadual de Campinas, Instituto de Física Gleb Wataghin.

1. Doenças das artérias carótidas. 2. COVID-19. 3. Espectroscopia de infravermelho próximo. I. Mesquita, Rickson Coelho, 1982-. II. Universidade Estadual de Campinas. Instituto de Física Gleb Wataghin. III. Título.

Informações para Biblioteca Digital

Título em outro idioma: Caracterização das alterações hemodinâmicas medidas por NIRS em doenças com comprometimento vascular
Palavras-chave em inglês:
Carotid artery diseases
COVID-19 (Disease)
Near infrared spectroscopy
Área de concentração: Física
Titulação: Doutor em Ciências
Banca examinadora:
Rickson Coelho Mesquita [Orientador]
Gabriela Castellano
Mônica Alonso Cotta
Renata Ferranti Leoni
Leandro Utino Taniguchi
Data de defesa: 04-02-2022
Programa de Pós-Graduação: Física

Identificação e informações acadêmicas do(a) aluno(a)
- ORCID do autor: https://orcid.org/0000-0002-3846-0761
- Currículo Lattes do autor: http://lattes.cnpq.br/1886510025147813

MEMBROS DA COMISSÃO JULGADORA DA TESE DE DOUTORADO DO ALUNO ANDRES FABIAN QUIROGA SOTO - RA 153906 APRESENTADA E APROVADA AO INSTITUTO DE FÍSICA “GLEB WATAGHIN”, DA UNIVERSIDADE ESTADUAL DE CAMPINAS, EM 04/02/2022.

COMISSÃO JULGADORA:

- Prof. Dr. Rickson Coelho Mesquita - Presidente e Orientador (IFGW / UNICAMP)

- Profa. Dra. Gabriela Castellano (IFGW / UNICAMP)

- Profa. Dra. Mônica Alonso Cotta (IFGW/ UNICAMP

- Dra. Renata Ferranti Leoni (FFCLRP/USP)

- Dr. Leandro Utino Taniguchi (HOSPITAL DAS CLÍNICAS DA FACULDADE DE MEDICINA DA USP)

OBS.: Ata da defesa com as respectivas assinaturas dos membros encontra-se no SIGA/Sistema de Fluxo de Dissertação/Tese e na Secretaria do Programa da Unidade.

CAMPINAS

2022

Viva a ciência na América Latina!

¡Que viva la ciencia en América Latina!

Long live science in Latin America!

Absorving and scattering knowledge!

Acknowledgements

The persons and institutions I will be acknowledging transcend countries and languages.

Quiero comenzar agradeciendo a mi madre, Marina, e a mi difunto padre, Hernán, por todo el sacrificio y esfuerzo que tuvierón conmigo e que permitió aprender el valor de esas palabras. A mis hermanos, Jessica, Karen, Marta, Leonardo, Elizabeth, Jairo e Deyvi por incentivarme y apoyarme siempre. A Carmenza y a la señora Marina por los consejos de vida.

Agradeço ao universo por me dar a oportunidade de compartilhar os últimos anos com umas das pessoas mais maravilhosas da minha vida, ela é a minha companheira, parceira e esposa, Karina, quero te agradecer pelo carinho, paciência e aprendizado que você me fornece dia a dia. Também me sinto muito grato por meus sogros, Raimunda e Jorge, que me adotaram como mais um membro da família.

Quiero también agradecer a mis grandes amigos Emmanuel, John, Pedro, Cesar y Daniel por ser modelos de inspiración, compañerismo y apoyo constante.

Um profundo agradecimento ao meu orientador Rickson, por ter acreditado em mim, ter me incentivado a melhorar, e ter contribuido na minha formação nestes últimos 7 anos. Você é uma inspiração. Me sinto orgulhoso de ter feito parte do LOB (laboratório de óptica biomédica). Neste lugar vivenciei os maiores aprendizados que tiveram influência neste trabalho. Agradeço Alex pela mais sincera amizade, Sérgio pelas excelentes discussões, Edwin pelas indicações precisas, Giovani G. pela ajuda indispensável, Giovanni H. pela fantástica colaboração, Rodrigo pelo grandioso suporte. Também, aproveito para destacar outros membros do LOB que tiveram uma colaboração direta nesta pesquisa. Quero dar um profundo agradecimento a Luis Felipe pela ajuda nas análises

de conectividade, a Vinícius R. e Luiz S. pela ajuda nas coletas de dados, a Vinicius e Adriana pela ajuda com o desenvolvimento do banco de dados e design da plataforma web.

Agradeço ao pessoal do Hospital das Clínicas da UNICAMP e USP pelas colaborações de pesquisa, destaco a colaboração da Prof. Ana Terezinha e Prof. Wagner que habilitaram acesso aos pacientes de estenose de carótida. A Lígia e sua equipe, como também a Leandro pelas coletas dos pacientes com COVID-19.

I also want to express my gratitude to the HEMOCOVID-19 project for creating and funding the optical devices used to monitor COVID-19 patients.

Finalizo meus agradecimentos afirmando que o presente trabalho foi realizado com apoio da Coordenação de Aperfeiçoamento de Pessoal de Nível Superior - Brasil (CAPES) - Código de Financiamento 001.

Abstract

Some diseases can affect the function of the vascular system at different levels, resulting in dysfunction of the heart, the vasculature, or the endothelium cells. Among several examples, carotid artery atherosclerosis is a vascular disease with consequences in cerebral hemodynamics that few understand; COVID-19 is a viral disease that impacts endothelial cell function. The impact of carotid stenosis and COVID-19 on microvascular hemodynamics cannot be assessed using current standard clinical procedures. On the other hand, near-infrared spectroscopy (NIRS) can noninvasively monitor hemodynamics at the microvascular level by measuring variations in absorption resulting from changes in oxy- and deoxy-hemoglobin concentrations. In this work, we used NIRS to assess microvascular reactivity in both carotid atherosclerosis and COVID-19 independently. In the first part of this work, we quantified the time delay in response to a breath-holding test across different brain regions in patients diagnosed with carotid stenosis to show that severe bilateral patients have a restricted and slower response to vasodilation. Furthermore, by correlating the fNIRS signal during the resting state across brain regions, we found that these patients have more densely connected oxygen extraction networks than controls. In COVID-19 patients, the oxygenation curve measured with NIRS during a vascular reactivity test was sensitive to oxygen consumption and endothelial disfunction that appear to be correlated with the severity of the disease. Overall, this work provides evidence that NIRS measures can offer insightful information for understanding the interplay between local blood oxygen supply and demand at the microvasculature, which can be valuable to clinically monitor several diseases that directly or indirectly cause microvascular impairments.

Keywords: near-infrared spectroscopy, carotid atherosclerosis, COVID-19, vascular reactivity.

Resumo

Algumas doenças podem afetar a função do sistema vascular em diferentes níveis, resultando em disfunção do coração, dos vasos sanguíneos ou das células endoteliais. Entre vários exemplos, a aterosclerose da artéria carótida é uma doença vascular com consequências na hemodinâmica cerebral que poucos compreendem, enquanto a COVID-19 afeta a função das células endoteliais. Atualmente, o impacto da estenose de carótida e da COVID-19 na hemodinâmica microvascular não pode ser avaliado usando os procedimentos clínicos padrão. Por outro lado, a espectroscopia no infravermelho próximo (NIRS) é capaz de medir a hemodinâmica microvascular de forma não invasiva a partir das variações na absorção resultantes de alterações nas concentrações de oxi e desoxi-hemoglobina. Neste trabalho, usamos a NIRS para avaliar a reatividade microvascular na aterosclerose de carótida e no COVID-19 de forma independente. Na primeira parte deste trabalho, quantificamos o atraso na resposta hemodinâmica a um teste de apneia em diferentes regiões do cérebro em pacientes diagnosticados com estenose carotídea para mostrar que pacientes bilaterais graves têm uma resposta restrita e mais lenta à vasodilatação. Além disso, ao correlacionar o sinal de fNIRS durante o estado de repouso em todas as regiões do cérebro, descobrimos que esses pacientes têm redes de extração de oxigênio mais densamente conectadas do que os controles. Em pacientes com COVID-19, a curva de oxigenação medida com NIRS durante um teste de reatividade vascular foi sensível ao consumo de oxigênio e à disfunção endotelial que parecem estar correlacionados com a gravidade da doença. No geral, este trabalho fornece evidências de que as medidas de NIRS podem oferecer informações relevantes para entender a interação entre a oferta local de oxigênio no sangue e a demanda na microvasculatura, o que pode ser valioso para monitorar clinicamente várias doenças que causam danos microvasculares direta ou indiretamente.

Palavras-chave: NIRS, aterosclerose de carótida, COVID-19, reatividade vascular.

List of Figures

List of Tables

Contents

Chapter 1

Introduction

Our body is composed of approximately 37 trillion cells [1], each of which is the smallest unit capable of sustaining life. They are vital for our biological tissues and are required for life to exist. Cells store and release energy by converting adenosine triphosphate (ATP) molecules to adenosine diphosphate (ADP) molecules and vice-versa. Cells preferentially produce ATP through glucose oxidation since they get most ATP using the Krebs cycle in the mitochondria, which requires oxygen. The sequence of chemical processes related to energy in the cell is called cellular metabolism, and a continuous supply of oxygen is needed to create sufficient energy for life.

It is highly challenging to provide adequate oxygen for dozens of trillion cells. As a result, nature found that the most effective oxygen delivery method is through the combination of the respiratory and circulatory systems. The respiratory system takes oxygen from the air and makes it available inside the lungs. Oxygen in the lungs binds to hemoglobin molecules in the blood, and the heart pumps the oxygenated blood to the capillary regions, ultimately releasing the oxygen to local tissues based on the cells' metabolic demand.

Finally, the deoxygenated blood returns to the heart and lungs to restart the cycle. Other important roles of the cardiovascular system include defending against invading microorganisms, controlling body temperature, and cleaning bioproducts.

Maintaining an appropriate oxygen supply at the tissues involves coordinated action. The circulatory system uses several mechanisms to regulate blood flow and deliver sufficient oxygen across all body regions. Two factors support this coordination: systemic regulation and local regulation. The systemic regulation is related to hemodynamic oscillations from different origins ranging from low-frequency oscillations of arterial pressure and respiration to fast oscillations of the cardiac cycle and heart rate. These oscillations are associated with the sympathetic system that produces fluctuations in the vascular tone caused by baroreflex effects [2]. On the other hand, local regulation occurs through changes in the inner diameter of the vasculature to keep the blood flow relatively constant (vasoreactivity) [3]. The vasoreactivity response can be triggered by four different mechanisms: myogenic (smooth muscle stretching) [4], metabolic (the synthesis of waste vasodilators) [5], endothelial (the release of oxygen nitric oxide) [6], and oxygen-linked (gradient of partial pressure oxygen) [7]. Our health is seriously affected whenever any of these protection mechanisms is compromised.

Vascular diseases can directly impact arteries, veins, vessels, blood flow, or autoregulation at several levels, resulting in various complications that can lead to mortality [8]. Although cardiovascular diseases do not catch attention from the media [9], they are the first cause of death worldwide according to the World Health Organization and killed 17.9 million people in 2019, which corresponded to 32% of all annual fatalities. Among the several cardiovascular diseases, heart attack and stroke were responsible for around 85% of these deaths [10]. Stroke survivors frequently present some irreversible incapacity which impacts countries on a large scale, both socially and economically. From 2005 through 2050, the overall cost of stroke in the United States is expected to be about $2 trillion [11]. Carotid stenosis is a risk factor that causes at least $15-20\%$ of all ischemic strokes, and it is estimated that $5-10\%$ of the people over 50 years of age have carotid stenosis [12]. Besides the increased risk of stroke, the hemodynamic implications of carotid stenosis remain unclear, with solid evidence that carotid stenosis leads to relevant neurodegeneration even in asymptomatic cases [13–15].

The stenosis in the carotid progressively reduces cerebral blood flow over several years and results in silent hypoperfusion due to self-regulation mechanisms that mask the brain's hemodynamic

repercussions. Several studies have attempted to better understand the hemodynamic impact of long-term carotid stenosis. The review of Dempsey et al. found that patients with carotid stenosis present cognitive impairment over time [16]; the deterioration is linked to the loss of neurons by hypoxia [17] when the cerebral protection mechanism fails to preserve the brain's integrity. We anticipate that this scenario will be difficult to examine using standard clinical procedures (vascular Doppler, angiography imaging, and positron emission tomography scan) because the hemodynamic information in these techniques originates from large arteries. The most probable scenario is that the effects of stenosis on hemodynamics first occur at the microvascular level. Hence, monitoring microvascular vasoreactivity in individuals with carotid stenosis can aid in understanding its implications.

It is genuine to assume that hemodynamic alterations are only found in vascular disorders. However, viruses can also significantly impact our vascular system, including viruses that cause respiratory infections, herpes, and HIV. The most common problem occurs when viruses infect the heart cells, producing inflammation in the myocardial (myocarditis) or pericardium (pericarditis). The high viral charge activates immunological and autoimmune mechanisms in the vascular cells that contribute to cell damage [18]. According to estimations, 1 to 5% of all individuals with severe viral infections will develop myocarditis [19]. Similarly, cells in the vascular system, such as endothelial cells, can be infected by viruses like Nipah, Hantavirus, Influenza A, H5N1, H7N1, Dengue, or Zikavirus [20].

SARS-COV-2 was an unexpected virus that appeared in 2019, which also infects the endothelium cells [21, 22], with a higher mortality rate in severe conditions related to endothelial dysfunctions such as diabetes, hypertension, and cardiovascular disease [23]. Multi-organ endothelial damage, thrombosis, inflammation, and pulmonary edema are frequent clinical symptoms in severe COVID-19 cases, which is akin to a loss of microvascular function [24]. In the microvasculature, endothelial cells perform vascular-regulating activities [6]. Therefore, it is straightforward to hypothesize that endothelial health can be assessed at the microvascular level. Monitoring the endothelium status can aid physicians in preventing adverse effects in severe COVID-19 patients or even predict the clinical outcomes.

Overall, both carotid stenosis and COVID-19 cause microvascular dysfunction, impact tissue hemodynamics and metabolism, with local implications in the microvasculature. This thesis builds on these facts and on previous studies to assess microvascular oxygen saturation with near-infrared spectroscopy and investigates how suitable optical techniques can be to provide information about the diseases mentioned above.

Near-infrared spectroscopy techniques can monitor tissue hemodynamics non-invasively at the microvascular level. This approach is based on the absorption and scattering of infrared light by tissue, which is sensitive to variations in oxy- and deoxyhemoglobin molecules found in the blood [25]. The simple implementation of the technique and its appropriate translation to the clinic makes it a potential tool for addressing vascular diseases. Therefore, this thesis proposes investigating the microvascular impairment associated with acute carotid artery stenosis and severe COVID-19 with near-infrared spectroscopy. This work aims to demonstrate that near-infrared measurements are sensitive to alterations in the microvasculature and can provide insightful information about vascular dysfunctions. We separated this work into two independent but complementary studies to address two unrelated diseases: (1) carotid artery stenosis and (2) COVID-19. Specifically, we attempted to answer the following list of questions throughout the study (1):

Q1.1 Can near-infrared spectroscopy quantify cerebral vasoreactivity?

Q1.2 How does carotid artery stenosis affect cerebral hemodynamics at the microvasculature across different regions and/or hemispheres?

Q1.3 Can the effects of carotid artery stenosis be detected at rest, without the need of disturbing the brain with a vasoreactivity test?

Q1.4 Assuming the answer to the previous questions is yes, how does carotid artery stenosis affect cerebrovascular connectivity in the brain?

Concerning our methods, near-infrared spectroscopy monitoring of the brain in individuals with carotid artery stenosis during a breath-holding protocol led to answer Q1.1. Question Q1.2 was assessed by simultaneously monitoring several brain regions. Q1.3 and Q1.4 were investigated by monitoring spontaneous oscillations of the whole head during the resting state. In all cases,

we compared the responses obtained in patients diagnosed with carotid artery stenosis with the responses measured in control subjects without the diagnosis of carotid artery stenosis.

Concerning study (2), the following questions were used to drive our research:

Q2.1 Is it possible to use near-infrared spectroscopy to assess the endothelium state in severe COVID-19 patients?

Q2.2 Is the severity of COVID-19 linked to the endothelial state, as measured by near-infrared spectroscopy?

In this case, hemodynamic monitoring of the brachioradialis muscle during a vascular occlusion test was used to evaluate question Q2.1. To address question Q2.2, we compared the hemodynamic parameters measured with near-infrared spectroscopy across patients diagnosed with COVID-19 with different degrees of severity. Again, the response of the patients was compared to the response obtained in healthy subjects under the same experimental protocol.

The details of both studies are presented in the following chapters contained in this work. The fundamental physical concepts and experimental aspects of near-infrared spectroscopy are covered in Chapter 2. The details of the study with the patients with carotid artery stenosis, the largest part of this thesis, are presented in the following three chapters. Chapter 3 introduces the research design, the recruited cohort, and our solution to manage clinical and optical data, which was unavailable in our lab before this thesis. Chapter 4 presents the results obtained during a cerebral vasoreactivity test (breath-holding) and proposes a novel approach to quantify the transit time of the brain response following a vasoreactivity test. Then, Chapter 5 investigates the cerebrovascular organization in the patients with carotid artery stenosis at rest. The assessment of patients diagnosed with COVID-19 is presented in Chapter 6, where we show the results obtained during a vascular occlusion test to assess endothelial dysfunction. Finally, Chapter 7 summarizes our observations, evaluates our results based on our initial goals, and discusses future perspectives on the use of near-infrared spectroscopy to monitor vascular diseases in the clinical setting.

Chapter 2

Near-Infrared Spectroscopy: fundamentals and practical aspects

Near-infrared spectroscopy (NIRS) is an optical technique based on the interaction of matter with low-power light in the near-infrared range of the electromagnetic spectrum (∼700–900 nm) to infer changes in its optical properties [25–28]. Light propagation is governed by the optical properties of a medium; in the case of near-infrared light in biological tissues, propagation faces low absorption and high scattering [29–32]. Consequently, the incident light is scattered multiple times in all directions, leading to a diffusion profile through the tissue [25, 33]. Eventually, it is possible to detect photons on the same plane as the incident light. Light absorption in biological tissue is strongly affected by two chromophores: oxyhemoglobin (HbO_2) and deoxyhemoglobin (HbR) present in blood [34]. Therefore, the detected photons carry information about the tissue's biomolecular composition and functional state. The sum of the HbO_2 and HbR concentrations represents the total amount of hemoglobin in the microvasculature (HbT, given by $HbT \equiv HbO_2 + HbR$). HbT is a quantity proportional to the blood volume in the sampled region. Blood oxygen saturation at the microvasculature can be estimated as the fraction of HbO_2 present in the measured blood volume (i.e., $StO_2 = HbO_2/HbT$). Without any risk, StO_2 may be measured continuously, noninvasively, and rapidly at the patient's bedside using NIRS.

NIRS relies on the following facts: 1) biological tissues are relatively transparent to NIR light; 2) light is absorbed or scattered by tissue components; 3) NIR light does not cause tissue damage, and; 4) the relative attenuation of NIR light is attributable to hemoglobin concentration in the circulatory system. The easy use and adaptability of NIRS when compared to other methods, as well as its low cost and noninvasive approach, have contributed to the rise in NIRS popularity in recent decades [33]. These properties are suitable for a wide range of clinical applications [35], including cancer diagnose [36, 37], neurology [38–40] and intensive care medicine [41, 42], both in adults and newborns [43, 44]. Our laboratory was the first in Brazil to introduce these methods in the clinic in the late 2000s [45], and we have been actively developing approaches and instrumentation in diffuse optical spectroscopy techniques since 2010 [33, 46, 47].

The fundamental physics concepts and experimental elements of NIRS will be presented in this chapter. First, we will understand the causes of light absorption and scattering and their consequences to light propagation in biological tissues. Then, we will cover the principles of one experimental approach to continuous-wave NIRS (CW-NIRS) based on the modified Beer-Lambert law and the spatially resolved spectroscopy. We will continue with an introduction to tissue hemodynamics before discussing instrumentation details for NIRS. Finally, we will explore standard CW-NIRS analysis and the general pipeline for working with CW-NIRS.

2.1 Interaction of near-infrared light with biological tissue

First, we need to recognize potential light-matter interactions and the relevant optical properties of biological tissue to understand the basics of NIR light propagation. The use of low-power sources in NIRS limits all possible light-matter interactions mainly to absorption and elastic scattering since there is neither enough energy to produce ionization nor enough power to generate nonlinear effects. The absorption process attenuates the light without changing its direction of propagation. On the other hand, elastic scattering changes light's direction of propagation while keeping the light intensity constant. Figure 2.1 shows an illustration of both interactions. We will get into more details about absorption and scattering in the following sections.

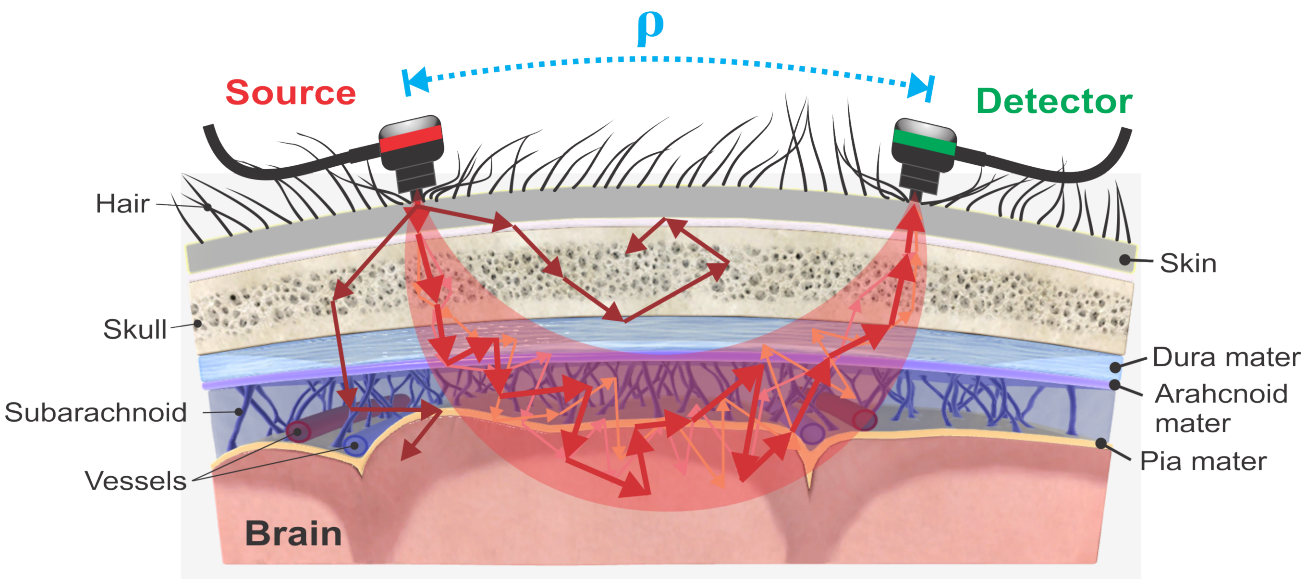

Figure 2.1: The **NIR light propagation in biological tissue** is governed by both absorption and (elastic) scattering. Representation of NIR light propagation in the brain. Photons are absorbed or scattered multiple times. Some paths lead back to the incident surface and collected by a sensor. The depth of the light into the tissue is determined by the distance between the source and the detector (rho) Figure drawn by A. Quiroga

2.1.1 Absorption

During absorption of light by tissue, the photons' energy is transferred to the medium. In a simplistic description, we can think of matter as a collection of particles (e.g., molecules or atoms) with discrete charges. The direct interaction of propagating light with the medium forces the particles to new excitation states with energy higher than the initial state. As the particles are not isolated, they will lose energy through collisions among themselves. Therefore, the photon's energy will be transferred to the material, increase the internal energy of the medium, and raise the system's temperature. Hence, the absorbed photon is not re-emitted, and the global effect of these small losses results in the attenuation of the incident light intensity. For absorption to occur, the incident photon energy should match the energy difference of two energy states of the particle (rotational, translational, or electronic states) and respect conservation of the other fundamental physical properties (e.g., angular momentum).

The scientists P. Bouguer, J. H. Lambert, and A. Beer described the relationship between the attenuation of light and the properties of an ideal medium formed by identical absorbing particles [48–50]. They found that the variation of light intensity (ΔI) of a specific wavelength (λ) decreases proportionally to the light intensity (I), the path length of light in a medium (Δx) [cm], and the absorption coefficient (μ_a) [cm^{-1}]:

$$\Delta I(t, \lambda, x) = -\mu_a(\lambda) I(t, \lambda) \Delta x. \tag{2.1.1}$$

When the path length is infinitesimal, $\Delta x \to 0$, the equation above reduces to the following differential equation:

$$\frac{dI(x)}{dx} = -\mu_a I(x), \tag{2.1.2}$$

whose solution defines the famous Beer-Lambert law:

$$I(x) = I_0 e^{-\mu_a x}, \tag{2.1.3}$$

where I_0 is the intensity of the incident light at $x = 0$. Although this result comes from an empirical deduction, the Beer-Lambert law can also be seen as a consequence of transport theory from a semi-infinite medium formed by pure absorbers and continuous-wave radiation. The photon diffusion formalism arrives naturally to an analogous relation of the Beer-Lambert law based on the definition of light radiance and the formulation of the radiative transport equation [51].

The absorption coefficient, μ_a, is related to the density of absorbing particles present in the material (ρ_a) and its cross-section (σ_a); it is a function of the wavelength, time, and position inside the medium for non-homogeneous media. As the cross-section is independent of both the relative orientation of the incident light and the absorber, we can define μ_a as:

$$\mu_a = \rho_a \sigma_a. \tag{2.1.4}$$

Macroscopically, μ_a represents the average absorptions per unit length that light undergoes as it travels through the medium. Its reciprocal represents the average distance a photon travels before being absorbed, and is known as the absorption mean free path or absorption length (l_a) [cm] [52]:

$$l_a = 1/\mu_a. \tag{2.1.5}$$

Empirically, μ_a is associated with the molar extinction coefficient at a given wavelength ($\varepsilon(\lambda)$) $[cm^2/mol]$ and the absorber's concentration in the medium (C) $[mol/cm^3]$ by the following expression:

$$\mu_a(\lambda) = \varepsilon(\lambda)C. \tag{2.1.6}$$

For a medium formed by N distinct absorbers, where each absorber contributes linearly to the total absorption, the total absorption of the medium is denoted as:

$$\mu_a(\lambda) = \sum_{i=1}^{N} \varepsilon_i(\lambda)C_i. \tag{2.1.7}$$

Another relevant piece of information from Beer-Lambert law (equation 2.1.3) is the attenuation of light. Light attenuation refers to the reducing intensity of light as it travels through a medium due to absorption. This medium's optical property is known as absorbance in chemistry and biology. In physics, it is more common to define the optical density (OD), and this work will adopt this definition:

$$OD(t, \lambda) = -\ln \frac{I(t, \lambda)}{I_0(t, \lambda)}. \tag{2.1.8}$$

By relating (2.1.3), (2.1.7) and (2.1.8) we have:

$$OD(t, \lambda) = \sum_{i=1}^{N} \varepsilon_i(\lambda)C_i(t)x. \tag{2.1.9}$$

Therefore, with a simple comparison between light intensities it is possible to obtain information about the medium's optical properties and constituents.

The molecules that absorb visible or NIR light in biological tissues are called chromophores. Biological tissues have various intrinsic chromophores, each with its absorption spectrum (see figure 2.2) contributing to light's total attenuation in tissue. The dominant chromophore in biological tissues is water (H_2O). The fraction of water in the organs depends on the body region and the tissue components. Water absorbs strongly before $300\,nm$ and after $1000\,nm$, but it shows relatively low absorption into the visible and NIR region. Another important chromophore is hemoglobin, a molecule found inside red cells (erythrocytes) and whose primary function is to transport around 97% of oxygen [53]. They are responsible for releasing oxygen to different body tissues and returning waste gases, such as carbon dioxide, to the lungs for exhalation. Each hemoglobin molecule can

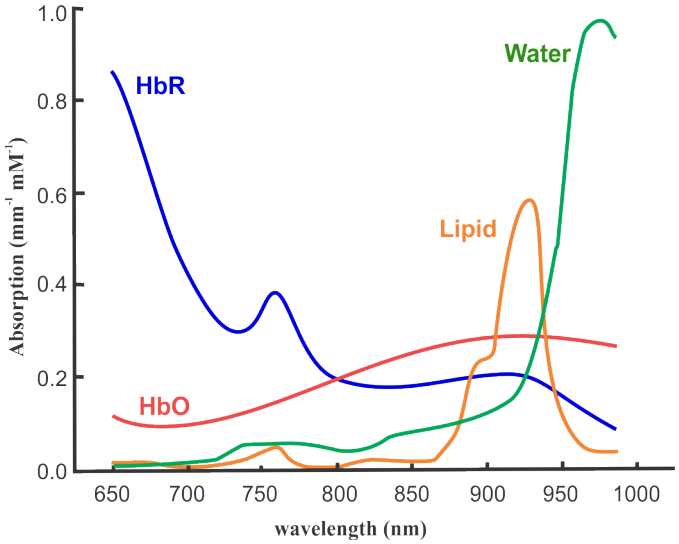

Figure 2.2: **Absorption spectra** of the main chromophores found in tissue in the near-infrared region of the electromagnetic spectrum. Data obtained from www.omlc.org

bind up to four oxygen molecules; when hemoglobin carries oxygen (a structurally relaxed state), it is in a state called oxyhemoglobin (HbO_2). After releasing oxygen, hemoglobin changes to a tense and reduced structure called deoxyhemoglobin (HbR). This structural difference changes the molecule's energy levels; consequently, the absorption spectrum for each hemoglobin state is different, especially at the NIR. The spectrum of HbR is highly absorbing in wavelengths shorter than 800 nm. Above this region, HbO_2 absorption is greater than HbR's. The wavelength where the two absorption spectra intersect occurs near 803 nm. The region between 600 to 1000 nm is typically referred to as an "optical window" [54]. In this region, absorption of other tissue molecules such as melanin and lipids is minimal compared to HbO_2 and HbR; therefore, NIR light can penetrate deeper into tissue [55].

Using equation (2.1.7), we can calculate the total absorption from the dominant chromophores concentrations in biological tissues (HbO_2, HbR, and H_2O):

$$\mu_a(\lambda) = \varepsilon_{HbO}(\lambda)[HbO_2] + \varepsilon_{HbR}(\lambda)[HbR] + \varepsilon_{H_2O}(\lambda)[H_2O]. \tag{2.1.10}$$

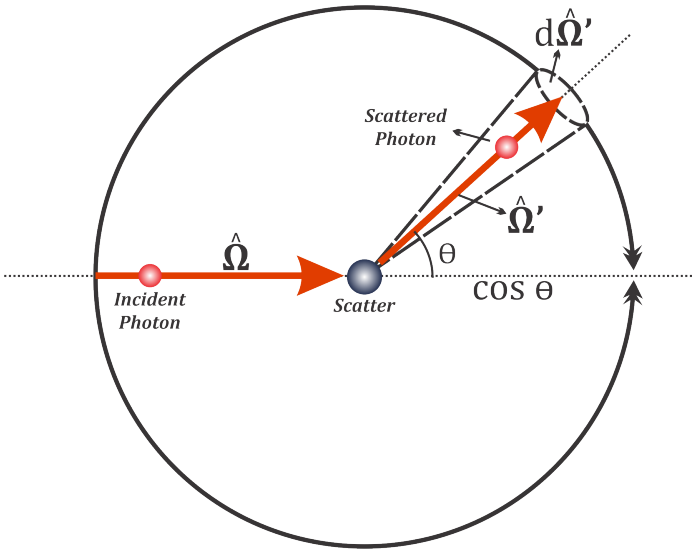

Figure 2.3: **Elastic scattering diagram**. The photon does not lose energy; instead, its trajectory alters due to contact with the scatter.

On the other hand, the concentration of total hemoglobin in biological tissue is very well approximated by:

$$[HbT] = [HbO_2] + [HbR]. \tag{2.1.11}$$

We can also estimate the blood oxygen saturation (StO_2) as:

$$StO_2 = \frac{[HbO_2]}{[HbT]} \times 100. \tag{2.1.12}$$

2.1.2 Scattering

Scattering is a re-emission process in which light changes direction during propagation in an inhomogeneous medium. The electromagnetic wave undergoes distortions that propagate the wave energy in new directions other than the incident direction. In the classical interpretation of elastic scattering, if the inhomogeneity is localized (scattering center) and composed of discrete charges (e.g., atoms or molecules), the interaction of matter with an electromagnetic wave forces the charges to oscillate at the frequency of the incident field. Consequently, the accelerated charges will radiate the electromagnetic energy in all directions with the same frequency.

There are two main models to explain the light scattering that depend on the geometric dimensions of the scatterer. The first model is the Rayleigh scattering, applicable if the light wavelength is significantly greater than the size of the scatterer. In this case, the scatterer cross-section is inversely proportional to the fourth power of the wavelength of the incident photon. Gustav Mie developed a more detailed model in 1908, describing the light scattering in a homogeneous and isotropic medium with spherical scatterers and dimensions comparable to the wavelength of the incident light [56]. In the two models, scattering depends on the light's polarization because the cross-section (σ_s) can be different for different orientations of the incident light. Then, we will assume that the scatterers are geometrically symmetric; consequently, the cross-section is independent of the direction of the incident light scattering ($\hat{\mathbf{\Omega}}$) (see figure 2.3), that is, $\sigma_s(\hat{\mathbf{\Omega}}) = \sigma_s$. The scattering cross section is the power (energy per second) scattered out of the plane wave divided by the incident intensity (energy per second per area) [52]. The differential cross-section is related to the angular distribution of the scattered radiation and depends exclusively on the orientation of the incident and scattered photons; hence, it is a function of the cosine of the relative angle (θ) between $\hat{\mathbf{\Omega}}$ and the scattering orientation ($\hat{\mathbf{\Omega}}'$) [52]:

$$\frac{d\sigma_s(\hat{\mathbf{\Omega}}, \hat{\mathbf{\Omega}}')}{d\hat{\mathbf{\Omega}}'} = \frac{d\sigma_s(\hat{\mathbf{\Omega}} \cdot \hat{\mathbf{\Omega}}')}{d\hat{\mathbf{\Omega}}'}. \tag{2.1.13}$$

Based on figure 2.3, and assuming the $\hat{\mathbf{\Omega}}'$ such as the axis of the cone of the solid angle $d\hat{\mathbf{\Omega}}'$, we can integrate over all angles to obtain the scattering cross-section:

$$\sigma_s = \int_{4\pi} d\sigma_s(\hat{\mathbf{\Omega}} \cdot \hat{\mathbf{\Omega}}') d\hat{\mathbf{\Omega}}'. \tag{2.1.14}$$

The above relation describes the probability of the incident light being scattered. Normalizing the differential cross-section to the cross-section for a single scatter, we obtain the scattering phase function:

$$f(\hat{\mathbf{\Omega}} \cdot \hat{\mathbf{\Omega}}') = \frac{1}{\sigma_s} \frac{d\sigma_s(\hat{\mathbf{\Omega}} \cdot \hat{\mathbf{\Omega}}')}{d\hat{\mathbf{\Omega}}'}. \tag{2.1.15}$$

Integrating over all solid angles, we obtain:

$$\int_{4\pi} f(\hat{\mathbf{\Omega}} \cdot \hat{\mathbf{\Omega}}') d\hat{\mathbf{\Omega}}' = 1. \tag{2.1.16}$$

The calculation of the phase function is relatively simple. For Mie scattering, the form of the phase function depends on the size and geometry of the particle (spheres). In this case, the phase function depends only on θ (see figure 2.3),

$$f(\hat{\mathbf{\Omega}} \cdot \hat{\mathbf{\Omega}}') = f(\cos\theta). \tag{2.1.17}$$

A good approximation to the phase function for Mie scattering is the Henyey-Greenstein phase function, initially proposed for the study of diffuse interstellar radiation [57, 58]:

$$f(\cos\theta) = \frac{1}{4\pi} \frac{1 - g^2}{(1 + g^2 - 2g\cos\theta)^{2/3}}, \tag{2.1.18}$$

where the parameter g is the anisotropy factor, and it is the average cosine from all possible scattering angles after a single scattering event:

$$g = \langle \cos\theta \rangle. \tag{2.1.19}$$

However, a simple scattering event is an ideal definition. In a realistic medium, the probability that a photon will undergo multiple single scattering events is high if the density of scatterers is also high. Consequently, the photon propagation becomes random throughout the medium. The treatment to describe multiple scattering is not trivial. An accepted solution is to use a statistical description. For this reason, we need to consider the density of the scatterers (ρ_s). Then, for a medium formed with identical scatterers, we can define the scattering coefficient (μ_s) $[cm^{-1}]$ as:

$$\mu_s = \rho_s \sigma_s. \tag{2.1.20}$$

Here, μ_s describes the probability of interaction between the photon and the scattering center after traveling a unitary distance; its reciprocal represents the average distance that the photon travels between two consecutive scattering events and it is known as the scattering length (l_s) $[cm]$ [52]:

$$l_s = 1/\mu_s. \tag{2.1.21}$$

In general, the scattering coefficient in the presence of N scatterers with density ρ_{s_i} and individual cross-section σ_{s_i} is the result of the contribution of each type of scatterer:

$$\mu_s = \sum_{i=1}^{N} \rho_{s_i} \sigma_{s_i}. \tag{2.1.22}$$

Media composed of different scattering centers are commonly anisotropic. Therefore, the cross-section depends on the orientation of the incident photon; this fact is a limitation for the Mie scattering model in biological tissues. Then, we must correct for the anisotropy of the problem and guarantee that the system will be isotropic, which is possible if we use the anisotropy factor, g, to obtain a new optical property called the reduced scattering coefficient, ($\mu_s^{'}$):

$$\mu_s^{'} = (1 - g)\mu_s \tag{2.1.23}$$

The $\mu_s^{'}$ description is equivalent to the probability of a photon being scattered after traveling a distance $l_s^{'}$ using many small steps l_s with slight deflection angles θ. As a result, the diffusion of photons is a random walk, and the path length is defined as $l_s^{'} = \mu_s^{'-1}$, where each scattering event is one isotropic scattering. For isotropic media ($g = 0$), $\mu_s^{'}$ is equal to μ_s.

Biological tissues have several particles, molecules, and structures, such as the cells and their organelles with different properties, sizes, and densities in each body region. Numerous factors contribute to the prevalence of tissue scattering, essentially by all heterogeneity present in the tissue. Optical scattering may be characterized as scattering by particles with a different refractive index than the surrounding media or scattering by a material with a variable refractive index. To approach the particle description, Mie theory, which discusses scattering from ideal spheres within a medium, might be applied [55]. The optical scattering characteristic of tissue may be replicated using a mix of spheres of varying diameters. In biological tissues, particle sizes range from 1 to 1000 nm, corresponding to the order of magnitude of NIR wavelengths (between 600 and 1000 nm). For example, the cell structures such as the nucleus, mitochondria, lysosomes, and the Golgi apparatus generate scattering [59]. Although red blood cells also help in dispersion, they only account for around 1.5% of tissue volume. Contacts between cells and extracellular space and cellular cytoplasm and organelles produce the majority of dispersion [60]. Hence, the Mie model may reflect scattering in biological tissue under certain conditions [55].

2.2 Continuous-wave near-infrared spectroscopy

We discussed the basic concepts of absorption and scattering separately. Nevertheless, these phenomena co-occur during light propagation in biological tissues [61]. Thus, we need to find a model that includes both absorption and scattering to understand how light behaves in biological tissue. At the NIR regime, μ_a is much lower than $\mu_s^{'}$ by approximately two orders of magnitude. The high scattering allows light to propagate a few centimeters deep into the tissue. As light is scattered multiple times randomly, some photons take trajectories in the direction of the incidence surface, which allows collecting the scattered light with an optical sensor on the surface. The attenuation of the detected scattered light is related to the optical properties of biological tissue. However, the exponential light attenuation depends on both absorption and scattering. In this case, a simple approach to model light propagation is to modify the Beer-Lambert law to account for scattering in equation (2.1.3) so that we can define the optical density as a function of these two parameters [62]. This approach is known as modified Beer-Lambert law (MBLL).

2.2.1 Modified Beer-Lambert law

Due to its theoretical and practical simplicity, the MBLL is arguably the most widely used approach to study light-tissue interaction in the near-infrared regime and its applications. This approach opens the possibility of monitoring temporal changes in blood oxygenation and blood volume using only continuous sources and optical detectors located at a certain distance from each other. However, a drawback is that it cannot determine absolute tissue hemoglobin concentrations. The MBLL relates the changes in light attenuation to the differences in tissue absorption in highly scattering samples [63, 64]. It uses the mean pathlength traveled by scattered photons as the best estimation to represent the distribution of photon pathlengths from the source to the detector, providing a constant of proportionality between the measured intensity and the tissue absorption [62].

In this approach, the optical density depends on μ_a and $\mu_s^{'}$. Moreover, it is readily expanded using the Taylor polynomials series around a reference time (typically, a baseline period denoted by t_0), so that [65, 66]:

$$OD(t, \mu_a, \mu_s^{'}) = OD(t_0, \mu_a, \mu_s^{'}) + \Delta\mu_a \frac{\partial OD(t_0, \mu_a, \mu_s^{'})}{\partial \mu_a} + \Delta\mu_s^{'} \frac{\partial OD(t_0, \mu_a, \mu_s^{'})}{\partial \mu_s^{'}} + \mathcal{O}(2), \quad (2.2.1)$$

where the optical density $OD(t, \mu_a, \mu_s^{'}) \equiv -\ln(I(t, \lambda)/I_0(t, \lambda))$ corresponds to the state of tissue at time t, and the reference optical density $OD(t_0, \mu_a, \mu_s^{'}) \equiv -\ln(I(t_0, \lambda)/I_0(t_0, \lambda))$ corresponds to the tissue baseline state. Further, $\Delta\mu_a$ and $\Delta\mu_s^{'}$ are the differential changes in absorption and scattering between the final and the baseline tissue states. Assuming that scattering remains constant ($\Delta\mu_s^{'} = 0$) after some time $t_0 + t$ and neglecting the higher-order terms ($\mathcal{O}(2) \approxeq 0$), we can rearrange expression (2.2.1) to obtain [67]:

$$\Delta OD(t) \approxeq \Delta\mu_a \underbrace{\frac{\partial OD(t_0, \mu_a, \mu_s^{'})}{\partial \mu_a}}_{\langle L \rangle}, \quad (2.2.2)$$

where $\Delta OD(t) = OD(t, \mu_a, \mu_s^{'}) - OD(t_0, \mu_a, \mu_s^{'})$ represents the change in optical density at time t with respect to an initial reference time t_0. In equation (2.2.2), $\langle L \rangle$ $[cm]$ is the mean pathlength of the scattered photons through the medium from a point source to a point detector with separation ρ on the surface (source-detector distance); it can be approximated as $\langle L \rangle \approx \rho \cdot DPF$, where DPF is the differential pathlength factor that accounts for the distance traveled by light in tissue due to $\mu_s^{'}$ [62, 64]. The DPF is a function of the wavelength and independent of the source-detector distance. For this reason, the use of $\langle L \rangle$ is more frequent than DPF in the literature [39, 68]. It is possible to empirically compute DPF for each wavelength with time-resolved techniques [69] or to estimate this value with Monte Carlo simulations [70].

Changes in OD can be related to changes in chromophore concentrations by associating equations (2.2.2) with (2.1.7) and (2.1.8):

$$\Delta OD(t, \lambda) = -\ln \frac{I(t, \lambda)}{I(t_0, \lambda)} = \sum_{i=1}^{N} \varepsilon_i(\lambda) \Delta C_i(t) \langle L \rangle. \quad (2.2.3)$$

Equation 2.2.3 is the basis of continuous-wave near-infrared spectroscopy (CW-NIRS) in biological tissue. The changes in light attenuation are proportional to the variations in tissue chro-

mophores' concentrations, mainly from oxy- and deoxyhemoglobin. Then, relating the equations (2.2.3) and (2.1.10), we have that:

$$\Delta OD(t,\lambda) = \left(\varepsilon_{HbO_2}(\lambda)\Delta[HbO_2] + \varepsilon_{HbR}(\lambda)\Delta[HbR]\right)\rho DPF. \tag{2.2.4}$$

The extinction coefficients and the DPF are found in the literature [71, 72]. Then, it is possible to infer the concentration changes in HbO_2 and HbR if we measure the attenuation changes at two or more wavelengths. The result is the following system of equations from Eq. (2.2.4):

$$\begin{pmatrix}\Delta[HbR]\\ \Delta[HbO_2]\end{pmatrix} = \rho^{-1}\begin{pmatrix}\varepsilon_{HbR}(\lambda_1) & \varepsilon_{HbO_2}(\lambda_1)\\ \varepsilon_{HbR}(\lambda_2) & \varepsilon_{HbO_2}(\lambda_2)\end{pmatrix}^{-1}\begin{pmatrix}\Delta OD(t,\lambda_1)/DPF(\lambda_1)\\ \Delta OD(t,\lambda_2)/DPF(\lambda_2)\end{pmatrix}. \tag{2.2.5}$$

The estimation of hemoglobin concentration changes from optical properties allows obtaining *in vivo* information about the physiological changes related to functional or metabolic processes in tissue.

2.2.2 Spatially resolved spectroscopy

This approach may determine absolute oxygen saturation despite not measuring absolute hemoglobin concentrations. The spatially resolved spectroscopy (SRS) method results from transport theory in a semi-infinite medium [72], showing that the light intensity also relies on the source-detector distance, ρ. According to photon diffusion theory, the light intensity at the CW approximation may be defined as [72, 73]:

$$I(\rho) \propto I_0 \frac{e^{-\rho\sqrt{3\mu_a\mu_s'}}}{\rho^2}. \tag{2.2.6}$$

Following equation (2.1.8), we may redefine the optical density as a function of the source-detector distance as:

$$OD(\rho,\lambda) = -\ln\frac{I(\rho,\lambda)}{I_0(\rho,\lambda)} \approx 2ln\rho + \rho\sqrt{3\mu_a\mu_s'}. \tag{2.2.7}$$

Equation (2.2.7) can be considered linear for $\rho > 1\ cm$ and we can determine its attenuation gradient. The partial derivation of OD in relation to ρ is given by:

$$\frac{\partial OD(\rho,\lambda)}{\partial\rho} = \frac{2}{\rho} + \sqrt{3\mu_a\mu_s'}, \tag{2.2.8}$$

And reorganizing equation (2.2.8) yields the relation:

$$\mu_a \mu_s^{'} = \frac{1}{3}\left(\frac{\partial OD(\rho,\lambda)}{\partial \rho} - \frac{2}{\rho}\right)^2. \tag{2.2.9}$$

Equation (2.2.9) clearly shows that the absorption coefficient and the reduced scattering coefficient are always coupled and cannot be unentangled in this approach. One possible workaround is to assume the scattering coefficient as known and use a linear approximation for the reduced scattering coefficient in the near-infrared regime, which can be expressed as [74]:

$$\mu_s^{'}(\lambda) = k(1 - h\lambda). \tag{2.2.10}$$

Here, h is the normalized slope of $\mu_s^{'}$ with respect to λ, which is dependent on tissue types and subjects, and k is regarded as a constant of proportionality.

If h is known, we can get an expression for the absorption coefficient, and then we can solve equations (2.2.9) and (2.2.10) to get:

$$k\mu_a = \frac{1}{3(1-h\lambda)}\left(\frac{\partial OD(\rho,\lambda)}{\partial \rho} - \frac{2}{\rho}\right)^2. \tag{2.2.11}$$

It is possible to extract all parameters on the right side of the equation (2.2.11). The measurement setup provides the source-detector distance and wavelength, while h can be found in the literature [75]. The attenuation gradient $\frac{\partial OD(\rho,\lambda)}{\partial \rho}$ can be calculated as an analogous attenuation slope using intensity values obtained at various distances from the same source, that is, $\Delta OD/\Delta\rho$. If $C \equiv \frac{1}{3(1-h\lambda)}\left(\frac{\partial OD(\rho,\lambda)}{\partial \rho} - \frac{2}{\rho}\right)^2$, then, it is possible to infer $k \cdot [HbO_2]$ and $k \cdot [HbR]$ if we measure the attenuation gradient at two or more sources-detector distances and wavelengths. The result is the following system of equations from (2.2.11):

$$\begin{pmatrix} k[HbR] \\ k[HbO_2] \end{pmatrix} = \begin{pmatrix} \varepsilon_{HbR}(\lambda_1) & \varepsilon_{HbO_2}(\lambda_1) \\ \varepsilon_{HbR}(\lambda_2) & \varepsilon_{HbO_2}(\lambda_2) \end{pmatrix}^{-1} \begin{pmatrix} C(\rho,\lambda_1) \\ C(\rho,\lambda_2) \end{pmatrix}. \tag{2.2.12}$$

Even though HbO_2 and HbR cannot be determined as absolute concentrations given that k is unknown, absolute blood oxygen saturation could be estimated since it does not depend on the proportionality constant:

$$StO_2 = \frac{k[HbO_2]}{k[HbO_2] + k[HbR]} = \frac{[HbO_2]}{[HbO_2] + [HbR]}. \tag{2.2.13}$$

It is worth noting that $\frac{\partial OD(\rho,\lambda)}{\partial \rho}$ only becomes essentially linear at larger distances. Furthermore, the detectors must be arranged closely to each other so that the various light streams investigate a comparable volume. As a result, we may employ optical characteristics to measure absolute oxygen saturation, which offers *in vivo* information about physiological processes in tissue.

2.3 Background on tissue hemodynamics

A broad understanding of tissue hemodynamics is essential to analyze the potential of NIRS. This section will focus on tissue hemodynamics and link it to the NIRS optical parameters, particularly, changes in absorption associated with oxyhemoglobin, deoxyhemoglobin, and oxygen saturation changes. It is worth noting that all tissue parameters obtained with NIRS represent averaged quantities over a large volume that depends on source-detector distance.

Biologically, a tissue is an organizational set of structural and functional similar cells that can organize and regulate an organism response to its environment [76]. Cells need a constant supply of energy (i.e., oxygen and glucose) to ensure the primary functions of the organs. The vascular system is a network specialized in delivering nutrients and removing metabolic waste from cells. Blood circulates throughout the whole body utilizing a circuit of vessels of different diameters (arteries, veins, arterioles, venules, and capillaries) to supply the cell demands. The arteries carry the oxygenated blood pumped from the heart and lung to the body. They are also responsible for regulating blood flow and blood pressure into the capillaries. The capillaries are the smallest and most numerous blood vessels, bringing red cells and plasma to within a hundred or so microns of every tissue cell in the body, so small that a single erythrocyte can barely fit through them. The exchange of oxygen, nutrients, and waste between blood and the surrounding tissue occurs mainly in the capillaries. The veins return the mixed oxy- and deoxygenated blood [77] to the heart and lungs so that red blood cells can oxygenate the deoxygenated blood to restart the cycle again.

The erythrocytes carry the hemoglobin molecules. As previously mentioned, the biochemical structure of hemoglobin consists of 4 globular proteins, two of the type α and two of the type β. Each globular protein contains a hemoglobin group, and each hemoglobin group has an iron

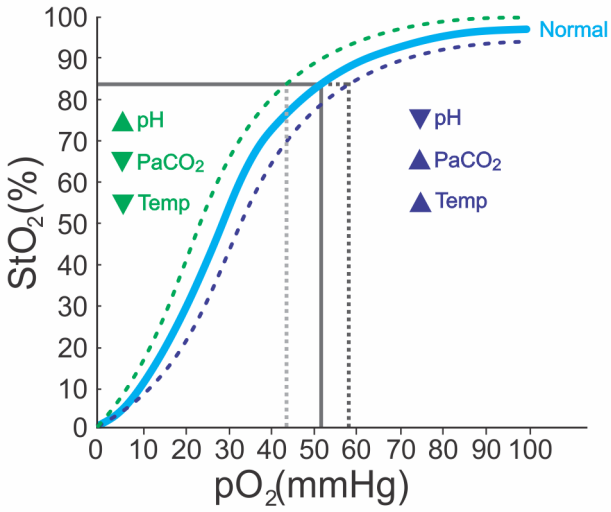

Figure 2.4: The **Hill curve** represents the relationship between oxygen saturation, StO_2, and the partial pressure of oxygen, pO_2. In humans adults, the curve can change or shift depending on various factors. The dotted purple line shows a decreased hemoglobin's affinity for oxygen to keep tissues well-oxygenated. The causes include increased body temperature, acidosis, and elevated partial pressure of arterial carbon dioxide ($PaCO_2$) levels. Similarly, the dotted green line shows an increase in hemoglobin's affinity for oxygen that can result from increased blood pH, decreased body temperature, or reduced $PaCO_2$ levels. Image obtained and adapted from [78]

diatomic molecule (Fe_2^+) that will bind to a diatomic oxygen molecule (O_2). When the Fe_2^+ is bounded to an O_2, the hemoglobin structurally changes to its relaxed state (HbO_2). When the hemoglobin molecule releases oxygen, it changes to a tense and reduced structure (HbR). Several factors govern the binding of oxygen with hemoglobin. When the oxygen concentration in tissue is low, a concentration gradient appears, and the HbO_2 releases the oxygen molecules so that the O_2 is dissolved into the tissue [79]. The tissue demand for oxygen determines the O_2 dissociation from hemoglobin. The Hill curve characterizes the oxygen equilibrium between StO_2 and partial pressure of oxygen (pO_2) (Figure 2.4). The partial pressure of oxygen characterizes different tissue states; an increment of oxygen dissolved in tissue represents elevated pO_2 levels. On the other hand, a decrease in pO_2 suggests an inadequate tissue oxygen level commonly indicating heart decompensation, chronic obstructive pulmonary disease, restrictive pulmonary disease, or hypoventilation. Then, the close relationship between pO_2 and StO_2 highlights the importance of NIRS as a non-

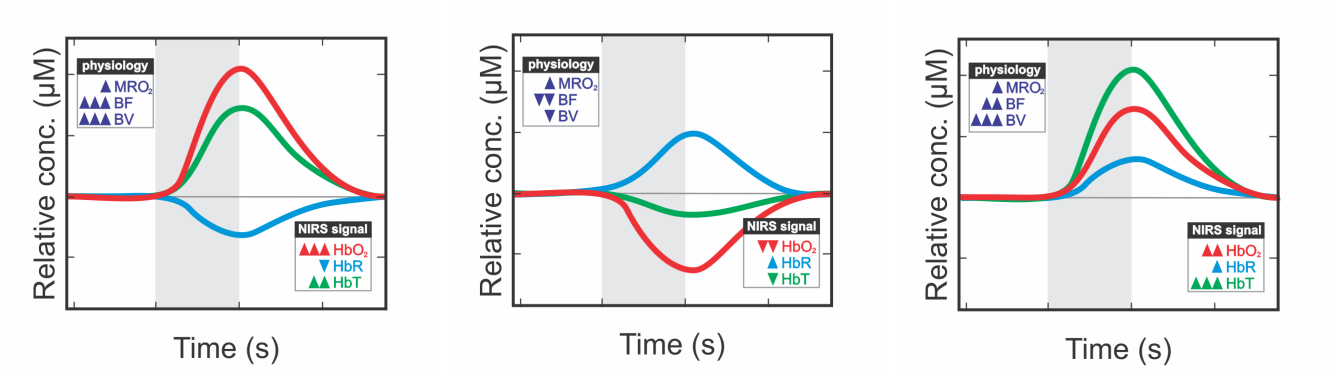

Figure 2.5: Typical **evoked hemodynamic changes** due to alterations in the metabolic rate of oxygen (MRO_2), blood flow (BF), and blood volume (BV). A shows a typical evoked hemodynamic response in the brain after sensory stimulation or a motor activity, B shows variations in the hemodynamic response when oxygen delivery is cut off, and C shows changes in the hemodynamic response when venous flow is blocked without cutting arterial blood supply. Figures obtained and adapted from [80].

invasive monitoring tool for tissue hemodynamics. Thus, measuring light intensity changes with near-infrared light and estimating oxyhemoglobin and deoxyhemoglobin concentration changes in tissue is key to studying microvascular hemodynamics.

Changes in the metabolic rate of oxygen (MRO_2), blood flow (BF), and blood volume (BV) affect hemoglobin concentrations measured with NIRS. In addition, changes in tissue hemodynamics can be induced by controlled stimulation or task activities. Figure 2.5A represents a typical evoked hemodynamic response in the brain after a sensorial stimulation or motor task. The stimulation increases neural activity, which requires local oxygen and causes a rise in the cerebral MRO_2 ($CMRO_2$); as a response to the increased metabolic demand, cerebral BF (CBF) increases, raising oxyhemoglobin concentration and reducing deoxyhemoglobin, i.e., more oxygenated blood than deoxygenated is present in the region, causing a washout effect [81]. Figure 2.5B shows changes in the hemodynamic response when oxygen supply is deprived (e.g., occlusions or breath-holding). This situation is commonly employed in studies aiming to quantify vascular reactivity. In this case, the stimulation increases the metabolic rate and, consequently, the oxygen consumption, decreas-

ing oxyhemoglobin concentration and increasing deoxyhemoglobin concentration in the sampled volume [82]. The situation represented by Figure 2.5C is found in specific conditions of blocking the venous flow without cutting the arterial blood supply (e.g., by occluding the arm and monitoring the anterior region of occlusion). As a result, the blood volume increment leads to increased oxyhemoglobin, deoxyhemoglobin, and total hemoglobin concentrations.

NIRS allows the study of the hemodynamics in biological tissues, such as muscle or brain, noninvasively and *in vivo*. The use of NIRS to study brain activity is typically known as functional NIRS (fNIRS). In most cases, brain activity increases oxygen consumption due to neurovascular coupling, CBF increases, and local oxyhemoglobin and deoxyhemoglobin are affected. The evoked hemodynamic response to a stimulation is a widely used mechanism to study the human brain in fNIRS. While absolute quantification is not readily available in most fNIRS using CW-NIRS, it is still possible to detect significant changes in brain activity compared to baseline periods, and analyze the spatial and dynamic response correlated with the stimulation for a subject or a group of subjects.

2.4 A brief overview of CW-NIRS instrumentation

A typical CW-NIRS system aims to control an emitter device that illuminates a small area of tissue with two or more NIR wavelengths, measures the diffuse reflectance re-emerged from the tissue a few centimeters of distance from the light source, and record the light intensity at the detector. The main components of a basic CW-NIRS system are the light sources, photodetectors, a tissue-coupling mechanism (i.e., optical probe), and a device to control and save data. Hence, NIRS systems have a simple setup, allowing the design of portable, wearable, and wireless equipment at a low cost. This section will briefly review the main characteristics of each NIRS component for fNIRS applications. We will restrict the discussion to CW-NIRS systems only.

2.4.1 Sources

Usually, two or more discrete wavelengths are needed to differentiate between oxyhemoglobin and deoxyhemoglobin, and it is desirable to use sources with a sharp peak in the spectrum (ideally monochromatic). The maximum output power possible is desirable to maximize the amount of light into tissue and improve the signal-to-noise ratio (SNR) at long source-detector distances (which have more sensitivity to deeper tissues). However, the power must not be high enough to generate any tissue damage or distort measurements ($\approx mW$). Generally, the light intensity fluctuations from the sources directly affect the detector's noise (drift effects). For these reasons, the power circuitry should reduce noise pickup, stabilize the power supply and cool the light source to help reduce emitted noise. Light-emitting diodes (LEDs) are an excellent option for NIRS applications, and they are available at different wavelengths within the NIR range (660, 670, 700, 850, 870, and 940 nm) with output power in the range of a few mW and spectral half-width of around 20 to 40 nm. Laser diodes are also an excellent option because they are small, consume low energy, and have output coherent light with output power in the mW range. Commercial systems usually use diode lasers of $GaAs/AlGaAs$ material (850 nm) or vertical-cavity surface-emitting lasers with wavelengths between 750 and 980 nm [83]. Even with various wavelengths available, a selection of specific wavelengths is needed to determine HbO_2 and HbR concentrations. Based on theoretical or experimental approaches, different wavelength combinations in the NIR range are used to minimize the crosstalk between the chromophores [84–89]. The ideal combination for increasing the accuracy of oxy-, deoxy-, and total-hemoglobin concentration measurement appears to be between 660 and 850 nm [89]. However, the 750 nm wavelength is typically more explored than 660 nm since the scattering is lower for the former.

2.4.2 Detectors

The main function of the detector is to receive and quantify the amount of light that emerges from tissue. The most used detectors for NIRS applications explore the photoelectric effect, i.e., the charged particles released by photons after they interact with the detector sensor to an electric

signal proportional to light intensity. Generally, photomultiplier tubes (PMT), silicon photodiodes ($SiPD$), and avalanche photodiodes (APD) are used. The PMT is based on the external photoelectric effect when a photon releases an electron from a photocathode surface, and a strong electric field accelerates the free electron. It knocks out other electrons from the surface of the dynodes, and the secondary electrons are accelerated, knocking out other electrons in a chain. As a result, this cascade effect leads to a successive multiplication of the carriers that have obtained significant gains in the order of 10^7 [83]. SiPD and APD are based on the internal photoelectric effect instead. The absorption of a photon in the semiconductor junction results in a jump of the electron to a higher energy state known as the conduction band, leaving behind a hole in the valence band. The electron movement as a result of added energy creates two charge carriers (an electron-hole pair). These carriers are responsible for a photocurrent, which is again detectable as an electric signal [83].

The detector selection depends mainly on the intended application and the source features. Recently, SiPDs have been more used in fNIRS applications due to their high sensitivity, gain, and speed acquisition [90, 91]. Moreover, they provide significant responsivity and higher SNR than APDs [92].

2.4.3 Optical probe

A source-detector pair (i.e., a channel) is the simplest NIRS arrangement. The depth of penetration in a small region of interest of tissue depends on the distance between a source and a detector (1 to 4 cm); however, the position of each source and detector on the tissue and their relative separations determine each channel's sensitivity [93]. Commonly, multiple channels are positioned on the skin to obtain a high image resolution, high sensitivity, accurate estimation of the chromophore concentrations, and cover a significant area [94]. The optical coupling is based on caps, elastic straps, masking tape, or glue [95].

The role of the optical probe is to primarily provide optode stability to reduce the motion artifacts in the NIRS signal. An excellent probe coupling is crucial for NIRS measurement because

less light will be lost, and more light is received in the sensor. Consequently, the SNR of the measurement will be higher. The probe arrangement depends on the region of interest (ROI), the number of available sources and detectors, the number of channels, and whether the source and detector are placed in the tissue directly or via fibers. Typically, a simple arrangement with 1–4 channels is used to study the microvascular muscle reactivity in the peripheral regions. The arrangement of the sources and detectors is more complicated to study brain function; defining the best arrangement depends on the brain regions of interest and the number of sources and detectors available. Some works use probes that utilize channels ranging from 30 (low-density coverage) to over 2,000 channels (high-density coverage) to cover the whole head [96]. Several head caps employ the EEG system of reference (10–20, 10–10, or 10—5) for positioning the optodes [94, 95, 97]. Earlier NIRS instrumentation utilized uniform source-detector distances for all channels [98], but the most recent systems include at least one short source-detector distance on the order of 5 mm to reduce the influence of undesirable components, such as extracerebral physiology.

2.4.4 Available fNIRS devices

Typical NIRS systems can be characterized by five essential components: sources, detectors, optical probe, electronic control module, and management software. The first commercial NIRS system was released in Japan in 2001. It was an instrument with 42 channels focused on brain studies. Currently, several companies are working to develop different portable or wireless multi-channel CW-NIRS systems to study human brain function (See table 2.1). Generally, CW-NIRS systems have sampling rates of up to 100 Hz. Several works have shown the ability of CW-NIRS systems to monitor adults and neonates at risk of brain hypoxia in clinical environments. For example, there is an estimate that approximately 10,000 brain oximeters have been utilized world-wide, mostly on adults [99]. Furthermore, CW-based systems offer the advantages of low cost and ease of transport.

Table 2.1: **Main commercially available CW-NIRS systems**. Data modified from [39, 83, 99].

System	No. of channels	Wireless	Company	Website
Dynot Compact	288 – 2049	No	NIRx, USA	www.nirx.net
ETG-7100	72 – 120	No	Hitachi, Japan	www.hitachimed.com
OXYMON MkIII	Up to 96	No	Artinis, The Netherlands	www.artinis.com
NIRO-200	10	No	Hamamatsu, Japan	www.hamamatsu.com
NIRS2 CE	16	No	TechEn, Inc., USA	www.nirsoptix.com
CW6	20 – 1024	No	TechEn, Inc., USA	www.nirsoptix.com
NIRScout	64 – 1536	No	NIRx, USA	www.nirx.net
HD-NI	Over 200	No	Cephalogics, USA	www.cephalogics.com
Brainsight NIRS	72	No	RogueResearch, Canada	www.rogue-research.com
LABNIRS	Up to 142	No	Shimadzu, Japan	www.shimadzu.com
fNIR100 W	4	Yes	BIOPAC Systems, USA	www.biopac.com
PocketNIRS Duo	2	Yes	DynaSense, Japan	www.dynasense.co.jp
NIRSport 88	Up to 256	Yes	NIRx, USA	www.nirx.net
Genie fNIRS	Up to 1024	Yes	MRRA Inc., USA	www.mrrainc.com
PortaLite	1	Yes	Artinis, The Netherlands	www.artinis.com
PortaMon	3	Yes	Artinis, The Netherlands	www.artinis.com
WOT	22	Yes	Hitachi, Japan	www.hitachimed.com
Brite	24	Yes	Artinis, The Netherlands	www.artinis.com
OctaMon	8	Yes	Artinis, The Netherlands	www.artinis.com
Hb13	8	Yes	ASTEM, Japan	www.astem-jp.com
LUMO	Over 12	Yes	Gowerlabs, UK	www.gowerlabs.co.uk
OEG - 17H	17	Yes	Spectra, Japan	www.spectratech.co.jp
NIRSIT	204	Yes	OBELAB, Japan	www.obelab.com

2.5 Functional NIRS experimental protocols

CW-NIRS measurements are relative, and therefore they must rely on paradigms, i.e., comparisons between the hemodynamics of two or more states. Typically, one state is neutral (reference), while controlled stimuli evoke other states. Due to the lower SNR, several blocks or trials composing reference and stimulation periods are performed to resolve the functional response and reduce the influence of noise in the NIRS signal. The study of average evoked hemodynamic changes helps to understand the dynamics and functionality of tissue. In addition, tissue impairment can also be studied using paradigms and comparisons between control and case samples. Another emerging CW-NIRS measurement is based on the resting-state paradigm, which does not include any stimulation. In this case, time courses of spontaneous hemodynamic changes from two distinct ROIs can be analyzed to derive a functional connectivity map defined by the temporal correlations between them.

It is critical to start with a clear definition of the research question to design an effective fNIRS protocol. *A priori* knowledge of tissue region, a definition of paradigm, an optical arrangement, and the delimitation of the subject population are also needed. Several researchers studied the sensitivity of CW-NIRS to different kinds of experimental protocols and conditions, and demonstrated the influence of stimulus duration in the NIRS signal, for example in motor [100–102], sensorial [103] and cognitive [104] protocols in the brain. In 2003, Franceschini et al. analyzed the bilateral responses evoked by different sensorimotor stimulations (finger tapping, sensorial tactile, and wrist electrical). They found higher amplitude in hemodynamic changes in motor stimulus than sensorial stimuli [98]. Overall, it is substantial to design the protocol robustly to minimize issues and reduce anticipatory effects that lead to false-positive responses. In the last years, the development of a new generation of wearable systems has opened up the possibility of performing CW-NIRS measurement with paradigms outside the laboratory environment, which allows the monitorization in naturalistic environments. New experimental protocols will probably emerge following these instrumentation advances in the future.

2.6 NIRS data analysis

In the NIRS signal, the tissue hemodynamic response is masked by components not associated with brain function. Therefore, we need to implement an effective procedure of several steps to remove unwanted parts of the measured optical signal. This section will introduce and review landmarks, conditions, and data processing steps to remove undesirable components and isolate the hemodynamic response.

2.6.1 Preprocessing

The NIRS signal contains information about systemic physiology, intrinsic measurement processes, and the evoked hemodynamic response (Figure 2.6). Significant systemic physiological contributions are due to superficial tissue layers because measurements are more sensitive to absorption changes in these layers. However, the global systemic hemodynamics and regulatory processes are induced by blood volume, flow, and oxygenation fluctuations in all layers of tissue at different time scales and frequencies [105]. The oxygenation, blood pressure, and vessels size fluctuate with each heart pulse with a heartbeat rate around 1.2 Hz (P-waves) in a person at rest. The oxygen also fluctuates with a breathing rate of around 0.2 Hz in adults (R-waves). Mayer waves are spontaneous arterial pressure oscillations tightly coupled with synchronous fluctuations of efferent sympathetic nervous activity with a frequency lower than respiration, around 0.1 Hz (M-waves) [106, 107], and they are also present in the signal. The origin of M-waves is yet unclear and discussed in the literature [108, 109]. There is no definition of a specific function of M-waves for being an epiphenomenon of normal baroreflex function [105]. However, M-waves could have the role of triggering the release of endothelium-derived nitric oxide through cyclic changes in vascular shear stress [110]. Although undesirable physiological fluctuations are a problem for estimating the evoked response, these oscillations can help study vascular physiology.

Intrinsic measurement effects are related to random noise, motion artifacts, and drifts, all derived from an imperfect measurement. We can define random noise as undesired random fluctuations in the detected light intensity at different frequencies. Random noise has two principal

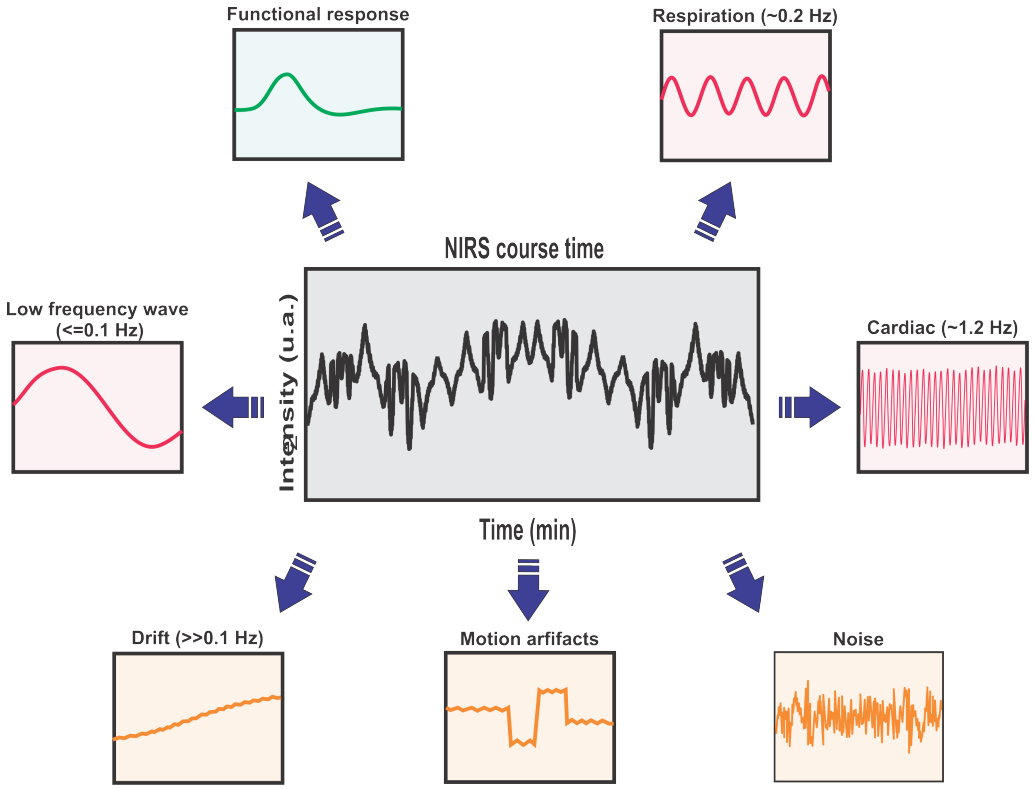

Figure 2.6: The mean **NIRS signal components** in NIRS data (black solid line) are consequences of systemic physiology processes (red solid lines), intrinsic measurement effects (yellow solid lines), and an evoked response (green solid line).

origins: the first is provided by the electric noise from the hardware system, and the second is the biological noise. Electrical noise is often assumed to have a uniform frequency spectrum (white noise), and biological noise has a 1/frequency behavior (pink noise). In addition, temperature changes in the optical system cause drift, thus, a very long oscillation that can climb up or climb down the NIRS signal.

The NIRS data is highly susceptible to motion artifacts caused by the relative motion between the optical probe and the tissue during data acquisition. Motion artifacts substantially impact the NIRS signal, making the extraction of the evoked response difficult or increasing the rate of false positives. We can identify two types of motion artifacts in the data (Figure 2.7). Type I corresponds to a spike, an abrupt change in the intensity without posterior harmonic oscillation and without altering the baseline continuity. Type II changes the baseline continuity of the intensity

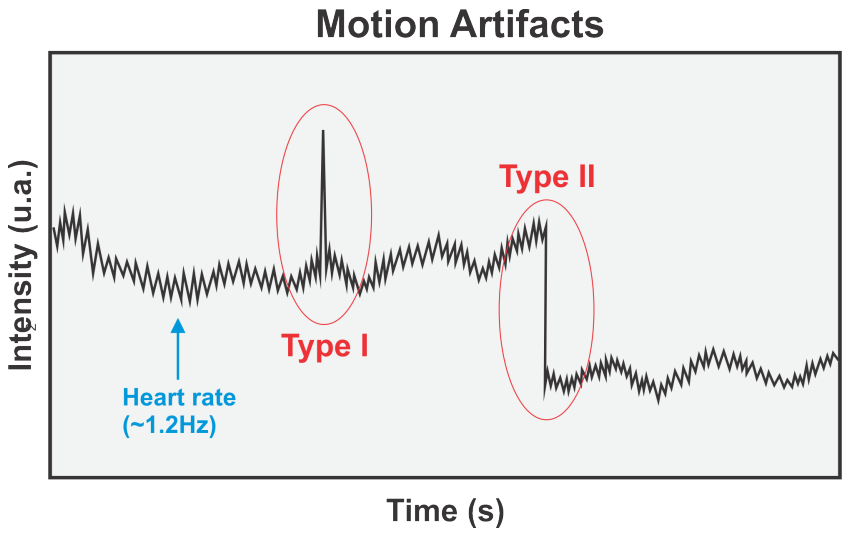

Figure 2.7: The **Motion Artifacts** of type I are also called spikes, abrupt change in the intensity without altering the baseline continuity. The motion artifact type II modifies the baseline continuity.

time course in a short time [111].

As we have noticed, many components make it challenging to extract the evoked response, so it is necessary to understand the existing processing strategies to deal with these undesired components.

Bandpass filtering

Some of the undesirable components are characterized by appearing at particular frequencies. One of the most common and more straightforward approaches is to remove specific frequency bands in the data employing filters. Frequency filtering is based on the Fast Fourier Transform procedure applied to discrete-time courses to reduce or enhance specific properties of the input signals [112]. The bandpass filter effectively removes specific frequencies from the signal, especially those from well-defined physiological origins. The high-frequency oscillations are removed using low-pass frequency filters, commonly cleaning frequencies higher than 0.5 Hz; therefore, P-waves and electronic noise can be easily removed. Low-frequency components are removed using a high-pass filter apart from signal waves or drift. Commonly, filtering is applied to the optical density

data before conversion to hemoglobin concentration changes, but it is also acceptable to use it on the oxyhemoglobin and deoxyhemoglobin signals [113]. The choice depends on whether the performance of posterior processing steps needs the filtered data or not. However, bandpass filtering cannot remove overlapping components with the hemodynamic response, such as respiration or M-waves. Therefore, this procedure should be carefully applied to avoid accidentally removing frequencies associated with the evoked response. As a result, bandpass filtering cannot be used without compromising the stimulus-response frequency bands to remove these specific effects [114]. In addition, frequency filtering cannot remove components associated with motion artifacts because it does not have a specific frequency.

Motion artifact corrections

The presence of motion artifacts in NIRS data is due to the relative movements of optodes and tissue, causing changes in the measured intensity and providing confounds and false hemodynamic changes. Novi et al. showed that no single algorithm could efficiently remove artifacts of type I and II [111]. On the contrary, it is necessary to use a hybrid procedure based on two classes of motion artifact corrections to reach a good result. The first class is based on spline interpolation to identify stretches or points of data corrupted by motion to replace predicted data and correct baseline changes. The spline algorithm calculates the standard deviation within a sliding window and replaces contaminated data points with the data residue from a cubic spline interpolation of the baseline trend on the data. This procedure is an excellent solution to correct type II artifacts. The second class is based on wavelet decomposition to correct motion artifacts of type I in the whole time series of NIRS data. The wavelet algorithm decomposes the time course of each channel in localized functions both in time and in frequency, and the wavelet coefficients with a higher probability of belonging to motion artifacts are manually zeroed. Then, the NIRS signal is reconstructed using inverse wavelet transform.

Removal of systemic contributions

The hemodynamic contributions in NIRS signals from the layers between the scalp and the cortex are typical of no interest to investigate brain function and can be considered a physiological source of noise. In brain studies, the optical probe is positioned on the scalp. Consequently, light must travel through different extracerebral and cerebral tissues (scalp, skull, cerebrospinal fluid, meninges, cortical grey matter) before leaving the head. The contributions of extracerebral layers (primarily systemic contributions) disrupt the results associated with functional brain activity. Therefore, brain functional studies must consider strategies of systemic contributions removal. There are several methods in the literature to solve this issue. The most common methods are principal components analysis (PCA) filtering and short-channel regression. PCA is a multivariate technique typically used to reduce the dimensionality of a dataset [115]. It separates N measurements into N components ordered by their contribution to the data variance assuming orthogonality and statistical independence [81]. The PCA filtering aims to identify the dominant component associated with the systemic contributions and remove it [116]. Commonly, the first component is attributed to the systemic contribution, since it has most of the variance across all measurements, which is characteristic of systemic sources of noise. Zhang discussed the fundaments of PCA filtering and explained the mathematical procedure in his work [117].

The short-channel (SC) regression uses channels formed by source-detector combinations with distances around 0.8 cm. Light detected at such short distances is assumed to contain only extracerebral information [118]. The goal of SC regression is to remove the extracerebral information from the long channels (source-detector distances around 3 cm) that contain extracerebral and cerebral information. Gagnon showed the theoretical fundamentals and details of SC regression, and several studies have reported significant improvements in the spatial localization of hemoglobin changes after using SC regression [119–126].

2.6.2 Functional NIRS processing

After the optical density is preprocessed, we want to find the evoked hemodynamic response from the optical signal. First, the OD should be converted to oxyhemoglobin and deoxyhemoglobin changes using equation 2.2.4. Given the low SNR for a single trial, repetition is needed to increase the statistical power to infer the evoked hemodynamic response based on oxyhemoglobin and deoxyhemoglobin concentration changes. There are statistical methods for adequately estimating the hemodynamic response and therefore infer brain function from the optical signal. The most used techniques in fNIRS are block averaging and the general linear model.

Block averaging

The block averaging approach calculates the average of the HbO_2 and HbR time series segmented by blocks (or epochs) consisting of an initial rest period and stimulation duration. This approach allows us to analyze the temporal dynamics of the response following activation without the need to define a hemodynamic response function. On the other hand, the temporal averaging of different time periods assumes that the response to the stimulus is always the same across the separate trials (which may not be true depending on the experimental protocol due to habituation effects). Another difficulty is comparing rest and stimuli values (therefore the inference of activation) for the averaged response with statistical methods. Most studies apply simple parametric statistical tests (such as t-student or ANOVA), although the data points are not independent of each other (as expected by these standard statistical tests). Regardless, block averaging is a great tool that complements the understanding of brain function. Furthermore, the high temporal resolution of NIRS allows for a detailed analysis of the hemodynamic response measured (rather than assumed as in other techniques) following stimulation.

General Linear Model

The general linear model (GLM) is a supervised analysis technique to find hemodynamic changes by modeling the measured signal with standard response functions. It was initially pro-

posed by Friston for fMRI [127], and since then, the GLM has been successfully adapted to NIRS. The GLM assumes that the measured hemodynamic time course for each channel results from the linear combination of hemodynamic changes [128]. Generally, the assumption of linearity is valid to the time interval between stimulus events higher than 4 seconds [129]. The GLM combines the experimental design (i.e., the time frames where activation started and finished) with a canonical hemodynamic response function (i.e., an analytical function that models the hemodynamic response to the stimulus) to provide a statistical model at the subject level with the best linear unbiased estimate of the hemodynamic response in the presence of noise [130]. Mathematically, the GLM uses a linear combination of regressors plus an error term to reduce the number of degrees-of-freedom and examine the evoked signal changes:

$$Y = X\beta + \epsilon, \tag{2.6.1}$$

where Y corresponds to the measured times-series and X is the matrix design that encodes the stimulus events and a canonical hemodynamic response. β is a vector containing the (estimated) coefficients from the GLM. The coefficient for each regressor in the matrix design corresponds to the strength of that regressor in the model of the measured data. The final term, ϵ, is the measurement error, often assumed to be an independent zero-mean Gaussian and randomly distributed variable. With this simplification, the problem of determining the hemodynamic response is reduced to estimate the β coefficients [128]. The X matrix is created by the convolution of boxcar functions, which reflect the experimental design, with the canonical hemodynamic response function (HRF_c)) [131]. One common HRF employed in fNIRS studies is [132]:

$$HRF_c(t) = k\frac{b^{a'}t^{(a'-1)}}{\Gamma(a')}e^{-bt}, \tag{2.6.2}$$

where $k = 1\ s$ is a constant that ensures equation's adimentional and is $a' = a/k$, where a is the time (in seconds) to reach the peak of HRF_c , t is the time $[s]$, and b $[s^{-1}]$ is the dispersion time constant; its reciprocal represents the response width in seconds ($\tau_h = b^{-1}$), usually set as 1.1 s [128]. Assuming $a = 6\ s$, we have $\Gamma(6) = 120$ so that equation 2.6.2 can be written as:

$$HRF_c(t) = \frac{1}{120\tau_h}\left(\frac{t}{\tau_h}\right)^5 e^{-\frac{t}{\tau_h}}. \tag{2.6.3}$$

To guarantee that equation 2.6.3 is a good representation of an ideal $HRF_c(t)$, it is necessary to constrain it to $t \geq 0$. To do so, we can use a unit step function, or Heaviside function, $H(t)$, so that equation 2.6.3 is redefined as [128]:

$$HRF_c(t) = \frac{1}{120\tau_h}\left(\frac{t}{\tau_h}\right)^5 e^{-\frac{t}{\tau_h}} H(t), \tag{2.6.4}$$

with $H(t)$ defined by:

$$H(t) = \begin{cases} 1 & t \geq 0, \\ 0 & t < 0. \end{cases} \tag{2.6.5}$$

If $N(S_i)$ is a boxcar function with a constant amplitude for the duration of the stimuli events, S_i, of an experimental protocol, we can define the matrix design as the convolution of HRF_c and $N(S_i)$:

$$X = HRF_c \circledast N(S_i). \tag{2.6.6}$$

With the matrix design well defined *a priori*, equation 2.6.1 can be solved for β using an ordinary least squares method, whose solution will be:

$$\beta = (X^T X)^{-1} X^T Y, \tag{2.6.7}$$

$$cov_\beta = (X^T X)^{-1} \sigma^2, \tag{2.6.8}$$

$$\sigma^2 = (Y - X\beta)^T (Y - X\beta) = \left\langle \epsilon^2 \right\rangle. \tag{2.6.9}$$

We can use a t-test to test whether the beta coefficients are statistically different from zero or whether multiple beta coefficients differ (e.g., the difference is nonzero). The expression for computing t is given by [133]:

$$t = \frac{c \cdot \beta}{\sqrt{c^T \cdot cov_\beta \cdot c}}, \tag{2.6.10}$$

where c is the contrast vector denoting the specific test to be performed.

However, when the slow dynamics of the hemodynamic response is sampled with a high temporal resolution, the noise in the NIRS signal will be correlated. It will result in serial correlations for

the error term , generating a potential bias in the estimation of the coefficients since the noise term is not zero mean [133]. Therefore, the time courses must be uncorrelated in the GLM analysis, which can be easily performed by including a prewhitening step. This process is a regression model in which the measured data and the GLM model are reweighted to remove colored noise from the residual . Therefore, applying the prewhitening in the equation 2.6.1 results in:

$$WY = WX\beta + W\epsilon, \tag{2.6.11}$$

where W represents the whitening matrix that is chosen based on the constraint that the residual of the model $W\epsilon$ must be white so that it no longer violates the assumptions of uncorrelated noise. In this work we assumed these considerations. Be $X_W = WX$, the solution using an ordinary least squares processing with the prewhitening filter is:

$$\beta = (X_W^T X_W)^{-1} X_W^T Y, \tag{2.6.12}$$

$$cov_\beta = (X_W^T X_W)^{-1} \sigma^2, \tag{2.6.13}$$

$$\sigma^2 = (Y - X_W\beta)^T (Y - X_W\beta) = \left\langle \epsilon^2 \right\rangle. \tag{2.6.14}$$

The GLM estimates of the β channels that satisfy the condition $Y - X\beta < \epsilon$ are defined as activated since their time series can be adequately modeled by equation 2.6.11. With the null hypothesis being $\beta = 0$, the channels are considered responsive to stimulation when $\beta > 0$ and are statistically significant ($p < 0.05$).

2.6.3 Summary of the fNIRS pipeline used in this work

Since we still lack a gold standard for NIRS data analysis, we used the following pipeline, which was constructed based on our group experience over the last two decades.

1. Raw data is the light intensity measured by a channel. Using the equation (2.1.8), we begin by transforming the raw data to the optical density.

2. The data quality must be evaluated at this stage and channels with low SNR are discarded.

3. The technique proceeds by correcting type I and type II artifacts using the hybrid artifact correction algorithm on the remaining data.

4. Using the modified Beer-Lambert equation, the preprocessed optical density is converted to oxy- and deoxyhemoglobin concentration changes.

5. The concentration of the time course is filtered; the characteristics of the experiment and research aims define the bandpass cutoff values of the filter.

6. The functional response may be obtained by the block averaging approach to analyze the types of hemodynamic curves that is measured. Later, the general linear model was applied to the data to determine channel response more accurately.

7. Last, the channels with a significant response to the stimulus are back-projected in a Monte Carlo sensitivity map model to allow spatial visualization.

It is important to mention that each step is required for each channel at the subject level. Group-level analysis may be performed by averaging the β's found for each subject when necessary. In this case, it is also advisable to consider the estimated covariance of each β found by the GLM.

2.7 NIRS limitations

Despite several recent advances in NIRS over the past two decades, the technique has certain limitations that should be considered and documented. From the data collection perspective, the presence of skin pigmentation may reduce light intensity and the SNR. Another disadvantage is that NIRS has a poor spatial (planar) resolution since it depends on the source-detector separation, which must be long (at least 3 cm) to get enough depth sensitivity. New instruments with high-density probes and overlapping measurements can significantly improve NIRS spatial resolution to the order of μm, although issues related to size, probe weight, and portability limits the wide use of such systems at the current time of this thesis.

From the data analysis perspective, it is worth noting that the modified Beer-Lambert law assumes the use of monochromatic light sources. This is difficult to achieve in practice because diode lasers and LEDs typically used in CW-NIRS systems have finite bandwidths. Since intensity and absorbance are wavelength-dependent, the absorption coefficient changes measured with CW-NIRS systems may yield smaller values than theoretically expected. Previous studies have shown that estimation of absorption coefficients becomes increasingly distant from their actual value as the spectral bandwidth increases [60]. Another minor topic is potential crosstalk with myoglobin in NIRS quantification since hemoglobin and myoglobin have comparable optical properties [35].

Last, it is essential to note that the magnitude of the NIRS signal is sensitive to changes in the source-detector distance and relative location on the tissue. In addition, paradigms that cause significant systemic vascular alterations and breathing patterns induce large systemic responses that affect the NIRS signal and should be monitored independently whenever possible.

Chapter 3

Functional NIRS measurements in patients with carotid artery stenosis (CAS)

One of the major advantages of NIRS is its sensitivity to hemodynamic changes at the microvasculature level, which can be used at the clinic to better understand how cerebrovascular diseases affect brain hemodynamics in a practical and straightforward way. For this reason, we collaborated with clinicians at the Clinical Hospital of the University of Campinas to explore the impact of fNIRS on the care of patients diagnosed with carotid artery stenosis. This chapter will go through the basic clinical aspects of the disease, the translation of fNIRS to the stenosis clinic and the main challenges we faced, and how we worked to overcome the logistical difficulties we found during this work. Section 3.1 offers an overview of the cerebrovascular circulation. Section 3.2 covers the main elements of carotid atherosclerosis disease, its consequences at the microvascular level, and the usefulness of NIRS in studying these effects. Section 3.3 addresses our study design and recruitment for over a year. Last, we discuss our novel database implementation to manage and store relevant clinical information in section 3.4.

3.1 An overview of the cerebrovascular circulation

The main arteries that supply the head and the brain are shown in Figure 3.1. The aorta artery emerges from the heart and goes to the other parts of our body. Three main arteries carry blood to the head and peripheral areas from the upper section of the aorta: the right brachiocephalic trunk artery (right BTA), the left common carotid artery (left CCA), and the left subclavian artery (left SA). From the right BTA arises two arteries, the right subclavian artery (right SA) and the right common carotid artery (right CCA). From the right SA branches the right vertebral artery (right VA). The left SA branches the left vertebral artery (left VA).

The right and left CCAs and the VAs carry all the blood supply to our head and brain. At the height of the carotid bulb, the CCAs bifurcate into an external and an internal carotid artery. The external carotid artery (ECA) primarily supplies blood to the superficial tissue of the face, while the internal carotid artery (ICA) supplies the anterior circulation of the brain (frontal, parietal, and most of the temporal lobes). The ICA is paired (i.e., one for each side, left and right), and each side is split into several branches. A important component is the anterior cerebral artery (ACA), which feeds the medial aspect of the cerebral hemisphere back to the parietal lobe. The anterior communicating artery (ACOA) connects the ACA from both hemispheres. The middle cerebral artery (MCA) is another branch of the ICA that distributes blood to the lateral aspect of the cerebral hemispheres (except the superior frontal and parietal lobes and the inferior temporal lobe). The posterior circulation of the brain (occipital lobe and the posterior-medium and inferior portions of the temporal lobe) is supplied by the posterior cerebral artery (PCA), which is located at the superior end of the basilar artery. One branch of the ICA is the posterior communicating artery (PCOA) that, as the name implies, connects the ICA with the PCA (therefore connecting the anterior and posterior circulations on one side of the brain).

The two ICAs and the vertebrobasilar arteries are connected by collateral circulation at the circle of Willis. One of the main features of the circle of Willis is that it provides redundancy within the circle that allows circulation even in the event of an artery being occluded.

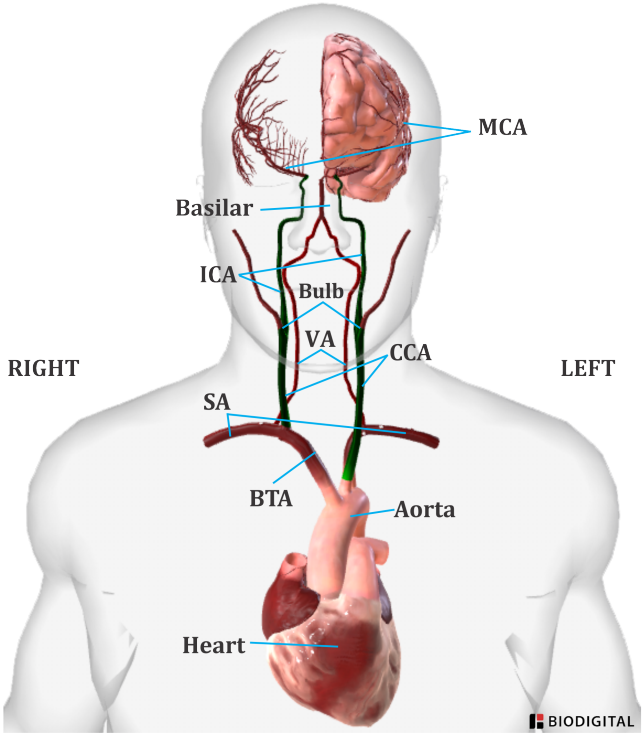

Figure 3.1: In the head, blood is supplied by the superior arteries that are branched from the aorta. BTA: brachiocephalic trunk artery, SA: subclavian artery, CCA: common carotid artery, VA: vertebral artery, ICA: internal carotid artery, MCA: middle cerebral artery. Image adapted from www.biodigital.com.

3.2 Carotid atherosclerosis disease

On average, someone dies in US from a stroke every four minutes (approximately 132 thousand individuals each year, which corresponds to 0.04% of US population) [134, 135]). One-third of survivors have some functional dependency or die three months later (44 thousand fatalities and another 44 thousand who are permanently incapacitated) [136]. In Brazil in 2016, there were approximately 107 thousand stroke deaths [137]. This fact has a significant effect on a country's economy. For example, the annual cost of stroke in the United States was approximately 49.8 billion dollars between 2016 and 2017 [136]. For people under 75 years old, men are more likely to have a stroke than women, but in general, women have more strokes than men. [138]. Carotid atherosclerosis disease (CAD) or carotid artery stenosis (CAS) causes at least 15-20% of all ischemic stroke [12, 139–141], and it is estimated that 5–10% of elderly (over 50 years of age) have

asymptomatic CAS with at least 50% arterial occlusion [142].

The carotid arteries are highly prone to developing atherosclerotic plaque at the origin of the internal carotid artery. Recent studies have shown that CAS causes hemodynamic impairments in multiple domains, which leads to clinically relevant neurodegeneration, even in asymptomatic CAS patients [13, 17, 143, 144]. CAS consists of the partial or total clogging of the blood vessels (stenosis) by plaque deposited within the artery carotid wall, causing vascular narrowing that alters the blood supply to the head and brain (see Figure 3.2). Plaque is formed by several pathogenetic processes, including the accumulation of extracellular lipid, the formation of macrophage foam cells, the accumulation of mineral deposits, chronic inflammation, the alteration of structural intercellular matrix or smooth muscle cells, instabilities of the lesion surface, the formation of hematoma and thrombus to fibromuscular junctions [145]. There is no obvious point at which plaque development begins, but the most likely scenario is that the entry of lipidic particles into the subintimal space activates monocytes, which adhere to the endothelium surface to remove them; eventually, they are caught by the lipids and die. Smooth cells are attracted to the region as well, causing a local inflammation [146]. The accumulation of monocytes and lipids creates macrophages that release free cholesterol into the extracellular region, attracting more monocytes and accumulating more macrophages into the area. This creates a vicious cycle, resulting in the formation of a necrotic core contained between the exterior and interior elastic membranes of the artery [147]. This condition is associated with risk factors such as smoking, high blood pressure, high levels of low-density lipoprotein, and genetic predisposition.

The carotid bulb is the site more prone to atherosclerotic stenosis. In addition, CAS progresses slowly for several years in asymptomatic patients. In some cases, plaque instability increases the risk of releasing small portions that evolve to an ischemic stroke or a transient ischemic attack (TIA). Ipsilateral embolic events frequently generate symptoms in patients diagnosed with CAS, differentiating between asymptomatic and symptomatic CAS. Then there must be a clear clinical differentiation between asymptomatic and symptomatic CAS essentially because hemodynamic instability and the chance of nonsurvival during surgery depend on both the severity of the symptomatic CAS patients and the plaque instability [147]. Currently, the direct consequences of CAS

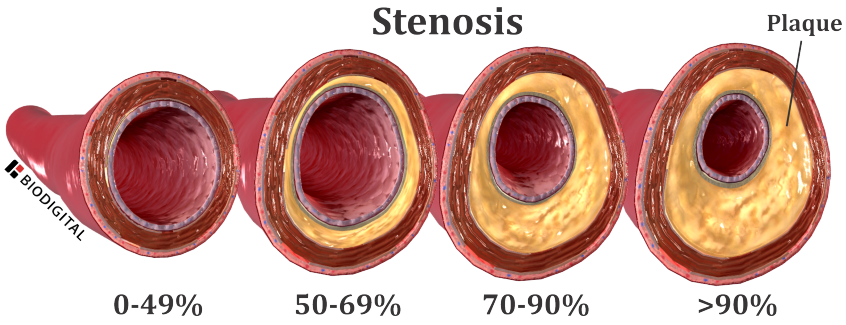

Figure 3.2: The carotid **stenosis** develops due to cholesterol creating a plaque within the arterial wall. The plaque gradually takes up more area within the artery, reducing its lumen (inner diameter). Imaged adapted from www.biodigital.com

on the brain of patients are poorly understood. Nevertheless, from a physiological standpoint, the brain damage associated with CAS directly results from microvascular cerebral hemodynamic dysfunction. Thus, CAS generates repercussions in cerebral hemodynamics that can cause damage to the white and gray matter in the long term [148]. Although there are compensatory mechanisms to overcome blood flow restriction, they appear to be ineffective in maintaining continuous brain perfusion and metabolism over the long term [149].

Many researchers have looked at the use of NIRS to study CAS patients in critical care settings [150–155]. For example, NIRS was used to assist in shunting or clamping strategies during carotid endarterectomy (CEA) and carotid artery stent (CAST) [153, 156–159]. The CEA and CAST are the most common surgical procedures to treat severe CAS patients, and these treatments are highly complex and have an unknown hemodynamic impact on the brain [149]. In investigating brain hemodynamic effects during the CEA intervention and aiding the decision for shunt placement, Pennekamp et al. monitored the brain of 151 CAS patients using EEG and NIRS [158]. The author concluded that NIRS might offer an effective monitoring tool to exclude a relevant number of patients for shunt during a carotid intervention. Pedrini et al. proposed using NIRS to assess perfusion and cerebral oxygenation and choose individuals with better hemodynamics for shunting [160]. The authors found that using NIRS to monitor cerebral oxygenation during CEA is a reliable strategy for detecting persistent hypoperfusion.

This work aimed to use NIRS to evaluate the deterioration of cerebral hemodynamics in individuals with carotid atherosclerosis before any surgical procedure. Our primary goal was to describe the cerebral hemodynamics of patients at the clinical stage and attempt to find correlates of the severity of carotid stenosis in the hemodynamic responses measured by NIRS. We also compared the hemodynamic responses of patients with carotid atherosclerosis to those of a control group matched for age, gender, and risk factors but not diagnosed with CAS. We hypothesized that: 1) CAS alters cerebral hemodynamics to a level proportional to its severity, and; 2) the induced changes in hemodynamics could be observed at the microvasculature with NIRS, both during a vasodilatory task and even during baseline.

3.3 Research Design

This work was developed through research cooperation between our group at the "Gleb Wataghin" Physics Institute (IFGW) and the Clinical Hospital (HC) at the University of Campinas (UNICAMP). The HC/UNICAMP established a unique outpatient clinic for CAS, known as the neurovascular clinic, recognizing that carotid artery stenosis affects both the brain and the vasculature. In this environment, neurologists and vascular surgeons jointly assessed patients diagnosed with CAS to speed up treatment.

At the neurovascular clinic, each case was studied and discussed based on the exams and clinical outcomes of plaque state, as determined by a blood chemistry test, transcranial Doppler (TCD) ultrasound and/or angiography, the cerebral state, as determined by MRI and/or EEG, and comorbidities such as Diabetes Mellitus, dyslipidemia, hypertension, heart diseases, brain disease, stroke history, obesity, and smoking. Patients in critical condition were referred to surgery for carotid revascularization (CEA or CAST). Based on this study's selection criteria, the clinical team selected a sample of patients who were evaluated with NIRS during their consult at the clinic.

3.3.1 Population studied

This research was evaluated and approved by the local Ethics Committee at the University of Campinas (CAAE 31592420.3.0000.5404), and all participants were instructed concerning the experiment protocol and signed an informed consent form prior to participation in this study.

We recruited a total of 50 patients with confirmed CAS diagnoses and 20 controls for this study. Table 3.1 shows the demographics and the clinical characteristics of all subjects within each group. In the patients, carotid ultrasonography was used to make the initial diagnosis, later verified by CTA of cervical arteries or digital arteriography. All recruited patients underwent a magnetic resonance angiography (MRA) exam, responded to a clinical questionnaire to assess medical history, and performed a neurological examination to identify comorbidities. Patients during pregnancy, with a previous history of dementia, or with the presence of atrial fibrillation were not included in our cohort. Similarly, patients with skull defects that could potentially affect the interpretation of the optical measurements were also excluded. Clinically healthy subjects without any CAS diagnoses were considered the control group, and they were formed mainly by relatives accompanying the patient. This procedure allowed for control of age, gender, and risk factors across the groups, although we cannot rule out the presence of asymptomatic CAS in the controls.

For our research goals, the degree of stenosis in each carotid artery was identified according to the severity of occlusion in four levels: 0 – 49%, 50 – 69%, 70 – 90%, and $> 90\%$ (assumed as occluded, i.e., when there was no detectable patent lumen at gray-scale ultrasound). The patients were sub-grouped as unilateral or bilateral stenosis depending on the number of carotid arteries affected by atherosclerotic plaque.

Table 3.1: **Demographic and clinical characteristics** of the study population. ICA: Internal carotid artery, CCA: Common carotid artery.

Parameter	Patients		Controls
	Unilateral	Bilateral	
Number of subjects	31	19	20
Mean age (years, SD)	67(8)	68(7)	63(8)
Female	7(22.5%)	5(26.3%)	6(30%)
Location of stenosis			
left ICA	9(29%)	18(94.7%)	-
right ICA	19(61.2%)	18(94.7%)	-
left CCA	2(6.5%)	1(5.3%)	-
right CCA	1(3.2%)	1(5.3%)	-
Degree of stenosis			
0% - 49%	1(3.2%)	0(0%)	-
50% - 69%	9(29%)	0(0%)	-
70% - 90%	20(64.5%)	13(68.4%)	-
Occluded	1(3.2%)	6(31.6%)	-
Asymptomatic	9(29%)	4(21%)	-
Symptomatic			
Transient ischemic attack	2(6.5%)	3(15.7%)	-
Ischemic stroke	20(64.5%)	12(63.1%)	-
Other conditions			
Hypertension	27(87.1%)	16(84.2%)	10(50%)
Diabetes	21(67.7%)	7(36.8%)	7(35%)
Smoking	18(58%)	10(52.6%)	5(25%)
Dyslipidemia	19(61.2%)	13(68.4%)	4(20%)
Heart failure	3(9.6%)	2(10%)	0(0%)
Coronary artery disease	2(6.5%)	4(21%)	0(0%)
Chronic kidney insufficiency	2 (6.5%)	3 (15%)	2 (10%)
Etilism	11(35.5%)	6(31.5%)	0(0%)
Obesity	0(0%)	1(5.2%)	0(0%)

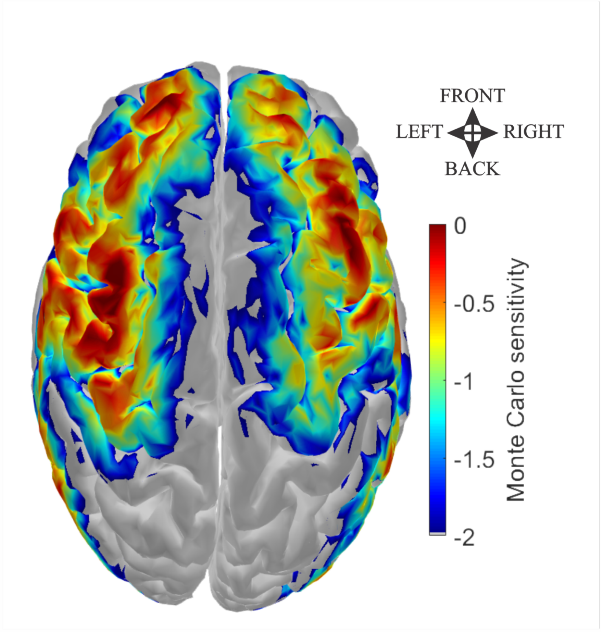

Figure 3.3: The **brain regions map** monitored with NIRS. We covered the significant brain areas irrigated by the carotid artery. The color bar represents a map of photons sensitivity based on Monte Carlo simulations. The red color represents regions with high photon sensitivity, while blue represents low-photon sensitivity.

3.3.2 NIRS Acquisition

The optical system used to acquire all NIRS data was a commercial CW-NIRS system (NIRScout, NIRx Medical Systems) available in our lab. The NIRS optical probe was designed with 14 sources at two different wavelengths (760 and 850 nm) and 30 detectors arranged in a head cap covering most of the head. The geometry configuration allowed 48 different source-detector pairs (i.e., channels) with 3 cm separation between sources and detectors. The temporal resolution of the system was 8.2 Hz.

Our work is a quantitative comparative study that aims to determine the association between carotid stenosis and cerebral microvasculature involvement. As a result, a NIRS device was used to monitor the brain region irrigated by the carotid arteries of the volunteers, and the probe sensitivity was tested by photon propagation in Monte Carlo simulation (see figure 3.3). We placed the optical probes in the frontal, parietal, temporal, and occipital areas to cover a large area.

3.3.3 Experimental Protocols

Each participant performed two independent experimental protocols (see Figure 3.4). The first protocol, a vasoreactivity test using breath-holding, has been employed regularly in the TCD and MRI [161]. Following a 60-second rest interval, individuals were required to complete up to seven attempts of voluntary breath-holding for a goal duration of 10 seconds each. A 30-second rest interval followed each trial. For a total of 6 minutes of data collection, NIRS data were obtained for the remaining 50 seconds following the last trial (Figure 3.4A). The goal of breath-holding is to study the local effects of CAS and to quantify the brain vasoreactivity that characterizes the hemodynamic response evaluated with NIRS. The cerebral vasoreactivity definition, analysis pipeline and the results obtained are detailed in Chapter 4.

The second experimental protocol consisted of a resting-state protocol. The individuals were required to sit down and rest for 6 minutes with their eyes closed and in silence (figure 3.4B). By analyzing the low-frequency hemodynamic oscillations, the resting-state tries to illustrate the effect of CAS on systemic hemodynamics. The analysis and the results are presented in Chapter 5. The average acquisition time spent by subjects was around an hour, with 40 minutes of NIRS setup and 20 minutes of brain monitoring.

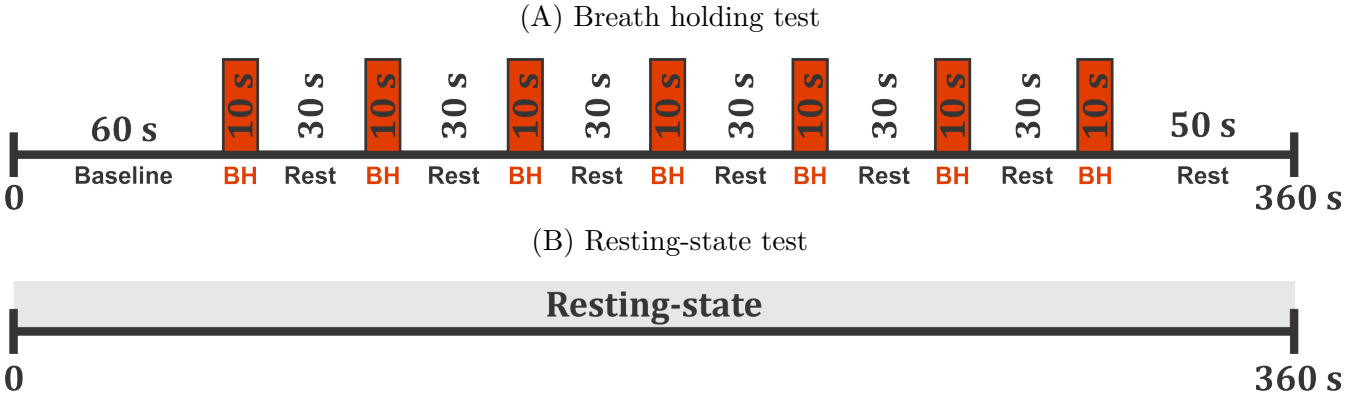

Figure 3.4: **Experimental protocols** performed by subjects during brain monitoring. (A) shows the breath-holding test, consisting of up to seven trials of 10 seconds of apnea followed by 30 seconds of rest for a total of 6 minutes of acquisition. (B) shows the resting-state protocol, consisting of 6 minutes of rest during brain monitoring with NIRS.

3.4 Database management

Creating research databases with clinical information has always been a frequent issue during our acquisitions. Since any clinical research question will involve correlations between acquired data with the patients' clinical data, it is essential to have them organized in a practical way. This research dealt with various data types, including volunteer information, clinical history, experimental data, NIRS system information, and management data.

At the same time, clinical information must be managed with safety since it contains sensitive information. Data management has become critical for clinical research in the era of big data, and Brazilian funding agencies (correctly) have required data management plans for the past few years. Standard spreadsheets are no longer viable solutions for correlating so much information.

For these reasons, we took the opportunity to develop an internal database management solution for this study. Our platform was designed to be more than a simple repository for this study; the goal was to provide a scalable platform for our clinical research. The initial solution was based on Visual Basic programming, but it was abandoned soon after due to the large data volume and the absence of remote access. The final solution was based on SQL programming to structure a database.

Briefly, a database management system (DBMS) allows users to remotely organize, store, and retrieve data from a computer. We established three stages for the design of our DBMS: (1) LOB data classification, (2) database architecture, and (3) access platform design. Each stage will be described in the following sections.

3.4.1 LOB data classification

Each acquisition included personal information about the subject, such as name, subject type (e.g., patient, control), date of birth, gender, weight, height, skin color, educational level, and contact information. Medical identification, medical history, type of disease, and comorbidities are all part of the clinical information for patients. On the other side, we have measurement

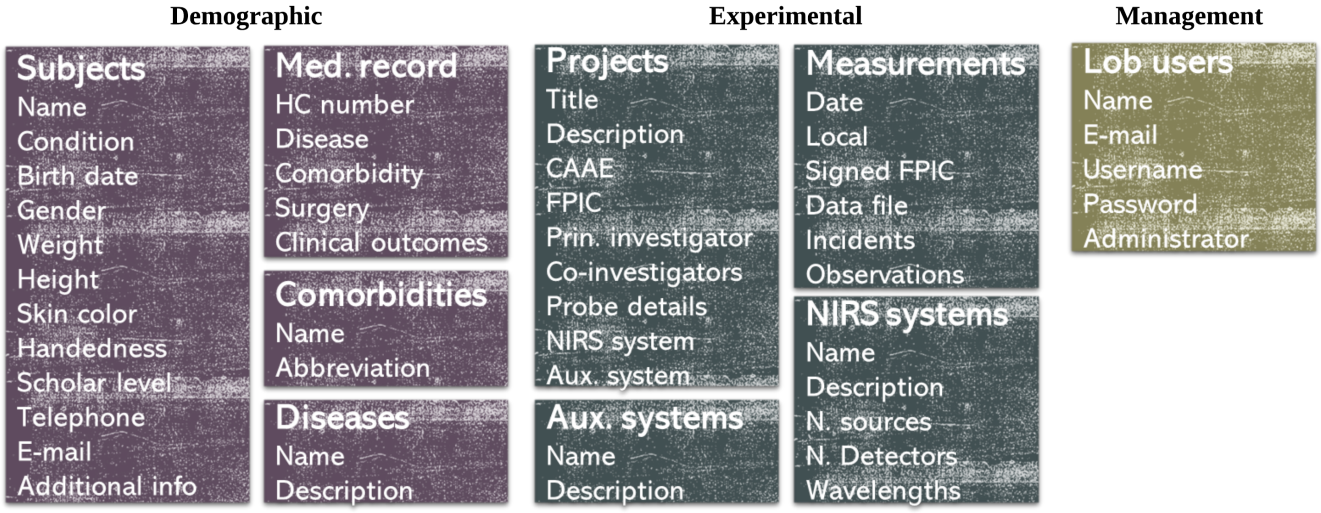

Figure 3.5: In the **Data classification**, we separated the data by the type.

data such as acquisition date, measurement place, signed consent form, optical data log files, acquisition report forms, and any other observations. In addition, to expand the use of this platform to other studies, it is also vital to store general information such as the title of the research project, the CAAE number, the investigators engaged in the project, and the specifications of the systems employed. As a result, data types were divided into demographic (personal and clinical), experimental (projects, systems, and measurements), and management data (users and permissions). Figure 3.5 summarizes all the fields and relational databases we envisioned for the management system we created. This classification makes the database structure easier (according to database theory) because each type and subset of data is considered a table, and each new data entry is considered a record.

3.4.2 LOB database architecture

The database structure for our data was created using the SQLite programming language. Following that, the LOB database's relational architecture was established. Each table should have its unique identifier, known as the primary key in the DB structure. The foreign key is

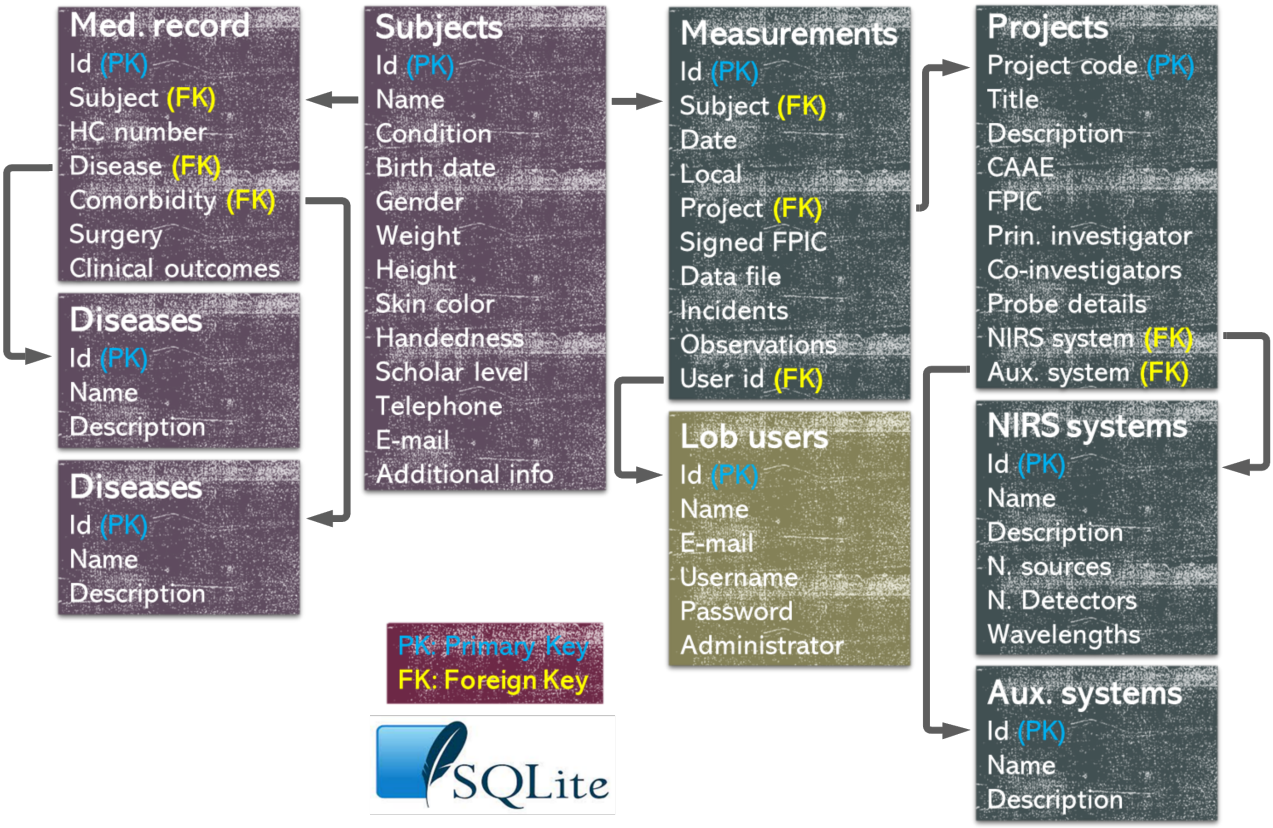

Figure 3.6: The **database architecture** was designed using the relational model.

a set of identifiers that manage the associations between records. The relationships among the different databases are shown in Figure 3.6. All group members are expected to have a login and password to access and upload information to the database. Some members will have administrator privileges, while others will have standard user access. The reasoning behind this structure is that users will only be able to perform limited activities to maintain the security and organization of the information. The relational model in the database benefits the records control; for example, for a user to add a new record, such as a new patient, *a priori* information about the disease and comorbidities must exist in the database. Alternatively, subject, project, and optical system records must already exist if the user adds a new acquisition record.

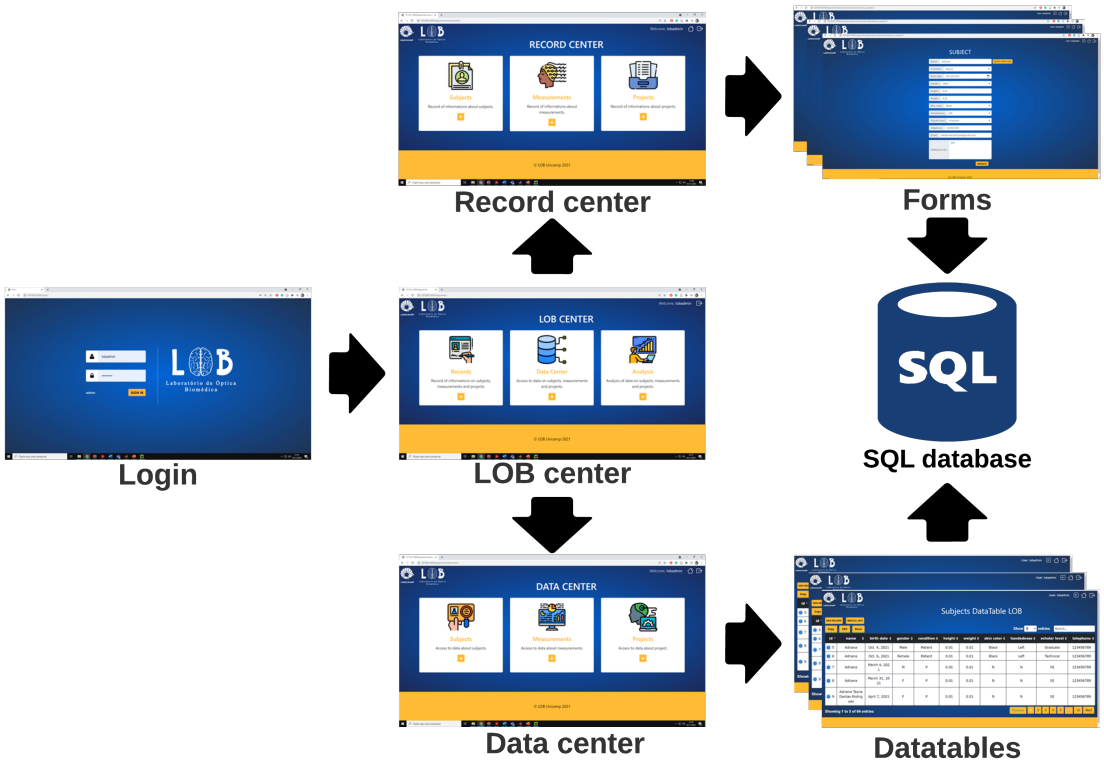

Figure 3.7: The **web architecture** developed to access the database.

3.4.3 Web platform design

Following the completion of the database structure, we focused on interactive access to the database. Django 4.0 was used to achieve this goal. Briefly, Django is a Python-based framework for rapid web development that employs the model-template-view (MTV) design. It is accessible under the BSD license. HTML5, CSS3, and Javascript was used in the web design. The web architecture is depicted in Figure 3.7. The login area corresponds to the initial website. The logged-in user will then be led to the LOB center screen, where they may choose to visit the record center to add new data or the data center to review previously saved data. The user can select one of the three forms to upload new data from subjects, measurements, or projects by entering the record center. All forms add new records to the database. The volunteer's personal and clinical information is collected on the subject form. The measurement form collects data on a

new acquisition, whereas the project form records information about the projects. To access stored data in the database, the user can select one of three alternatives in the data center section: subject, measurement, or projects. The identification number organizes the records, and the tables may be downloaded in various formats to work offline. Each web layout is highly dynamic, user-friendly, and contains helpful information about the operation of each widget.

This database structure was currently accessible for utilization, and all project information for this work has been transferred to it. Overall, we uploaded 50 CAS patient records with clinical and personal information and 20 healthy volunteer data. Simultaneously, 140 acquisitions are equivalent to 70 brain monitoring sessions with the NIRS system during breath-holding and 70 resting states. We expect that this platform will be employed in all of the lab's research programs in the future.

Chapter 4

Temporal effects of cerebrovascular reactivity in CAS patients

Carotid artery stenosis is linked to hemodynamic disorders in the brain. Even in patients with asymptomatic CAS, who have a low risk of clinical ischemic stroke, there is growing evidence that severe CAS causes meaningful neurodegeneration. Although the processes causing neurodegeneration are unknown, proximal stenosis and decreased artery blood flow cause arteriolar dilatation, which can affect cerebrovascular reactivity (CVR), cerebral autoregulation (CA), and cerebral blood flow (CBF). In this chapter we aimed to demonstrate how NIRS can be used to indirectly assess CVR in patients diagnosed with CAS. In particular, we introduce a new method to quantify the time delay of the vasodilatory response following breath-holding, as measured with NIRS. We believe that the quantification of the time delay can lead to a better understanding of the vasodilatory capability of the different regions of the brain.

4.1 Cerebrovascular reactivity

The development of CAS is complicated by hemodynamic compromise implicating a decrease in cerebrovascular reserve and cerebral blood flow (CBF), resulting in lower perfusion pressure

downstream of the carotid occlusion and persistent autoregulatory dilatation of cerebral arterioles. The cerebrovascular reactivity is an inherent defensive feature that helps to keep CBF stable [162–165]. The CVR measures our vascular system's ability to dilate blood vessels to meet tissue blood supply. Patients at risk of stroke or neurodegeneration may benefit from early identification of poor cerebrovascular autoregulation. The change in cerebral blood flow (CBF) or cerebral blood volume (CBV) caused by vasodilation can be used to evaluate the CVR. We hypothesized that CAS impairs the autoregulatory system, leading to cerebrovascular damage in the long term.

A cerebral vasoreactivity test can assess the ability of the brain's vasculature to increase CBF in response to a vasodilatory stimulus and the possibility for assessing cerebral hemodynamic impairment [166]. In CAS patients, the pathophysiologic mechanism of inducing arteriolar dilation to maintain cerebral perfusion in an environment of reduced large artery flow leads to a permanent condition of low CVR and increased oxygen extraction fraction (OEF) [167, 168]. A variety of possible hypercapnia stimuli can be used to induce vasodilation, including breath-holding [169], CO_2 rebreathing [170], inhalation of 5% CO_2 [171], or administration of carbonic anhydrase inhibitors such as acetazolamide [172]. Literature suggests that all methods are well correlated [173, 174]; among those, breath-holding tests are easy to perform, and there are no associated costs, but cannot control the amount of CO_2 retained.

Techniques that can directly or indirectly measure the cerebrovasculature status during a vasoreactivity test can help prognosis and treat patients with CAS. The cerebral blood flow velocity in the middle cerebral artery has traditionally been measured with transcranial Doppler ultrasound (TCD) to assess CVR. In fact, impairments following a vasodilatory stimulus in CAS patients have been previously described using SPECT, BOLD-MRI, ASL-MRI and TCD [13, 17, 173, 174]. However, information on blood flow in large arteries alone cannot distinguish reduced CBF caused by narrowing the carotid arteries from compensatory physiological reductions in CBF caused by reduced metabolic demands. In addition, since compensatory mechanisms can be local, the measurement of a large vessel will not be specific to regional hemodynamic variations across the brain.

NIRS is an alternative technique that can provide additional and complementary information about the hemodynamic status in the brain by measuring blood oxygen saturation noninvasively and in a portable manner. NIRS has been extensively validated and applied to CAS patients during a cerebrovascular reactivity test under different stimulations [40, 163, 172, 175–181]. Of particular interest, most previous studies use the breath-holding index (BHI, defined as the change between the measurement at the end of breath-holding and baseline, normalized by the duration of the breath-holding and the baseline measurement) to characterize the cerebral vasoreactivity. While this analysis is sensitive to the severity of the stenosis and correlates with TCD both in the affected and nonaffected sides [40, 182], it ignores the temporal dynamics of the induced vasodilation. Furthermore, when NIRS data are available in more than one location, they are typically collapsed into one single average across different areas of the head. Although cerebral vasoreactivity stimulation is supposed to be a global effect throughout the brain, it may not have the same impact on every cortical region. For example, Zirak et al. investigated the blood flow deficit produced by internal CAS, assessing cerebrovascular reactivity with NIRS and TCD to better understand the macro and microvasculature effects [179]. They observed that in the presence of CAS, microvascular hemodynamics did not correlate with macrovascular hemodynamics, suggesting that the measurements at the micro and macro levels accurately represent the disparities between global and local cerebral hemodynamic responses. On the other hand, Reinhard et al. used phase shifts between arterial blood pressure, respiratory-induced, and oxyhemoglobin determined by NIRS to study cerebral autoregulation in fifteen severe unilateral CAS patients [183]. Their findings revealed phase differences in all measures examined, suggesting that cortical dynamic autoregulation is impaired. These studies demonstrate that the NIRS approach is sensitive to cerebral vasoreactivity.

In this context, this work aimed to analyze the temporal dynamics and spatial variability of the NIRS-based cerebral blood volume response to voluntary breath-holding in CAS patients. We hypothesized that different brain regions fed by the internal carotid artery can respond differently to a vasodilatory stimulation and that the timing of this response can be associated with the severity of stenosis. In particular, we quantified the temporal delay between the start of the breath-holding and the beginning of the hemodynamic response and compared it among different

brain locations to understand how cerebrovascular reactivity varies throughout the regions fed by the internal carotid artery.

4.2 Data Analysis

For each subject, we first discarded channels with a signal-to-noise ratio (SNR) lower than eight from the raw intensity data since they do not contain relevant information. Light intensity from the remaining channels was converted to optical density and then corrected for motion artifacts with a hybrid algorithm. Next, we calculated HbO and HbR concentration changes using the modified Beer-Lambert law with a differential pathlength factor of 6 for both wavelengths. Data were band-pass filtered between 0.01 and 0.5 Hz to remove any long-term trends and high-frequency systemic physiology contributions prior to analysis. Total hemoglobin concentration (HbT) changes were calculated as the sum of HbO and HbR concentration changes. Since breath-holding is a global vasodilatory task supposed to increase blood volume without oxygen consumption, we restricted our analysis to HbT only.

For identifying the changes correlated with the breath-holding experiment, we performed a GLM on the HbT signal of each channel independently by convolving a canonical hemodynamic response function (HRF) with a boxcar with the breath-holding duration (10 s). The HRF was assumed as a gamma function without an undershoot period defined by equation 2.6.4. In this study, we purposely varied τ_h from 1.0 to 5.0 s to accommodate an altered dispersion in the cerebrovascular hemodynamics expected in patients with atherosclerosis. Therefore, we could investigate the time delay between the breath-holding onset and the start of the cerebrovascular vasodilatory response evoked by the challenge. By varying the response width time between 1.0 and 5.0 s, we could fit hemodynamic responses with onset delays ranging from 1 s to 7 s post breath-holding (Figure 4.1). (Note, the onset delay was calculated as the time when the HRF amplitude was larger than or equal to 0.01.)

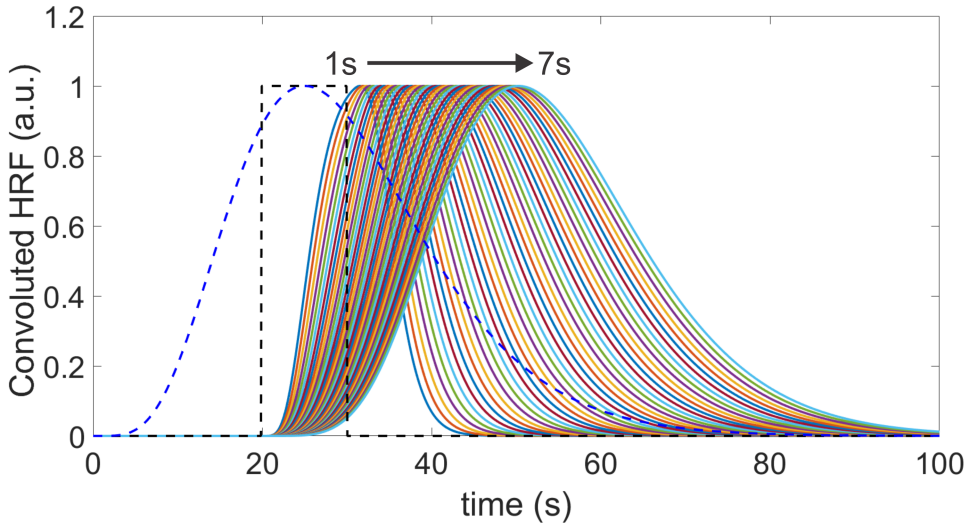

Figure 4.1: **Hemodynamic response function** (HRF) models used in the GLM analysis. By varying the dispersion time of the HRF basis function (Equation 2.6.4), we could model differences in the transit time of the cerebrovascular response to breath-holding in the patients diagnosed with carotid atherosclerosis. The HRFs with different delays (solid curves) were obtained by convolving the HRF basis function (dashed blue line) with a boxcar representing the breath-holding challenge (dashed black line). The resulting HRFs were characterized by their delay onset, which varied from 1 s to 7 s.

Channels that exhibited significant HbT increases (i.e., $\beta > 0$ in the GLM) compared to baseline ($p < 0.05$) for any HRF delay were considered as a response to breath-holding. When a single channel presented a vasodilatory response for more than one delay, we chose the delay that minimized the p-value related to the fit. For a hemispherical analysis of each subject, we calculated the median and the inter-quartile range (IQR) of all active channels in the hemisphere. Group averages across all subjects within the group were taken by averaging the GLM coefficients for each subject channel.

For the time-course analysis, the temporal response to breath-holding was performed by block-averaging all trials from a single channel from 5 s before the start of the challenge until 35 s after the breath-holding onset (or 25 s after the challenge was completed). Hemispherical time-courses were extracted by averaging the temporal courses of all channels with a significant response in the

hemisphere, while the subject response was obtained by averaging all channels with a significant response from both hemispheres. Finally, the time-course of the group was obtained by averaging the response across all subjects within the group.

Last, we extracted the parameters of interest for each subject (or each hemisphere) for comparison among the groups for statistical analysis. Given the heterogeneity of the disease and the small sample size to account for the high variability in each group, we performed nonparametric statistical tests to assess differences across groups. Specifically, we used a paired two-sided Wilcoxon rank sum test for the spatial analysis of activation to evaluate whether two groups have equal medians. A one-sided Wilcoxon rank sum test assessed whether HRF delays are longer in the stenosis groups than matched controls. For the temporal analysis, we extracted the peak (positive or negative) of each time-course and its corresponding time for each subject. Then, a one-sided Wilcoxon rank sum test was used to compare the parameters extracted from the time-series between two groups.

4.3 Results

4.3.1 Temporal dynamics of the hemodynamic response to breath-holding

Figure 4.2 shows the average time-series responses obtained for each group across all channels that exhibited a significative response to breath-holding. Although the hemodynamic response is quite heterogeneous within groups (reflected by large standard errors in each time point), it is possible to observe differences in the long-term trends for all contrasts (i.e., HbO, HbR, and HbT) that are potentially related to differences in the cerebrovascular reactivity among the groups. The differences in the temporal response to breath-holding support our approach of looking for vasodilatory responses at different time delays. The control and unilateral groups exhibit a hemodynamic response expected for breath-holding experiments and are typically reported in the literature with fNIRS [13–18]. Holding the breath increases the partial pressure of CO_2 ($pCO2$), which is a cerebral vasodilator. The vasodilation leads to increased cerebral blood volume across the vasculature,

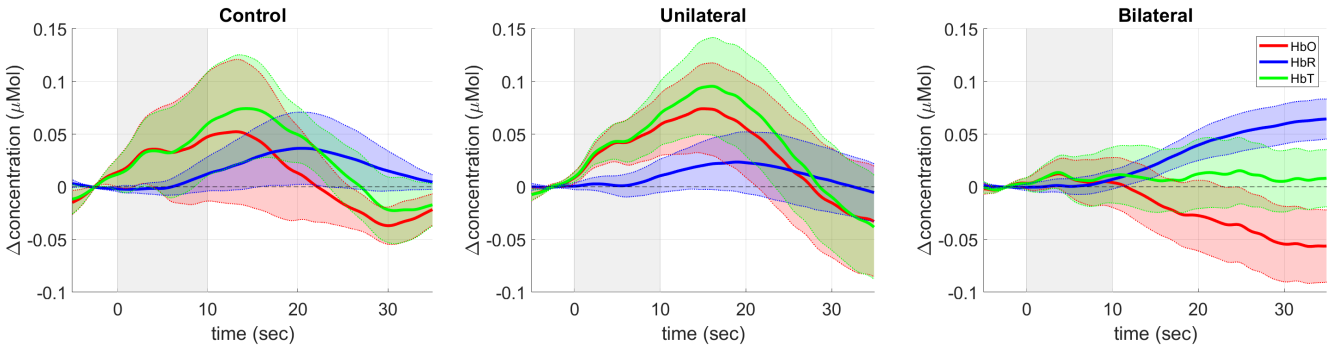

(A) (B) (C)

Figure 4.2: **Group averaged time-courses** of the oxy-hemoglobin (HbO, red), deoxyhemoglobin (HbR, blue), and total hemoglobin (HbT, green) concentration changes due to the breath-holding task (represented by the grey shadow in the plots) from all channels and all subjects. The solid curves represent the median values of the channels with a significant response across all subjects in each group, and the shadows around the curves represent the standard error of the mean.

reflected by the rise in HbT compared to the baseline. Since the dilation occurs primarily in the arterial side of the vasculature, the greater amount of blood volume is accompanied by an increase in blood oxygenation, leading to higher levels of HbO concentration than the baseline. The increase in HbR measured in fNIRS during breath-holding is harder to interpret since it results from the interplay between vasodilation in cortical and extra-cortical tissues and the metabolism required by the smooth muscle cells to dilate the extra-cortical vasculature.

The control group showed a slow but robust increase in HbR, reaching a peak at 20.5 s after the challenge onset (Figure 4.2A). The higher HbR compared to baseline is accompanied by similar increases in HbO and HbT that get to their maximum at 13.2 s and 14.3 s after the challenge onset, respectively. These two chromophores peak slightly longer in the unilateral group (Figure 4.2B), at 15.0 s and 16.0 s, respectively, although the difference is not statistically significant considering all subjects ($p = 0.36$ and $p = 0.59$ for HbO and HbT, respectively). At the same time, the increase of HbR in the unilateral group reaches its maximum at 18.9 s, which is faster than the control group ($p = 0.05$). Although not significant, these differences are consistent with the hypothesis that ICA stenosis restricts blood availability at the microvasculature. The faster HbR dynamics

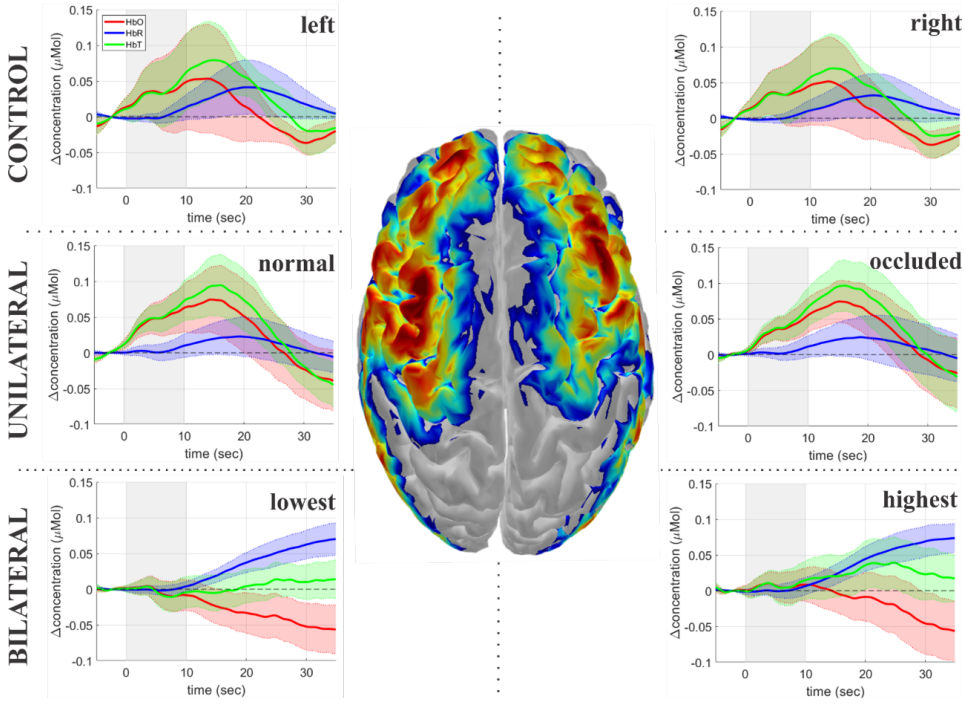

Figure 4.3: **Group averaged time-courses for each hemisphere** due to the breath-holding task (grey rectangle). The plots show the changes in oxy-hemoglobin (HbO, red), deoxyhemoglobin (HbR, blue), and total hemoglobin (HbT, green) induced by breath-holding for each group. The left column represents the left hemisphere (controls) or the hemisphere ipsilateral to either the nonoccluded ICA (unilateral patients) or the ICA with the lowest level of occlusion (bilateral patients). The right column shows the data from the right hemisphere (controls) or the hemisphere ipsilateral to either the occluded ICA (unilateral patients) or the ICA with the highest level of occlusion (bilateral patients). In all plots, the solid curves represent the median values of the channels with a significant response across all subjects in each group, and the shadows around the curves represent the standard error of the mean.

in the unilateral stenosis could be associated with the difficulty to balance metabolic demand and vasodilation.

On the other hand, the average time-course of the bilateral group shows a slight and continuous decrease in blood oxygenation (HbO) in parallel with an increase in HbR, resulting in a nonsignificant change in blood volume (Figure 4.2C). These dynamics were seen for most patients within the bilateral group, although few showed an HRF with a similar time-course from the unilateral and

control groups. The behavior exhibited in Figure 4.2C would be observed in the face of increased OEF when the oxygen available at the local microvasculature is used, but there is not enough supply of blood to match the demand required by the vasodilatory challenge. Unlike the previous two groups, both HbO and HbR are significantly different from the baseline at the end of the time window analyzed (25 s after the end of the challenge) in the bilateral group. By modeling the time series, we projected HbR to take 52 s to return to baseline (not shown in the Figure). Similarly, the decrease in HbO in the bilateral group would last approximately 80 s from the beginning of breath-holding. When compared to HbR, the longer time of HbO to return to baseline can be indicative of the limited vasodilatory capability expected in the bilateral patients.

When comparing the average temporal response measured in each hemisphere, we did not find any significant differences between the two hemispheres due to the vasoreactivity task in any of the two patient groups (Figure 4.3). The hemispherical similarity was already expected for the control group, and it works as a controlled condition in this case.

4.3.2 Characterization of the hemodynamic response delays

Figure 4.4 shows arbitrary responses to breath-holding at the individual level separated by subjects' group. It is clear from this overall sample that the responses are quite heterogeneous within each group. We observed a global response (i.e., a significant increase in HbT across all channels) with a small time delay (typically $1 - 3$ s) uniform across the brain regions for most controls. Few subjects in the control group showed a global and uniform but delayed response, while others had local delays in specific areas (mainly in the inferior frontal cortex).

The response in the unilateral group was also predominantly global, although nonuniform. The time delays of the vasodilatory response were quite variable across the brain for the majority of the unilateral patients, with most responses delaying $3 - 6$ s. This pattern was also observed in the bilateral patients. However, almost half of the patients in this group lacked any vasodilatory response in a significant portion of the brain, one pattern that was rarely observed in the unilateral group.

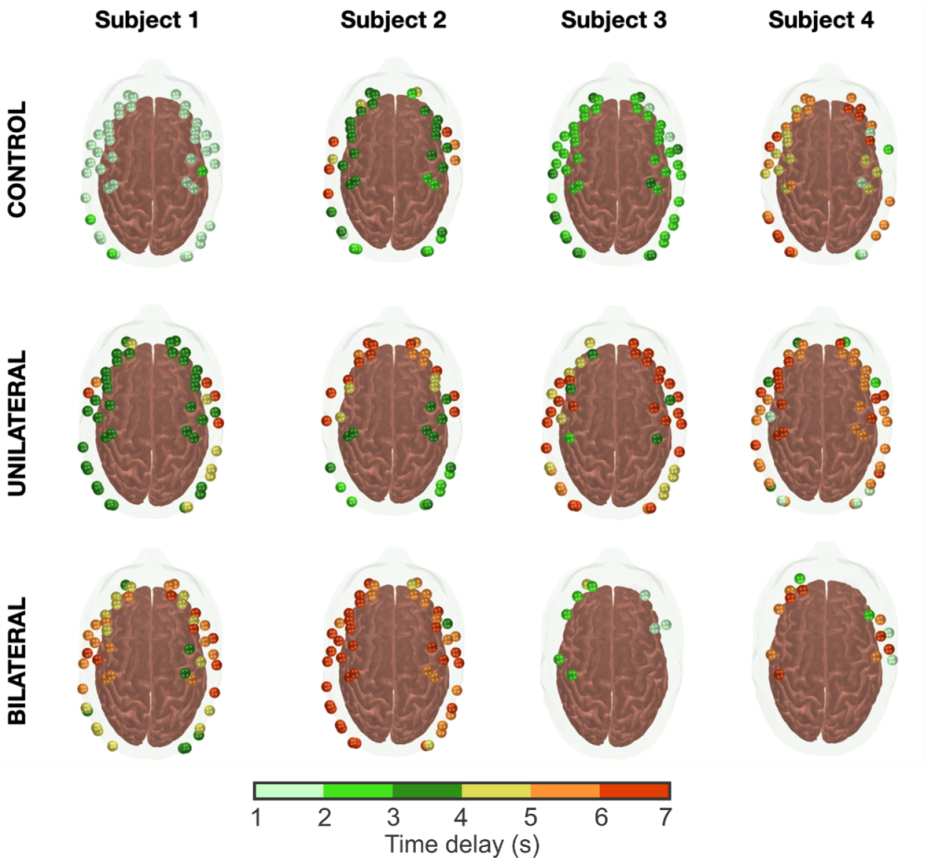

Figure 4.4: **Individual responses to the breath-holding** challenge from four arbitrary subjects within each group. Each sphere on the head represents a NIRS channel that showed a significant vasodilatory response (as measured by a significant increase in HbT) following apnea. The color bar represents the time delays of the modeled HRF that maximizes the fit of the measured time courses

The descriptive statistics of the time delays measured in the channels that responded to the vasoreactivity challenge are shown in Table 4.1. Across all subjects within a group, patients appear to take slightly longer to vasodilate than controls. The hemodynamic onset following breath holding took a median (IQR) of 3.8(1.9) s in the patient group, which is approximately 10% lower than the average delay found in controls (3.5(1.2) s, $p = 0.05$). When split between unilateral and bilateral stenosis, the hemodynamic latency was slightly longer for the latter: 3.8(1.5) s and 3.9(2.2) s for the unilateral and bilateral groups, respectively. The difference in the response delay was not significant for any of the groups compared to the control subjects ($p = 0.08$ and 0.06 for the unilateral and bilateral groups, respectively). However, the distribution of the time delays for each

Table 4.1: **Delay of the hemodynamic response** due to the breath-holding challenge. The group patterns suggest a slower vasodilatory response in the patients diagnosed with carotid stenosis. The higher standard deviation of the time delay distribution across all channels in the bilateral group is indicative of higher heterogeneity of activation patterns.

Group	Percentile			Inter-quartile range (IQR)
	25%	50% (median)	75%	
Average delay across all channels				
Control	2.89s	3.53s	4.04s	1.15s
Unilateral	2.97s	3.80s	4.50s	1.53s
Bilateral	2.98s	3.85s	5.14s	2.16s
Standard deviation of the time delay across all channels				
Control	0.62s	1.06s	1.37s	0.75s
Unilateral	0.70s	1.02s	1.49s	0.79s
Bilateral	0.77s	1.24s	1.52s	0.75s

group (Figure 4.5A) revealed a highly skewed profile for the control group towards longer delays, which overestimates the delay times in this group and therefore limits our statistical power to assess statistical differences in the data.

We also investigated the dispersion of the time delays across the different channels since it could provide information about the heterogeneity of the vascular response induced by vasoreactivity. Overall, patients showed a slightly higher standard deviation of time delays when compared to controls ($p = 0.11$). However, the response heterogeneity is different between unilateral and bilateral patients in this case. While we observed no significant differences in the dispersion of the delays in the unilateral group when compared to controls ($p = 0.24$), the bilateral group presented the highest standard deviation of time delays, with a median (IQR) of 1.24(0.75) s, which is marginally significant when compared to the control group ($p = 0.05$).

We attempted to quantify any potential hemispheric differences during vasodilation by computing the laterality index ($LI = (H_1 - H_2)/(H_1 + H_2)$, where H_1 and H_2 represent the two cerebral hemispheres). In our analysis, H2 was always considered as the hemisphere ipsilateral to the ICA with occlusion (unilateral group) or the ICA with the highest level of occlusion (bilateral

(A)

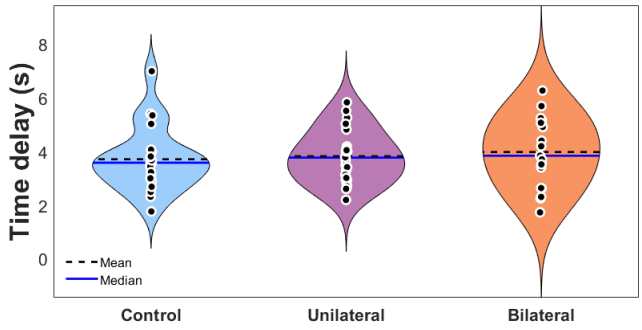

(B)

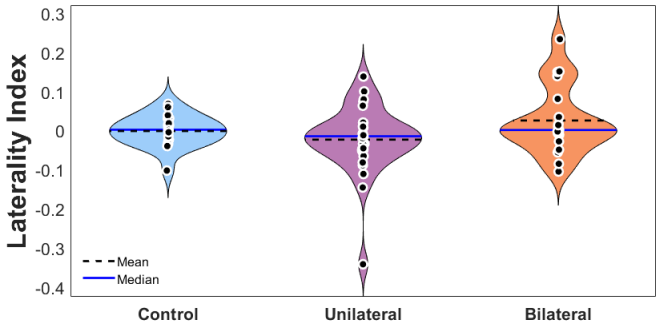

Figure 4.5: **Distribution of** the (A) **time delays** of the vasodilatory hemodynamic response to breath-holding and the (B) **laterality index** calculated to assess potential differences across the two hemispheres.

group); therefore, negative values of LI suggest longer delays in the hemisphere ipsilateral of ICA (unilateral group) or the highest level of ICA occlusion (bilateral group). However, we found no significant differences between the two hemispheres (Figure 4.5B). Even when we found a delayed vasodilatory response to breath-holding in a given brain region, the homotopic area showed a similar delay. As a result, the laterality index was symmetrically distributed around 0 in all groups, with few outliers present in the patient groups.

4.3.3 Quantification of the vasodilatory capability

The cerebrovascular capacity to vasodilate following breath-holding was assessed by counting the fraction of channels with a significant response in the NIRS probe, independently of the time delay. Figure 4.6A shows the distribution of the active channels per subject for each group. It is possible to note a bimodal distribution in all groups, but the more severe the condition is, the greater the difference between the two distributions within the group. This difference is reflected in the lower fraction of active channels during breath-holding for the bilateral group (median (IQR)= 78(33)%) when compared to either the unilateral patients (92(21)%) or the controls (90(18)%), which is probably associated with the inability of the bilateral patients to respond to a vasodilatory challenge. Here, we have not performed any statistical tests between groups since the distribution is bimodal.

Finally, we assessed the LI to capture any specific hemispherical differences (Figure 4.6B). Similar to what we reported earlier in this work, we observed no differences in the number of channels with a vasodilatory response between the two hemispheres, despite the presence of nonnegligible outliers in the bilateral group.

4.4 Discussion

In this work, we employed NIRS to assess the vasodilatory response at the local cerebral microvasculature in patients diagnosed with carotid atherosclerosis. Specifically, we used the breath-holding task for 10 seconds to evaluate the cerebrovascular reactivity at the clinic, which may be seen as a shorter duration when compared to the target 30 s period used in the clinic with TCD. However, our practical experience was that very few patients can actually hold their breath for that long. In our protocol, we confirmed that all patients recruited in this study were able to hold their breath for 10 s. Furthermore, we hypothesized that the local microvasculature assessed by NIRS would have a larger relative response to breath-holding than the relative response in the larger vessels measured with TCD, which would be easier to detect even at a shorter duration.

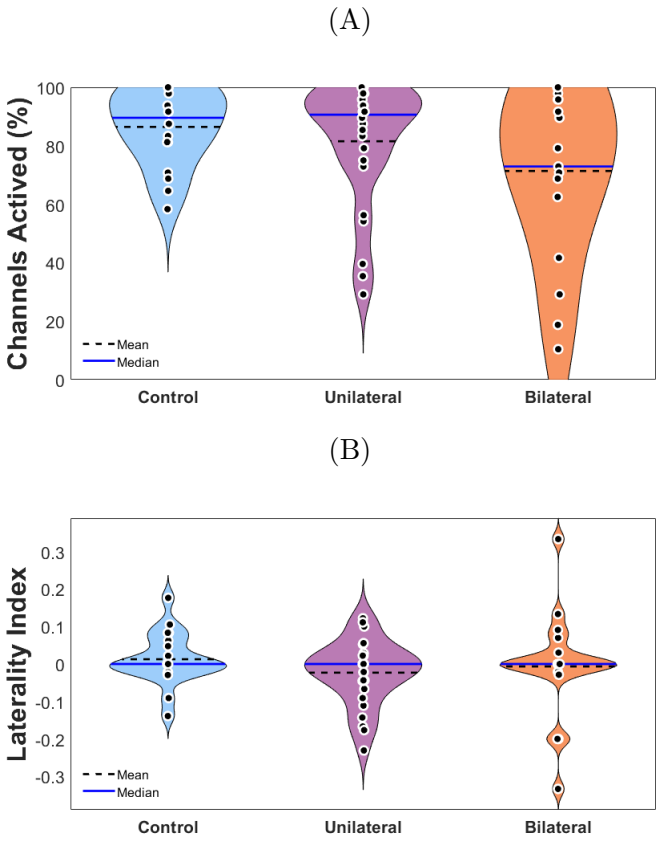

Figure 4.6: **Distribution of** the (A) **actived channels** by breath-holding test and the (b) **laterality index** calculated to assess potential differences across the two hemispheres.

The average time courses support our hypothesis, and we were able to successfully see a significant response correlated with breath-holding at the group (Figures 4.2 and 4.3) and the individual (Figure 4.4) levels.

Like previous studies that performed breath-holding with NIRS, our experimental setup only used long source-detector separations (3 cm). Therefore the optical signal analyzed in this work contains both cerebral and extracerebral contributions, which makes the physiological interpretation of HbO and HbR changes challenging since the interplay of oxygen supply and demand will have different dynamics at different depths. The inability to unentangle cerebral and extracerebral contributions with our NIRS setup was one of the main reasons we focused on HbT changes. The vasodilation induced by the increase in pCO_2 during breath-holding should affect all arterial vessels

(i.e., cerebral and extracerebral) in the same direction to increase blood volume, which would be observed as an increase in HbT everywhere in the brain and outside.

On the other hand, there would be no reason to expect that the vasodilatory mechanisms would coincide at the extracerebral and the cerebral microvasculature. Feedback and feedforward signaling of the neurovascular unit suggest that cerebral vasoreactivity will most likely rise different dynamics at a given instant, significantly affecting the temporal dynamics measured by NIRS. On top of that, it is expected that a disease of vascular origins such as CAS will affect how blood responds to a vasodilatory task and introduce temporal shifts in blood flow and oxygenation throughout the cerebrovasculature. To the best of our knowledge, it is surprising that these effects have never been accounted for in previous studies of NIRS in CAS patients.

Here, we approached the temporal mismatch between the breath-holding onset and its hemodynamic response by introducing a novel methodological approach based on varying the dynamics of the HRF used in the analysis model and quantifying a temporal delay that maximizes the fit of the experimental data with the standard GLM model. By accounting for the different time delays, we were able to detect robust vasodilatory responses across all measured regions of the brain and used this parameter to assess local differences in vasoreactivity with NIRS. In our opinion, the quantification of the time delays appears to be a valuable tool to better understand the limitations of the cerebrovasculature reorganization in CAS patients. Our results suggest that the vasodilatory response is slower in patients. Although a clinical study with a larger number of subjects is needed to confirm this finding, the trends for the association between the presence of carotid atherosclerosis and slower/nonuniform hemodynamic response to vasodilation are clear (Table 3.1).

Across all data analyses, we observed significant heterogeneity within each group, which ended up limiting the power to assess statistical significance with our sample. There are several sources for this heterogeneity. First, introducing a new free parameter in the analysis (time delay) will naturally allow more intrinsic variability in the results and contribute to the overall heterogeneous patterns we reported. On top of this inherent variability, different reasons will increase the variability within the group. The subjects in the control group were selected based on age and gender.

Since we did not perform any diagnostic exam for the presence of atherosclerotic plaques at the ICA, it is possible that some of the subjects in this group have an internal carotid artery stenosis that was not diagnosed, which would explain the few cases with higher time delays we found in this group. In the patients' groups, the confirmed presence of the atherosclerotic plaques and the quantification of the level of the ICA occlusion will eventually force the cerebrovasculature to reorganize itself and develop new functional mechanisms aiming to compensate the lower level of blood going into the brain, as is widely known in this population. It is expected that the available compensatory mechanisms will differ across patients and give rise to a unique cerebrovascular reorganization that can similarly affect the large vessels but will undoubtedly vary at the local microvasculature.

Even with all the heterogeneity, we observed strong and coherent trends that achieved marginal statistical significance. A larger cohort would probably increase the level of confidence in the groups' comparison. However, the individual results shown in Figure 4.4 suggest that by only looking at the group averages, one would miss the richness variability. Indeed, our results indicate that group averaging may not be the best strategy to understand the effects of CAS at the microvascular level and translate findings to individualized clinical care. On the other hand, the methodology presented in this work may open new directions towards the individualized characterization of cerebrovascular deficits due to CAS.

By analyzing the individual patterns, we were able to see that the ability to vasodilate appears to be significantly reduced in patients with both hemispheres affected by CAS. We quantified this observation more accurately by counting the number of NIRS channels that showed a vasodilatory response following breath-holding at different time delays (Figure 4.6). The lower number of channels with a vasodilatory response in the bilateral group is consistent with the hypothesis that patients with severe carotid stenosis are already in a stressed condition of permanent vasodilation as a compensatory mechanism for the lower blood provided by the carotid arteries [184–186]. It is worth noting that, although breath-holding is a global disturbance expected to affect the whole cerebral vasculature, not all NIRS channels yielded a significant change correlated with the task even in the control group. This may be related to the amount of disturbance caused

by vasodilation, which can vary in different brain locations. From the technology perspective, the SNR of channels located in the various areas will also vary. The physiological and technical aspects of the measurement will lead to regions in which our NIRS probe will not have enough sensitivity to identify changes associated with breath-holding robustly.

Since each ICA feeds a different hemisphere, one may expect hemispherical asymmetries in the vasoreactivity response to breath-holding. The disparity between the two hemispheres could be even more expected in the unilateral group since one of the hemispheres provides normal flow to the brain. However, we could not find any observation that supports this hypothesis. We observed similar characteristics in both hemispheres when comparing one given measured region with its homotopic area at the contralateral side. The collateral circulation at the circle of Willis might explain the similarity across both hemispheres. It has been shown that the ACOAs provide collateral channels in patients diagnosed with unilateral ICA [187]. In addition, the carotid blood flow contralateral to the stenosis hemisphere increases to compensate for the decreased perfusion in the ipsilateral side [188]. However, the posterior circulation appears to be demanded entirely only after a severe stenosis occurs [187, 188], which is the case in patients with bilateral carotid stenosis. All these factors will contribute to the reorganization of the cerebral vasculature, which will act collectively as a highly connected system to minimize impaired brain function at the microvasculature.

In the future, the use of NIRS montages with short-channels in a larger cohort focused more on a clinical trial than on a methodological development will allow us to separate the contributions of the extracerebral microvasculature from the cerebral vasculature and further examine the interplay of the temporal blood oxygenation dynamics at different locations.

4.5 Conclusions

Based on NIRS monitoring, this work introduced and validated a novel approach for quantifying the temporal delay of the hemodynamic response to vasodilation. The time delay method clarifies the vasodilatory processes induced by breath-holding (cerebral and extracerebral changes are yet to

be studied). CAS patients take slightly longer than controls to vasodilate and have a more diverse response across different brain areas. Quantification of activated channels in bilateral patients is a measure for vasodilatory capacity and may be used to quantify CAS severity. In CAS patients, we observed no hemispherical variations in local microvascular reactivity.

In this context, we offered a potential solution to the posed question Q1.1: Can NIRS assess cerebral vasoreactivity? In a breath-holding test, we demonstrated that NIRS measures the vasodilatory response at the local cerebral microvasculature in individuals with carotid atherosclerosis. Furthermore, this study adds two new measures for assessing cerebral vasoreactivity. In response to Q1.2, does carotid artery stenosis affect cerebral hemodynamics by hemisphere?, our findings revealed no hemispherical changes in local microvascular responsiveness.

Chapter 5

Assessment of cerebrovascular connectivity in CAS patients

Spontaneous vascular fluctuations are present in the entire body at rest and synchronized at multiple body sites. Network theory has been extensively used to study the synchronization of spontaneous vascular fluctuations in the brain. The mean hypothesis assumes that the brain is a complex system; as a result, it is possible to measure functional connectivity from brain network properties and detect faulty functional connectivity in sick states [189–193]. Considering the hemodynamic altered by a decrease in cerebral perfusion in patients with carotid stenosis, it is reasonable to assume that the spatio-temporal relationships of hemodynamic fluctuations in these patients will be altered too, which should be reflected in the quantification of cerebral connectivity properties. Therefore, we propose to use NIRS to research brain connectivity during rest in individuals with carotid stenosis to better understand how the illness may modify the hemodynamic connections between different brain areas.

This chapter aimed to show how NIRS may measure functional connectivity in CAS patients. We examine the function of systemic contributions in global and local connectivity. We show that the brain may need to restructure itself by increasing the connections between areas.

5.1 Spontaneous hemodynamic fluctuations

Our vascular system presents some spontaneous oscillations at rest, and we can define such a set of global and unconscious circulatory processes that induce variations in the blood pressure at several frequencies [109]. Each band of spontaneous oscillations is associated with different physiological activities. Indeed, frequencies near 1 Hz (P-waves) are associated with heart rate, whereas frequencies near 0.3 Hz (R-waves) are associated with respiration [194]. Spontaneous low-frequency (SLFO) or M-waves (0.1 Hz) are unrelated to heartbeat or respiration but are commonly associated with sympathetic brain oscillations because they increase when the sympathetic nerve is active [107]. The very slow oscillations (VLFOs) or B-waves are present at around 0.03 Hz, they are assumed to reflect regular cerebral blood volume variations caused by different brain stem nuclei [195]. The origin of SLFOs and VLFOs is not fully comprehended. Some discussions suggest that they are a kind of systemic autoregulation mechanism based on regular changes in the vasomotor tone of arterioles and capillaries [196–200].

Previous studies have demonstrated that CAS results in clinically significant neurodegeneration even in asymptomatic patients [13, 17, 143, 144, 201, 202], although the mechanisms underlying deterioration and its long-term impact on cerebral hemodynamics are not completely understood [149]. Impairments in the cerebrovascular reserve are typically used as correlates of neurodegeneration; they are clinically assessed by vasoreactivity tests, which measure the vasculature's ability to respond to a vasodilatory challenge. In general, vasoreactivity tests have shown to be sensitive to CAS severity [40]. However, they do impose challenges concerning patient adhesion to the protocol and high variability at the inter-subject level [203]. In addition, impaired cerebral reactivity measures across different techniques are not well correlated [13], potentially illustrating the heterogeneous nature of the disease.

The brain has several anatomically-programmed compensatory mechanisms to balance blood flow restriction even before they are needed in situations of low cerebrovascular reserve. One example is the blood circulation coming from the communicating arteries in the circle of Willis, where the collateral flow can be reversed to provide additional blood. Considering the hemody-

namic alterations induced by the deficit in cerebral perfusion, it is reasonable to hypothesize that cerebrovascular reorganization due to CAS will have signatures in the spontaneous brain hemodynamics even in the absence of a vasodilatory task. In fact, Diehl et al. reported disparities in cerebral blood flow velocity patterns between patients with internal cerebral artery stenosis and controls using transcranial Doppler (TCD) ultrasound [204].

SLFOs and VLFOs in the brain measured during rest have been widely studied with neuroimaging techniques such as functional magnetic resonance imaging (fMRI) [205] and near-infrared spectroscopy (NIRS) [196]. Current evidence suggests that such resting-state hemodynamic fluctuations are associated with an autoregulation mechanism based on regular changes in the vasomotor tone of arterioles and capillaries [197–200]. They have also been associated with sympathetic brain oscillations [107] and assumed to reflect regular cerebral blood volume variations caused by different brain stem nuclei [195].

Despite the origin of these fluctuations, they appear to be sensitive to impairments in blood oxygenation at the cerebral vasculature. Porcu et al. used fMRI to show that functional hemodynamic connectivity of CAS patients changes following brain revascularization (i.e., carotid endarterectomy), evidencing cerebrovascular reorganization [206]. Our group has previously employed NIRS to describe patterns associated with resting-state functional connectivity in CAS patients, which are different from those reported in healthy subjects [40]. However, it is difficult to comprehend the origins of these fluctuations since both NIRS and fMRI measure blood oxygenation, and therefore are affected by impairments in endothelial function or neurovascular coupling, or both.

This work aimed to analyze cerebrovascular connectivity in CAS patients across different brain regions during the resting state. In particular, we explored the intrinsic property of the NIRS signal to separate the neural and the systemic components and to understand how the disease may alter the hemodynamic relationships between different brain regions.

5.2 Data analysis

Channels whose raw intensity data signal-to-noise ratio (SNR) were lower than eight were removed since they did not contain useful information. Light intensity was transformed to optical density for the remaining channels and then corrected for motion artifacts using a hybrid approach [111]. Then, we used the modified Beer-Lambert equation with a differential pathlength factor of 6 for both wavelengths to estimate HbO_2 and HbR concentration changes. Hemoglobin data were band-pass filtered around low frequencies (i.e., between 0.009 and 0.08 Hz) to remove long-term trends and main high-frequency systemic physiology contributions (i.e., respiration, heart rate, and systolic/diastolic arterial blood pressure oscillations) from the optical signal.

Although the NIRS signal is often associated with a neural signal, it naturally contains both neural and nonneural contributions, given the physical principles of near-infrared light propagation into the head. The nonneural contributions can be both from systemic origin and extrinsic to the brain, such as Mayer waves, and from intrinsic factors originated in subcortical pathways, such as cross-hemispheric vasomotion [207, 208]. To account for the nonneural origins in the data, we further performed a principal component analysis (PCA) regression of the filtered signal. Briefly, PCA decomposes the input data into orthogonal noncolinear components sorted by their covariance; we removed the first principal component from the input data to end up with a signal that minimizes the nonneural contributions to the optical data [132, 209, 210]. Therefore, we hypothesized that the PCA-filtered data primarily contained the neural contribution to the spontaneous hemoglobin concentrations. While the filtered band-pass data mostly contained nonneural contributions (which, in the case of NIRS, are mainly from systemic origin).

Since the high temporal resolution of NIRS results in highly correlated data points, we performed a pre-whitening filtering to remove any temporal autocorrelation in the data before computing the Pearson correlation coefficient, r, between two given channels. The correlation coefficient calculation between every possible combination of two channels resulted in a correlation matrix for each chromophore and volunteer.

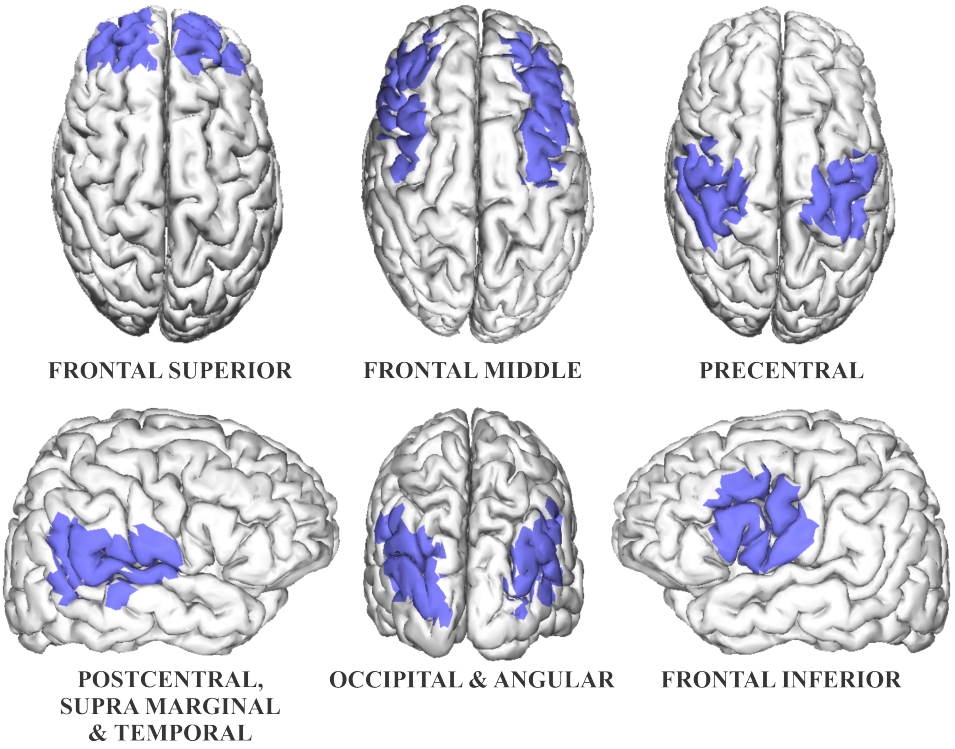

Figure 5.1: **Regions of interest** (ROIs) defined for this study. The definition of each ROI was considered based on the brain sensitivity of the NIRS probe channels

We employed graph theory to build the brain networks from the pre-processed NIRS data. In this approach, each source-detector pair (i.e., channel) can be associated with a node in the graph. The link between two nodes was assigned based on the z-transform of the Pearson correlation coefficient.

In this work, we opted to build a weighted network so that the z-value represents the strength of the connection between two given nodes, w. We ignored the negative correlations for practical reasons and considered only $r \geq 0$. We calculated the average positive node strength for each channel by computing the average connectivity positive weights (denoted by s) of the edges attached to each channel i, i.e., $s_i = \frac{\sum_{i \neq j} w^{+}_{i,j}}{n}$, where n is the number of channels available ($SNR > 8$).

To assess how the connections are distributed locally, we defined 12 regions of interest (ROIs) divided throughout the entire head according to the sensitivity of each NIRS channel (Figure 5.1). The ROIs were hemispherically divided in frontal superior, frontal middle, frontal inferior,

precentral, postcentral, supramarginal & temporal, and occipital & angular. The Atlas Viewer software was used to find the brain sensitivity of each channel [211].

The connectedness of the resting-state networks was computed based on the global properties of the graph by averaging the positive node strength according to the question to be answered (i.e., brain hemispheres, ROIs, or the whole brain) for each chromophore and subject.

We obtained the parameters of interest for each participant for statistical comparison between the groups. Due to the disease's heterogeneity and the small sample size, we performed nonparametric statistical tests to examine differences in topological properties calculated within an ROI. Specifically, we used a two-sided Wilcoxon rank-sum test to evaluate whether two groups have equal medians in the parameter analyzed.

5.3 Results

5.3.1 CAS affects the systemic component of the resting-state hemodynamics

For an overall qualitative description of brain connectivity, Figure 5.3 shows the average connectivity maps obtained from HbO_2 and HbR for each group and in the two conditions analyzed (i.e., with and without the systemic contribution in the NIRS signal). In all cases, the systemic component significantly increased the connectivity across different regions, particularly in the frontal areas. The increase in robust connections is expected since the systemic contribution is global and will affect the whole brain. However, CAS appears to affect brain connectivity across the microvasculature. In the HbO_2 signal, the control group showed a higher number of robust connections when compared with CAS patients. The average number of strong HbO_2 connections (defined as $r \geq 0.3$) was 861, 787, and 736 for controls, unilateral, and bilateral patients. The lack of robust connections in the bilateral CAS patients could be related to differences in transit time of blood flow induced by the presence of plaques, which would lead to desynchronization of the systemic components of blood delivery across different regions and decrease the Pearson correlation at lag

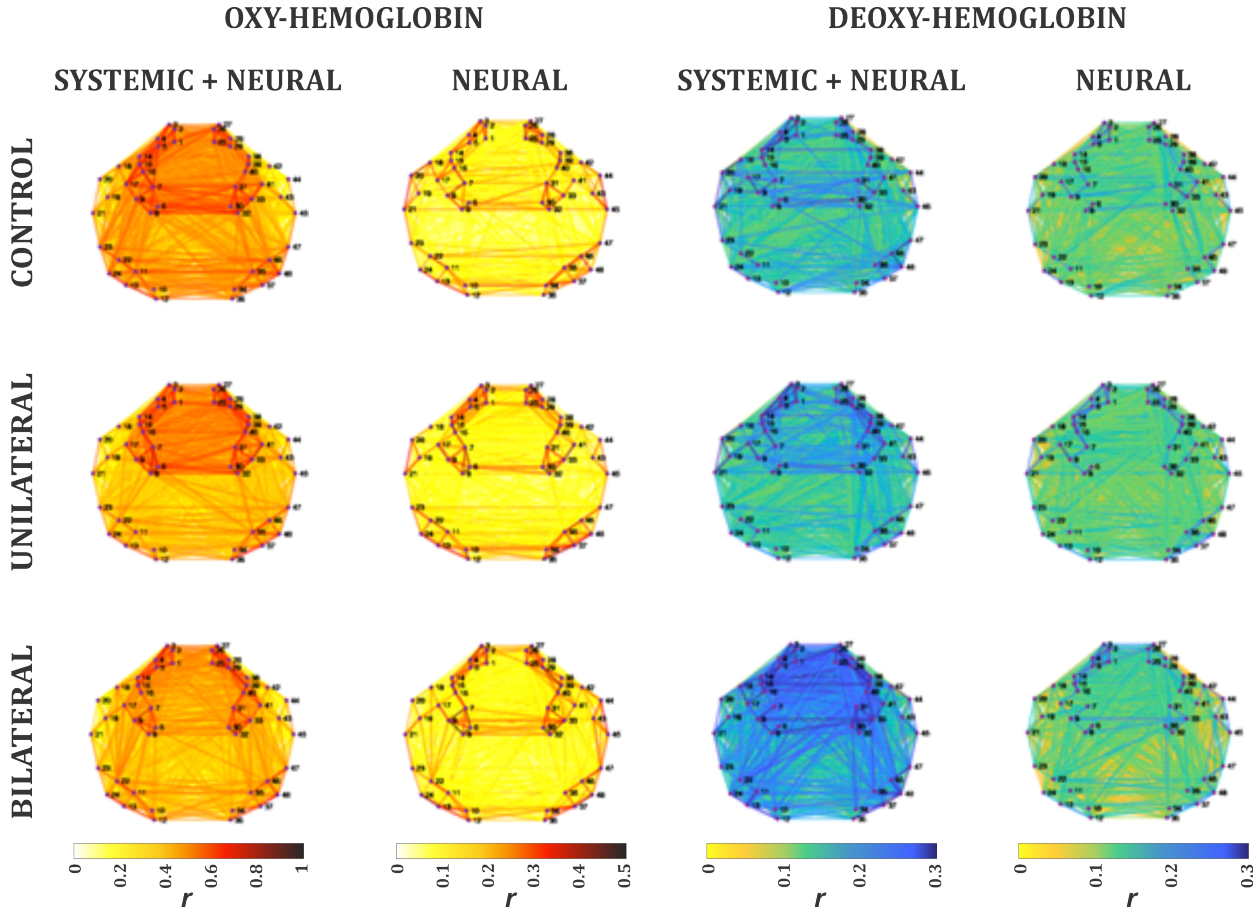

Figure 5.2: **Average weighted network maps by groups** with systemic contributions and removing systemic contributions in the Oxy- and Deoxy-hemoglobin..

zero. Table 5.1 shows the number of strong connections across the different ROIs; it is possible to note that the loss of connectivity was most prominent in the Occipital and Angular area. The situation is reversed when one analyzes the connections through the oxygen extraction signal, as represented by the HbR maps. In this case, the bilateral group is densely connected, with links above a threshold of $r \geq 0.2$, which is 68.5% higher than the number of highly connected links in the unilateral group and 81.3% higher than controls. (Note, we used a lower correlation threshold for HbR because the SNR is significantly lower for this contrast.) This result suggests that CAS might synchronize oxygen demand throughout the brain as an optimization strategy in the situation of inadequate perfusion. The Frontal Middle area was the main region affected (Table 5.2). Concerning the neural component of the signal, we did not observe significant differences

Table 5.1: Number of strong connections originated at different brain regions during blood delivery, as measured by HbO_2.

Group	ROIs Location					
	Frontal Superior	Frontal Middle	Frontal Inferior	Precentral	Postcentral, Supramarginal & Temporal	Occipital & Angular
Systemic + Neural						
Control	263	308	166	197	232	242
Unilateral	213	285	179	203	206	168
Bilateral	225	271	150	177	182	183
Neural						
Control	3	6	3	3	5	2
Unilateral	5	11	4	8	6	4
Bilateral	5	9	2	5	5	4

among the three groups, implying that CAS affects the low-frequency systemic oscillations of the microvasculature, both during oxygen delivery and extraction primarily.

5.3.2 High intra-subject variability suggests different mechanisms of cerebrovascular organization

Although the group results presented clear evidence of alterations in the brain connectivity of systemic origins in patients diagnosed with CAS, the inter-subject variability within each group was relatively high, implying that each subject develops their mechanism to overcome restrictions in blood delivery. Figure 5.3 shows the average positive node strength distribution across all subjects for each group and NIRS contrast. The highest node strength was found for the neural + systemic network in the HbO_2 signal, with an interquartile range (IQR) of 0.3, varying from approximately 0.2 to 0.5. We found no differences in the whole brain connectivity when comparing controls to either unilateral ($p = 0.7$) or bilateral ($p = 0.3$) CAS patients. The high node strength for HbO_2 was also expected since this molecule is mostly found in the arterial side, which is more sensitive to systemic factors. On the other hand, the effect of systemic factors on the venous

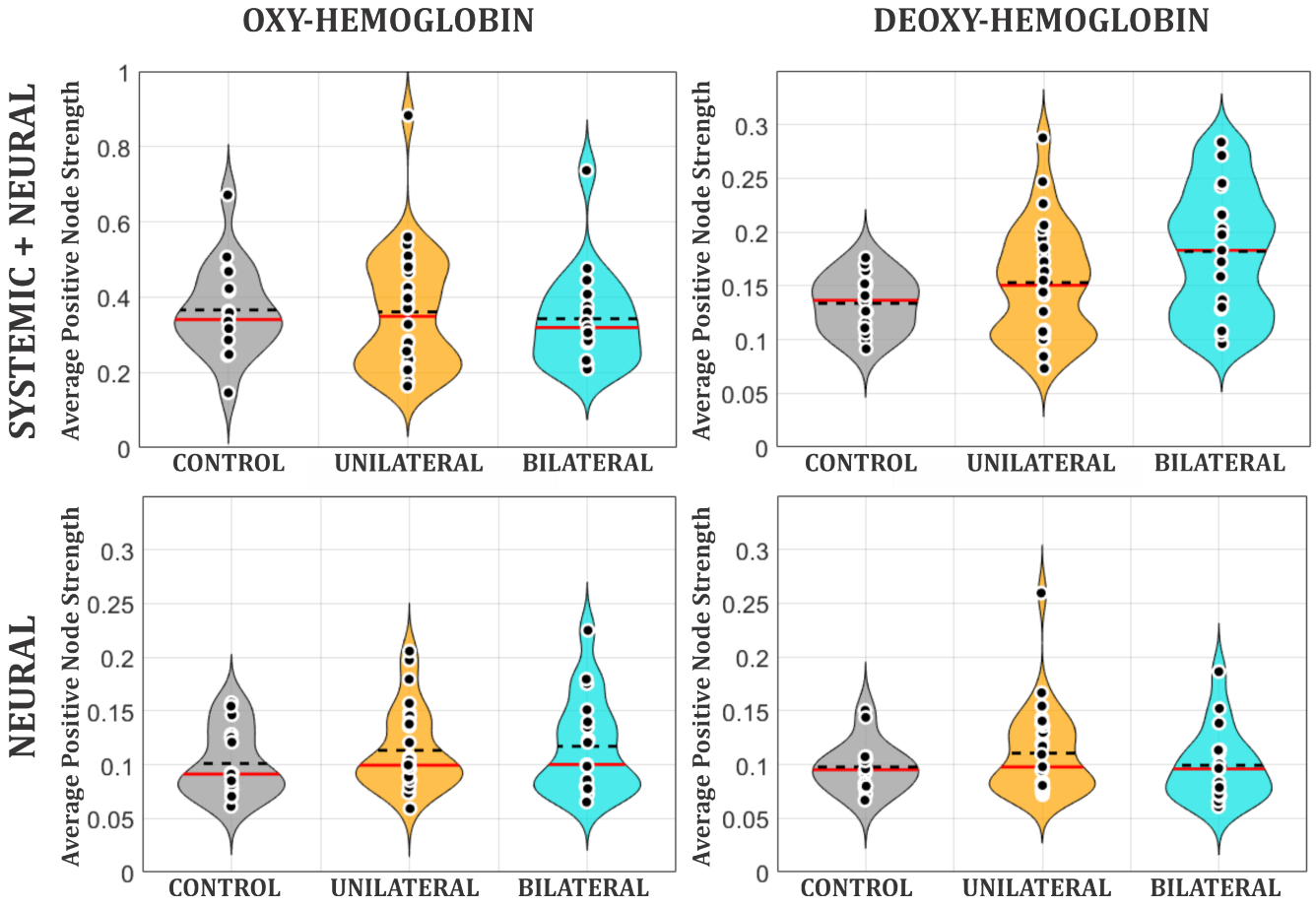

Figure 5.3: **Positive node strength distribution** for each group in the two situations analyzed: systemic + neural (top row) and neural only (bottom row). The networks formed from the oxy-hemoglobin signal (HbO_2, left column) provide a picture of oxygen delivery. In contrast, the deoxy-hemoglobin signal (HbR, right column) data are a proxy to oxygen extraction (therefore, oxygen consumption).

Table 5.2: Number of strong connections originated at different brain regions during blood extraction, as measured by HbR.

Group	ROIs Location					
	Frontal Superior	Frontal Middle	Frontal Inferior	Precentral	Postcentral, Supramarginal & Temporal	Occipital & Angular
Systemic + Neural						
Control	14	25	16	18	17	12
Unilateral	30	59	33	29	14	7
Bilateral	102	153	42	78	69	60
Neural						
Control	5	8	6	5	4	2
Unilateral	11	13	5	4	7	4
Bilateral	8	12	4	5	4	3

side is mild, which is reflected in our data by the lower node strengths in the neural + systemic network in the HbR signal, with averages ranging from 0.14 to 0.18. In this case, the bilateral group has significantly more connections than controls (0.18 ± 0.01 vs. 0.14 ± 0.01, $p = 0.02$) and the unilateral CAS patients (0.15 ± 0.01, $p = 0.1$). The NIRS-based connectivity is drastically reduced when the systemic component is removed in both cases (i.e., HbO_2 and HbR). In this situation, the node strength of the networks varied from 0.09 to 0.11, with no differences among the three studied groups ($p > 0.2$).

5.3.3 Oxygen demand in the anterior circulation is more affected than in other regions

In order to assess local differences across the brain, we calculated the average node strength for each ROI separately (Figure 5.4). Overall, we observed that the most significant differences are located in the superior areas of the frontal lobe (frontal superior, frontal middle, and precentral). Oxygen delivery network appears to be less connected in CAS patients in these areas, while regions more closely located to the blood entrance at the base of the brain (frontal inferior, parietal &

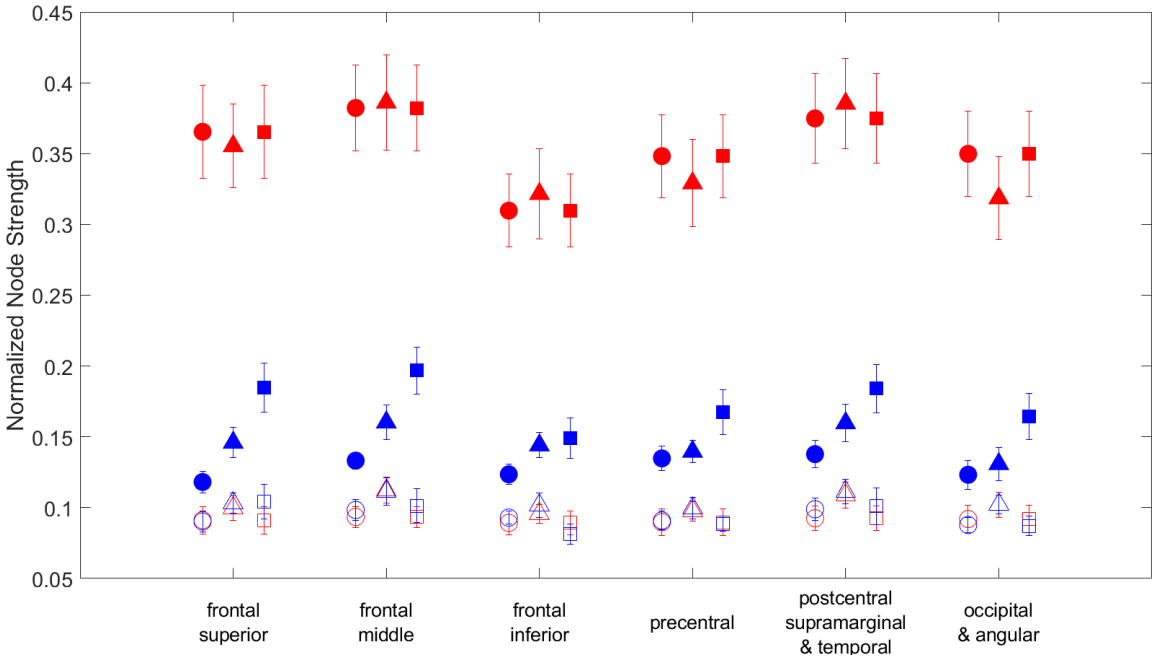

Figure 5.4: **ROIs connectivity distribution**. The circles represent the control group, the triangle represents unilateralism, and the square represents bilateralism. HbO is the red color, and HbR is the blue color. The filled boxes indicate systemic + neural network, whereas the empty boxes represent the neural network

temporal, and occipital & angular) do not show significant connectivity losses. The differences in the oxygen demand network between patients and controls appear to be more explicit and uniform across all regions. They are also present at the neural factor of the resting-state low-frequency oscillations.

The local differences can be better observed by analyzing the relative changes in connectivity in the CAS patients compared to controls (Figure 5.5). Unlike the unilateral group, where changes in connectivity are mild, and mostly under 25% increase relative to controls, the resting-state network of bilateral CAS patients is more robustly connected. The difference to controls grows more prominent as we progress from inferior occipital to superior frontal areas. Surprisingly, Figure 5.5 shows no evidence of hemispherical differences even in patients with unilateral CAS, suggesting that cerebrovascular reorganization is a global phenomenon across the whole brain.

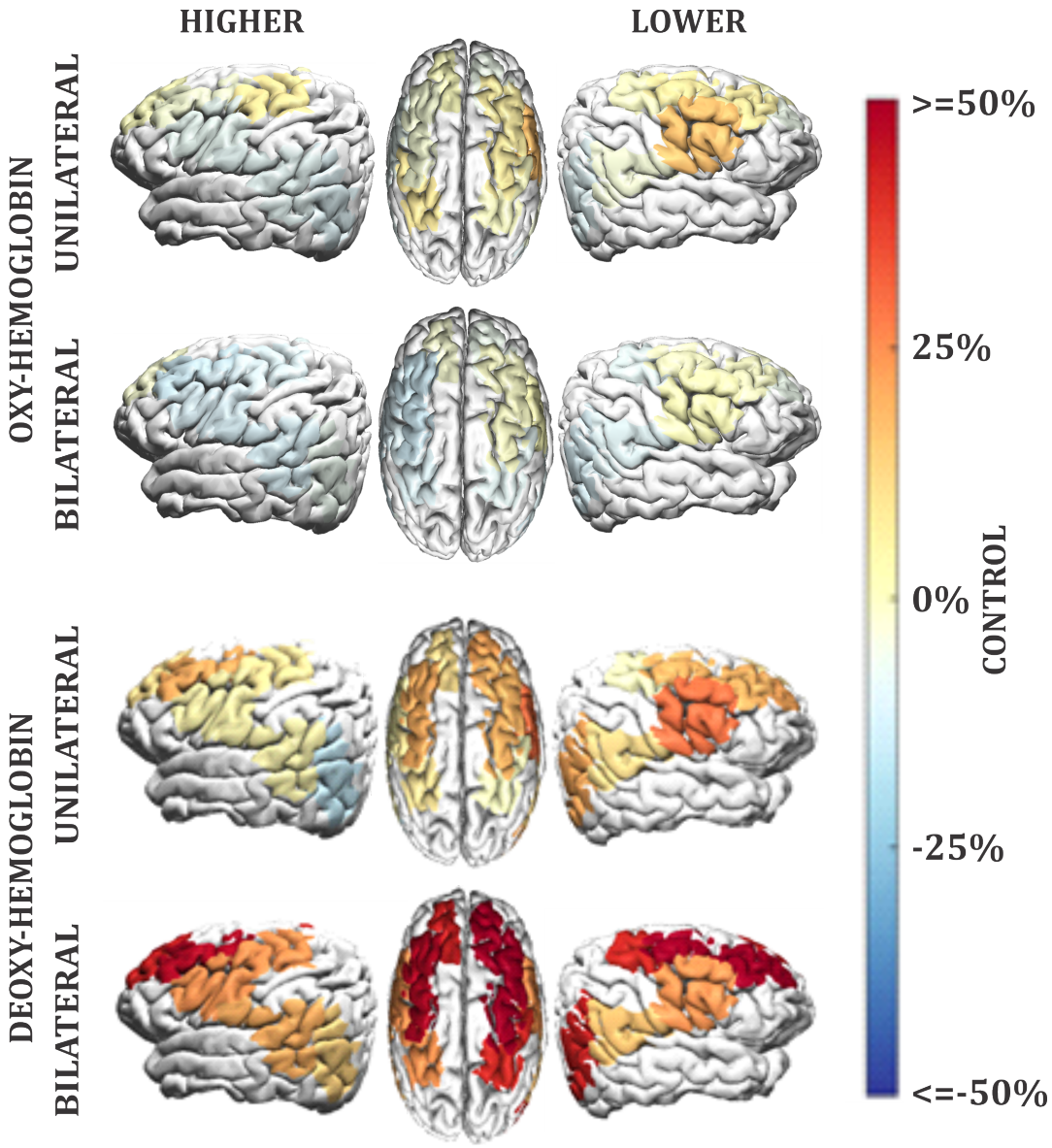

Figure 5.5: **ROIs differences between control and CAS patients** for Oxy- and Deoxy-hemoglobin in systemic +neural networks. Higher and lower correspond to hemispheres with higher and lower stenosis

5.4 Discussion

This study used NIRS to investigate how the perfusion deficit induced by carotid artery atherosclerosis affects cerebrovascular function during the resting state. The brain is a complex system despite local heterogeneity, and the cerebrovasculature is connected in a closed loop with several branches. Therefore, brain hemodynamics across different regions are related to one another and should be analyzed as a whole. In this work, we approached this problem using graph theory to describe the connectivity patterns in CAS patients compared to controls. Although several other parameters could have been used to describe topological features of the network, here we focused on the most fundamental characteristic of any network, i.e., how it was connected. We quantitatively assessed connectivity by calculating the positive node strength at each node. Most resting-state functional connectivity studies performed with neuroimaging techniques aim to find correlates of neural connectivity through hemodynamic measurements. In most cases, the systemic contributions to the hemodynamic fluctuations are ignored, probably because they can hardly be accounted for or are not typically of interest to the main research question. Due to its intrinsic features, NIRS is more sensitive to systemic changes than neural changes. The systemic contribution is treated as physiological noise of no interest in several cases. Over the last decades, significant efforts have been made in the field to isolate the neural contribution by removing systemic/extracerebral changes from the NIRS signal. To date, PCA filtering, as performed in this work, is the most efficient technique available when there are no short channels in the optical probe setup. However, as is shown in this work, comparison of the data before and after PCA filtering, rather than just trashing pre-PCA filtering data, can provide insightful information, particularly in the case of vascular disease.

Another advantage of NIRS is its sensitiveness to both the arterial and venous blood oxygenation, which allows us to examine the roles of oxygen demand by tissue and oxygen delivery to tissue by simultaneously measuring HbR and HbO_2, respectively. Although it is not entirely possible to unentangle the contributions of the different vascular compartments by a single NIRS measurement with centimeter resolution, prior studies have established the close association of NIRS-based HbR measurements with BOLD-fMRI (whose signal mainly originates in the veins

compartments). In contrast, HbO_2 has been associated with ASL-fMRI (predominantly arterial). In this work, we used this approximation to translate our methodology to physiological terms and better comprehend the differences in the networks obtained with each contrast. When applied to patients diagnosed with CAS, we found that our methodological approach provides exciting information that could be readily assessed with a practical technique in a straightforward resting-state protocol. Our findings suggest that the cerebrovascular reorganization induced by CAS affects the spontaneous hemodynamics in the brain at rest and, therefore, could offer a new biomarker for the disease. However, this was true only when we analyzed the neural + systemic signal, suggesting that most differences are from systemic origin, not neural.

By looking at the whole brain, we found that CAS decreases the connectivity of the oxygen delivery across different regions, probably related to differences in blood transit time to reach several locations. In the future, we plan to investigate this hypothesis by exploring the temporal correlations across different nodes at several lags. Concerning the oxygen demand, HbR maps revealed high connectivity as a function of the severity of CAS. The increase in global HbR connectivity in CAS patients could be seen as a response to lower perfusion, as an attempt to optimize oxygen extraction to maintain cerebral metabolism in the brain without huge unbalancing across different regions. In addition, by analyzing the local changes across different ROIs, our results indicate that the oxygen demand connectivity increased the most in more frontal and superior regions. Interestingly, these regions are more distant from the circle of Willis than the inferior regions measured with our probe, suggesting that the physical distance along the vasculature may play a role in neurodegeneration induced by CAS.

Although we believe that more patients are needed to better understand the consequences of atherosclerosis in the brain, our findings enhance the current comprehension of neurodegeneration induced by CAS. More importantly, our work introduces a novel approach based on a portable technique and a simple protocol that any patient can adhere to; this approach can be further explored to assess relevant information about cerebrovascular reorganization following CAS and drive new therapeutics for CAS patients in the future.

5.5 Conclusions

This study investigated the hemodynamic influences of spontaneous hemodynamics in patients diagnosed with carotid artery atherosclerosis using NIRS. We demonstrated that the effects of CAS on the brain can also be investigated during rest, without the need to induce changes with cerebral reactivity tasks that not all patients can perform. The hemodynamic patterns of control and CAS patients were displayed for both HbO_2 and HbR, representing different hemodynamics aspects. The strength of hemodynamic connections was quantitatively assessed by calculating the positive strength node. We found a decrease in connectivity during oxygen delivery and an increase during oxygen extraction as the severity of the CAS increased. These results provide initial evidence of cerebrovascular reorganization following CAS to compensate for lower local cerebral blood flow. The increased cerebrovascular connections in CAS patients are evident when the systemic (rather than the neural) contribution is kept in the NIRS signal. Lastly, we found that the network impairment caused by CAS is not uniform; the discrepancy is more significant in the anterior and superior areas of the brain. Overall, our findings open up new avenues for studying the effects of atherosclerotic disease on the brain with NIRS, and larger-scale clinical studies should corroborate our findings. In the context of this thesis, this work proposes a possible answer to question Q1.4.: how does carotid artery stenosis affect cerebrovascular connectivity in the brain? The connection patterns suggest that CAS mainly affects systemic oxygen metabolism in the brain, increasing systemic HbR connectivity as CAS severity increases. This increase in HbR connection results from vascular reorganization at the systemic level.

Chapter 6

Analysis of microvascular reactivity in patients with severe COVID-19

This chapter discusses the vascular consequences of COVID-19 in severe patients and our efforts to alleviate the situation by employing NIRS to provide relevant clinical information for healthcare professionals at the COVID-specialized intensive care units (ICUs). This work is based on the hypothesis that the muscle response to microvascular reactivity tests can inform about endothelial health and that endothelial dysfunction is associated with the severity of COVID-19.

6.1 A brief overview of COVID-19

The 2019 coronavirus pandemics (COVID-19) is a public health emergency with over 290 million people diagnosed and over 5 million deaths (Jan-04-2022) since the World Health Organization (WHO) declaration on January 30, 2020 [212]. The international community has been trying to accelerate the development of interventions to prevent, diagnose, and treat COVID-19. Among the ten priority thematic research areas defined by WHO, the search for adjuvant and supportive interventions to improve clinical outcomes for infected patients stands out [213].

COVID-19 is a disease caused by a new coronavirus (SARS-CoV-2) whose etiologic agent is an RNA virus related to the same coronavirus family that caused severe acute respiratory syndrome (SARS) in 2003 and the Middle East respiratory syndrome (MERS) in 2012 [214, 215]. The disease's clinical presentation varies from asymptomatic or mild symptoms (80% of cases) to severe pneumonia (15% of cases) [216, 217], characterized by cough, dyspnea and infiltration on chest imaging that is indistinguishable from other viral lung infections [218, 219]. Early in 2020, the need for supplemental oxygen via nasal cannula was required in approximately 50% of hospitalized patients; 30% needed noninvasive mechanical ventilation, and less than 3% depended on invasive mechanical ventilation with or without extracorporeal membrane oxygenation (ECMO) [220].

Acute respiratory distress syndrome (ARDS) is one of the main complications of COVID-19 pneumonia. In general, ARDS is marked by a lung inflammatory process of direct (such as pneumonia, aspiration, or chest trauma) or indirect (such as pancreatitis and hemorrhagic or septic shock) origin. Currently, the clinical diagnostic criteria for ARDS are established by the Berlin definition [221]. Particularly in the most severe cases of COVID-19 infected patients, ARDS affects about 20-30% of patients after approximately eight days [222, 223]; it is estimated that about 93% of patient deaths appear to be related to ARDS [224].

Since ARDS can frequently lead to hypoxemia (i.e., low arterial blood oxygen concentration), the management of adjuvant therapies to improve arterial oxygenation has been key for intensivists. Some of the strategies employed in the ICU to increase arterial oxygenation are prone positioning [225] and external ventilation. However, the use of invasive mechanical ventilation, or even noninvasive ventilation, has long been associated with high mortality rates [226, 227] and long-term sequelae [228, 229] in survivors. Even without the pandemics, ARDS is already commonly diagnosed in 25 to 30% of patients in intensive care units (ICU) who require mechanical ventilation for more than 24 hours [230]. In Brazil, a prospective multicenter study with more than 700 patients revealed ARDS diagnosis in 31% of the patients hospitalized in 45 researched intensive care units (ICUs), with a mortality rate of 52% [231].

The respiratory effects of COVID-19 are mostly known. Some studies report as typical the presence of cardiovascular confusions in this condition, such as myocarditis, myocardial injury,

arrhythmias, vascular inflammation, thromboembolism, and ischemic stroke [24]. But ARDS also causes diffuse alveolar damage, which evolves in well-defined phases [232]. The exudative phase, present mainly during the first week, is defined by capillary crowding and intra-alveolar edema. The second phase, present after the second week, is marked by intense cell proliferation and may result in tissue repair or progression to fibrosis in cases where the lung injury is persistent.

The infection of endothelial cells can lead to vascular endothelium dysfunction and can be associated with these critical situations. The endothelial cells form a vascular inner layer that establishes an essential interface between the circulatory system and the tissue, covering the supply routes. Additionally, the endothelium has endocrine functions that successfully govern vasoreactivity through the release of solutes, liquids, macromolecules, and hormones that regulate territorial blood flow. They also firmly maintain coagulation and fibrinolysis and assume a significant part in the guideline of insusceptible reactions, aggravation, and angiogenesis. Evidence suggests that endothelial dysfunction is a central component of COVID-19, which leads to changes in the blood microcirculation in ARDS [24]. Such changes seem to be correlated with the severity of the disease, and the different clinical outcomes of patients [233–235].

One of the physiological factors used for clinical evaluation of the respiratory health of patients diagnosed with ARDS is the ratio of partial pressure of oxygen (PaO_2) to the fraction of inspired oxygen (FiO_2). However, this ratio has a low ability to predict the clinical outcome of ARDS patients [226]. Moreover, the PaO_2/FiO_2 ratio neglects the impact of ARDS on tissue oxygenation, which should be the goal when choosing adjuvant therapy. The tissue oxygenation can be directly assessed and quantified at the patient's bedside using NIRS during blood microcirculation testing [236, 237]. In particular, the vascular occlusion test (VOT) can be used to measure microvascular reactivity [238–240]. In VOT, the arterial blood supply in a particular region is temporarily obstructed. The rate of decrease in blood oxygen saturation (StO_2) reflects local oxygen consumption [241]. In contrast, the rate of increase in StO_2(i.e., resaturation) after VOT is related to the capacity for post-occlusion microvascular hyperemia [242]. Microvascular reactivity tests such as VOT have been used to show that muscle microcirculation is altered in patients with sepsis, multiple organ dysfunction, trauma, acute heart failure, cardiovascular surgery, or resuscitation

after cardiac arrest [230, 238, 240]. However, the amount of data in ARDS patients is quite limited. Recently, however, Cortés and colleagues showed that monitoring StO_2 with DOS has the potential to predict adverse clinical outcomes in hospitalized patients with ARDS [230].

6.1.1 The HEMOCOVID-19 consortium

This study is part of an international multicentric initiative involving fourteen centers in six countries (Spain, Mexico, USA, Italy, Ireland, and Brazil) called HEMOCOVID-19 and coordinated by the Institute of Photonic Sciences (ICFO, Spain) [243]. The goal is to assess and characterize the peripheral endothelial health of critical COVID-19 patients using CW-NIRS technology into the clinical environment of intensive care to aid physicians in better managing COVID-19 in the severely ill. In Brazil, our lab has coordinated the internal efforts and acquisitions, which have been performed at the Clinical Hospitals of the University of Campinas (HC/UNICAMP) and the School of Medical Sciences at the University of São Paulo (HC/FMUSP). In this thesis, we will only present data collected from the two Brazilian centers.

6.2 Research Design

6.2.1 Population

The local Ethics Committees at the University of Campinas and the University of São Paulo approved this study (CAEE number 34454920.7.0000.5404), and all participants or their primary relatives signed the informed consent form. We enrolled a total of 35 patients with positive diagnosis of COVID-19 (57% male, average age = 57 ± 12 years old) and with ARDS symptoms, who were admitted to the Intensive Care Unit of either hospital. The exclusion criteria included evidence of venous thrombosis, hematoma, or skin lesions in upper peripheral members, hemodynamic instability such as uncorrected arterial hypotension and/or the need for active resuscitation interventions for optimizing blood pressure and/or cardiac output. Measurement of all patients occurred during the first week of admission following hospitalization. In addition, we collected

Table 6.1: **ARDS Patients clinical information**. MAP, mean arterial pressure; SpO_2, pulse-oximetric oxygen saturation; FiO_2, fraction of inspired oxygen

Clinical variables	**mean ± std**
Heart Rate (bpm)	90 ± 20
Systolic BP (mmHg)	100 ± 20
Diastolic BP (mmHg)	70 ± 10
MAP (mmHg)	80 ± 10
Respiratory rate (bpm)	30 ± 10
FiO_2 (%)	60 ± 30
PaO_2 (mmHg)	90 ± 30
SpO_2 (%)	100 ± 3

independent data from 34 healthy adults (38% male, average age = 33 ± 13 years old), with no history of disease or recent medications affecting blood circulation, as a control group.

Table 6.1 shows the main systemic and respiratory parameters measured for the ARDS/COVID-19 group, including heart rate (HR), mean arterial pressure (MAP), respiratory rate (RR), arterial oxygen saturation (SPO_2), the fraction of inspired oxygen administered (FiO_2), arterial partial pressure of oxygen (PaO_2).

6.2.2 NIRS measurements and experimental protocol

All measurements were performed with a commercial CW-NIRS system (PortaMon, Artinis Medical Systems, Elst, The Netherlands, www.artinis.com) to standardize any potential systematic errors across all centers in the multicentric trial. Briefly, this NIRS device is portable, wireless, battery-operated, and works with three LED sources at distances of 30, 35, and 40 mm from one single detector. Each source is composed of 760 and 850 nm wavelengths. It has a capacity for continuous monitoring with a temporal resolution of 0.1 s by ∼2 hours [244]. This system is based on spatially resolved spectroscopy to infer the absolute values of local StO_2 (Section 2.2.2).

The optical probe was positioned on the forearm's brachioradialis muscle to monitor the muscle hemodynamics during a vascular occlusion test (VOT) protocol. The VOT is a noninvasive proce-

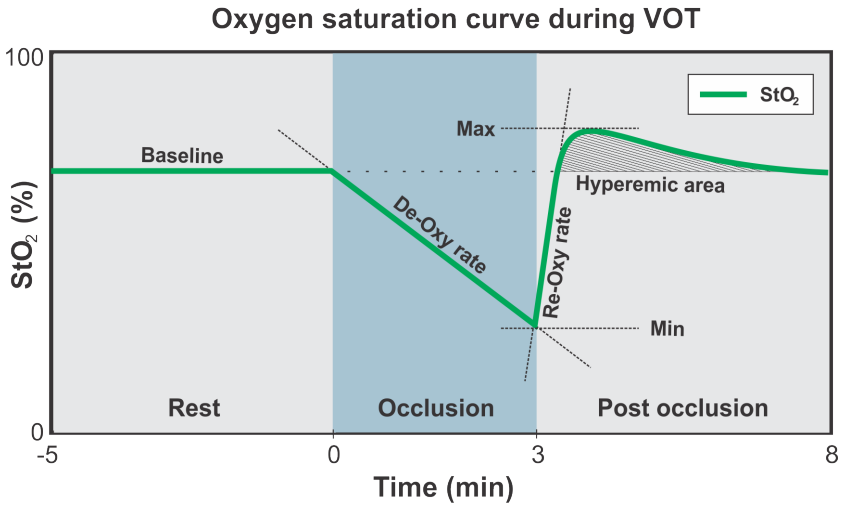

Figure 6.1: The **Oxygen saturation curve during VOT** contains relevant hemodynamic information about endothelial health

dure to stimulate muscular consumption of tissue oxygen and vasoreactivity in the limbs. Briefly, the VOT occludes the forearm's blood supply with a blood pressure cuff inflated to 50 mmHg above the systolic pressure for 3 minutes, at which time the cuff is deflated. The experimental protocol started with 5 minutes of rest to record the baseline period followed by the 3-min VOT and with 5 minutes of recovery following the cuff release. The behavior of StO_2 resulting from the application of the protocol is represented in figure 6.1. It is possible to obtain the de-oxygenation (De-Oxy) and re-oxygenation (Re-Oxy) rates from the StO_2 curves. The De-Oxy and Re-Oxy rates are related to muscle oxygen metabolism rate and the microvascular reactivity, respectively. (Note, the latter depends on the endothelial function.) Also, it is possible to estimate the hyperemic response by computing the area under the overshoot region post occlusion.

6.2.3 NIRS Data Analysis

First, we verified the signal quality of each volunteer and discarded the optical data with an unstable baseline of StO_2 due to the strong influence of artifact motion or poor sensor-tissue coupling. Likewise, we removed optical data that did not respond to VOT because of inadequate occlusion with blood drain. The light intensity of the excellent signal was converted to optical

density, then, the slope of optical density versus source-detector distances was measured. The reduced scattering coefficient was defined as $\mu_s^{'} = k(1 - h\lambda)$, and for the forearm, we used $k = 1.1MM^{-1}$ and $h = 4.6 \times 10^{-4} NM^{-1}$ [75]. Accepting that tissue is homogeneous, and the scattering coefficient is steady during the measurement, the slope determined the absorption coefficient. Next, we calculated absolute HbO_2 and HbR concentrations and then the tissue saturation oxygen using equation 2.1.12. From StO_2, we inferred the dynamic parameters during VOT. Three states form VOT, 1) five minutes of rest guarantee the basal oxygen saturation and this is estimated as the mean of StO_2 during this period. 2) three minutes of occlusion bring out a controlled ischemic condition, evidencing the local metabolism; consequently, we have access to the de-oxygenation rate from the StO_2 decreasing during this period, and the minimum StO_2 value reached. 3) Five minutes of post occlusion evidence the endothelial health by accessing the re-oxygenation rate estimated from StO_2 increasing, the maximum StO_2 value reached during the post occlusion period, the ΔStO_2 defined as $StO_2^{max} - StO_2^{min}$, and the hyperemic response that corresponds to the blood overshot compared with basal StO_2 and is calculated as the area under the curve. We used robust linear regression to compute the slopes to assess De-Oxy and Re-Oxy rates. For the De-Oxy rate, we used the occlusion interval. Furthermore, for the Re-Oxy rate, we limited the interval between the beginning of post occlusion to the time to reach the basal StO_2. The hyperemic area was calculated using the trapezoidal numerical integration that computes the approximate integral of the hyperemic region via the trapezoidal method. The hyperemic region was defined as the interval between reaching the basal StO_2 and three minutes after.

We separated the VOT parameters of each volunteer and compared the control and COVID-19 groups by statistical analysis. Due to the small samples size and the difference between the mean and median values of some VOT parameters, we performed a paired two-sided nonparametric statistical test called Wilcoxon rank-sum test. We subclassified the COVID-19 subjects into two groups depending on ARDS severity, defined by the SpO_2/FiO_2 ratio. The mild and moderate group is formed by patients with a SpO_2/FiO_2 ratio $>= 144$, and the severe group are patients with SpO_2/FiO_2 ratio < 144 [245]. The statistical comparison of ARDS severity groups was based on the Wilcoxon rank-sum test.

6.3 Results

6.3.1 Comparison of COVID-19 patients with healthy controls

The distribution of all microvascular hemodynamics parameters measured during VOT is shown in Figure 6.2 for the two groups, and the results are also summarized in Table 6.2. Figure 6.2A depicts the baseline saturation distribution, which was basically the same for patients and controls; the median (interquartile range) was 70% (6%) and 70% (11%) for the control subjects and patients with COVID-19 groups, respectively ($p = 0.45$).

Figures 6.2B and 6.2E depict the dynamics during occlusion. The de-oxygenation rate was used to quantify oxygen extraction, which is linked to local muscle metabolism. The control group had a median decrease of -8 (3) $\%/min$, which was significantly slower than the -5 (2) $\%/min$ found for the COVID-19 group (p = 0.0001). The minimum oxygen saturation obtained during the occlusion was similar for both groups, however, with median values around 50% (p = 0.09), but with a higher heterogeneity (as measured by the interquartile range) in the COVID-19 patients.

In the post occlusion phase, the dynamic is more related to the blood regulation mechanism at the microvascular level and the endothelial state. Figures 6.2C, 6.2D, 6.2F, and 6.2G show the oxygen saturation dynamics after the cuff release and oxygen supply to the posterior regions. Endothelial regulation was inferred by the re-oxygenation rate and the hyperemic region on the oxygen saturation curve. We found significant differences ($p < 10^{-5}$) between the median re-oxygenation rate of the control group (70 %/min) and the COVID-19 patients (40 $\%/min$), with IQRs of 30 and 70 $\%/min$, respectively. The hyperemic area was also greater in controls than in COVID-19 patients ($p < 10^{-5}$), indicative of endothelial disfunction in COVID-19 patients. In addition, the maximum oxygen saturation value and the variation of saturation by COVID-19 patients was lower than the control group ($p < 0.001$).

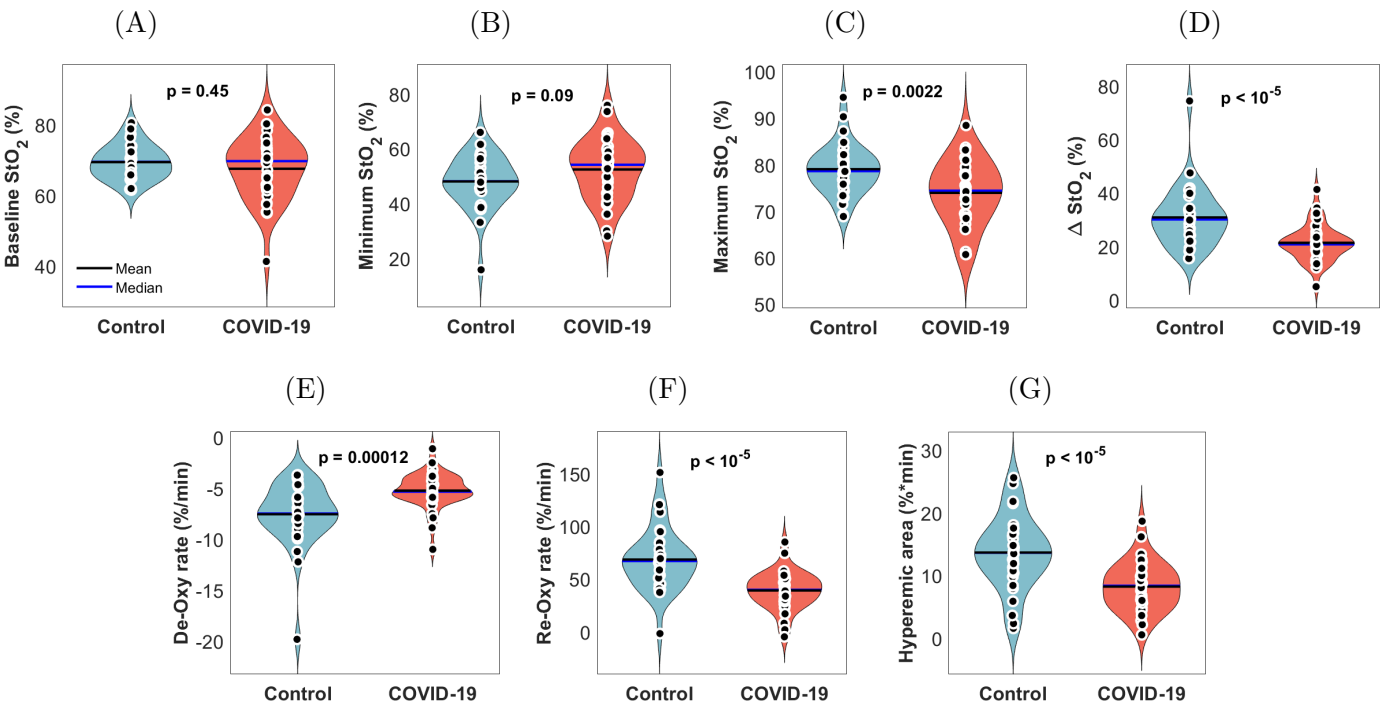

Figure 6.2: The distribution of **hemodynamics parameters** during VOT by groups. The black and blue solid lines show the mean and median values respectively, for the control group (blue distribution) and Covid-19 patients (red distribution).

Table 6.2: **Results of hemodynamic parameters** during VOT

VOT parameters	Control (n = 34)	COVID-19 (n = 35)	p values
	Median (IQR)	Median (IQR)	
Basal StO_2 (%)	70(6)	70(10)	0.45
De-Oxygenation $(\%/min)$	$-8(3)$	$-5(2)$	$< 10^{-4}$
Minimum StO_2 (%)	50(10)	50(20)	0.09
Re-Oxygenation $(\%/min)$	70(30)	40(20)	$< 10^{-5}$
Maximum StO_2 (%)	79(6)	74(9)	$< 10^{-3}$
ΔStO_2 (%)	30(10)	21(7)	$< 10^{-5}$
Hyperemic area$(\% * min)$	14(6)	8(5)	$< 10^{-5}$

6.3.2 Severity correlates of COVID-19

To investigate the effects of ARDS severity on the NIRS data during the VOT, we divided the COVID-19 patients into mild and moderate (34%) and severe (34%) based on SpO_2/FiO_2 rate. We excluded from the analysis patients who did not have SpO_2 or FiO_2 information in the database (32%). Figure 6.3 depicts the distribution of the NIRS parameters measured during VOT. As can be seen from the figure, the median values of all hemodynamic parameters in mild and moderate patients are comparable to those in the severe group.

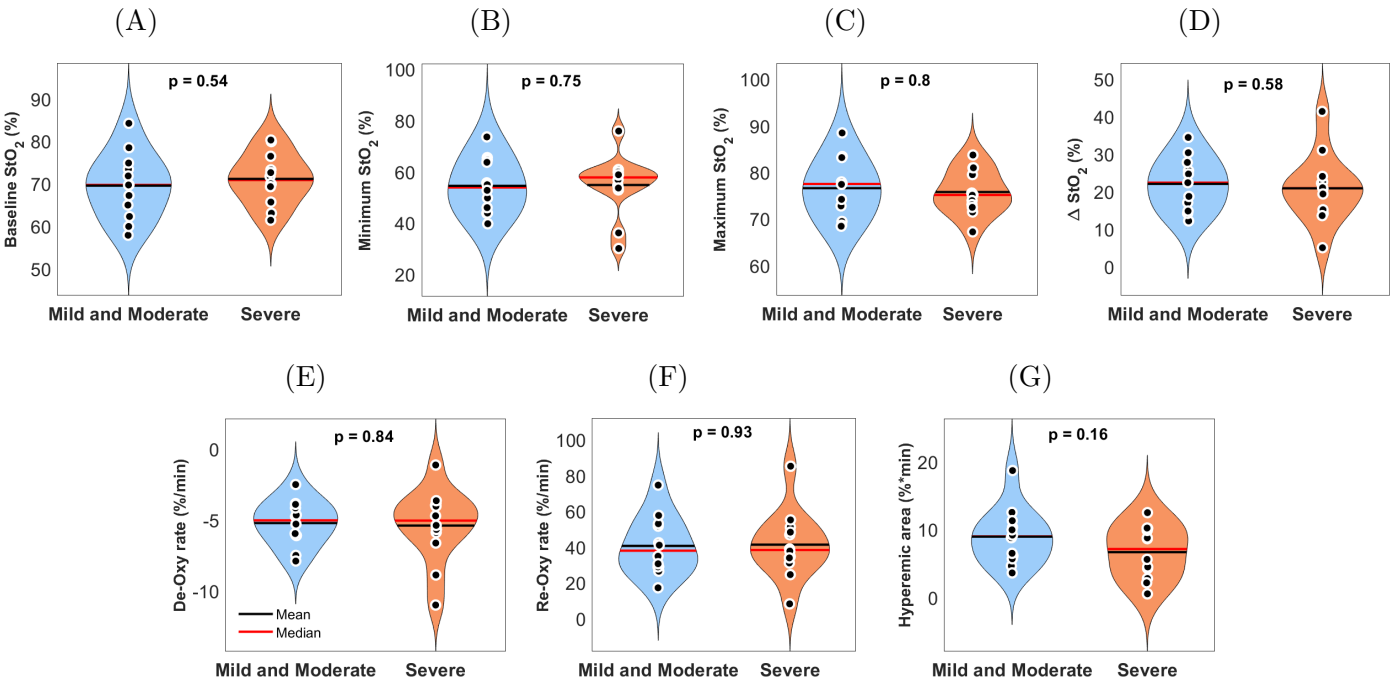

Figure 6.3: The distribution of **hemodynamics parameters by ARDS severity** during VOT. The black and red solid lines show the mean and median values respectively, for mild and moderate ARDS (blue distribution) and severe ARDS (orange distribution).

6.4 Discussion

This study aimed to analyze potential changes in the peripheral microvasculature status in patients diagnosed with COVID-19 and hospitalized with ARDS symptoms at the ICU of two

main hospitals in Brazil. The simplicity with which the microvasculature function may be assessed with NIRS under critical situations is a big advantage towards patient monitoring in critical care. Futhermore, optical techniques have been reliable and safe clinical instruments for patient monitoring.

Overalll, our findings confirm a link between COVID-19 and muscle physiology disfunction which can be used to predict adverse outcomes. Our hypothesis is that endothelial dysfunction causes a change in the vascular balance by increasing microvascular resistivity followed by endothelitis and resulting in a serious vascular condition [246]. Consistent with this hypothesis, we observed poor microvascular reactivity in the braquiorradial muscle. Clinical endothelial damage is clearly seen in the advanced phases of the illness, which is produced by the direct viral infection of the endothelial cells and excessive systemic virus-mediated activation of immune cells [24, 247].

The respiratory deficit caused by ARDS forces severe COVID-19 patients to be attached to some form of respiratory assistance. This fact probably explains the similarity of tissue saturation during baseline when compared to healthy controls. As a result, NIRS-based real-time monitoring of baseline oxygen saturation of the muscle may be used to assess the respiratory state of patients. However, it is not sufficient for detecting endothelium abnormalities, which are the most common causes of complications (and even death) in severe Covid-19 patients [248]. An important point to mention is the fact that the de-oxygenation and re-oxygenation rates from a simple VOT appear to be sensitive to endothelium disfunction and therefore could be employed as biomarkers to monitor endothelial state under critical situations. In addition, VOT parameters assessed by NIRS could help focusing therapy efforts on drugs that protect the endothelium or mitigate endothelial dysfunction's repercussions.

We also attempted to evaluated the influence of respiratory severity on the microvascular reactivity measured with NIRS during the VOT. Using our Brazilian cohort, we observed no differences between mild/moderate and severe cases. The low sample size of mild and moderate cases forced us to group these two conditions under the same group for statistical power, which is not ideal since the criteria of mild and moderate cases represent different clinical conditions. However, using a larger dataset ($n = 73$) with data from all centers of the HEMOCOVID-19 trial, Mesquida et

al. were able to find differences between mild, moderate, and severe cases. Although we could not find it in a smaller sample, this result is of practical importance because it demonstrates the NIRS-based VOT test is sensitive to the severity. In this protocol, the hemodynamic parameters associated with endothelial dysfunction were measured only at a single point for the first week after admission, but the protocol could be easily extended to longitudinal monitoring to assess the patient evolution over time by assuming that the parameters are sensitive to the severity of the disease.

Due to the fact that the severe cases were more prevalent in the elderly population, our patient sample is biased towards older ages. For this reason, we did not analyze the relationship between age and endothelial dysfunction. It also favored age to be accounted as a cofactor in the group comparison, since we avoided exposing healthy elderly subjects to this research project.

6.5 Conclusions

The hemodynamic monitoring during VOT revealed endothelial impairment in severe COVID-19 patients with ARDS admitted in the ICUs. In particular, COVID-19 patients appear to recover more slowly from minor saturation changes than healthy controls, implying weaker microvascular reactivity and metabolic capacity.

In this context, we addressed Q2.1: Is it possible to use near-infrared spectroscopy to evaluate endothelium state in severe COVID-19 patients? We demonstrated that NIRS measures microvascular muscle hemodynamics in severe COVID-19 patients, and we evidenced endothelium status using a vascular occlusion test. In response to Q2.2, Is the severity of COVID-19 linked to endothelial state? Our findings did not reveal a link between COVID-19 severity and endothelial reactivity, but the evidence integrating all HEMOCOVID-19 consortium data appears to point to the fact that the answer to this question is also true [249].

Chapter 7

Conclusions and future perspectives

In this work, near-infrared spectroscopy (NIRS) was employed to assess tissue hemodynamics in two specific diseases where microvascular reactivity plays an important role: carotid artery stenosis and COVID-19. Throughout the different experimental protocols and situations, we successfully translated the technique to different settings in a hospital, from the regular clinic to the intensive care unit. In adittion the high heterogeneity across CAS patients, we quantified cerebral vasoreactivity during a breath-holding task with NIRS to show that temporal delays can provide a biomarker for neurodegeneration in CAS. Despite the clinical use of cerebral vasoreactivity, we showed that the effects of CAS can be seen even at rest in a more straightforward protocol. Unexpectedly, our combined results suggest that CAS has consequences in the microsvaculature at both hemispheres. We also provided evidence that endothelium function is affected in severe COVID-19 patients. Overall, this work shows that NIRS is sensitive to changes in the local microvasculature and illustrates how NIRS measures can offer insightful information for understanding the interplay between local blood oxygen supply and demand. These steps are helpful towards the goal of treating vascular dysfunctions better.

In patients diagnosed with carotid artery stenosis, we used NIRS to evaluate the vasodilatory response at the local cerebral microvasculature from a breath-holding challenge for 10 seconds in the clinic. We characterized the hemodynamics in healthy subjects for understanding the patient's

hemodynamic response to the test. We showed how vasodilation increases cerebral blood volume across the vasculature. Although the dynamics of the vasodilatory response in unilateral stenosis CAS patients was comparable to those of controls, the temporal discrepancies indicated that stenosis affects blood supply at the microvasculature and affect the balancing metabolic demand and vasodilation. In addition, we found a lack of vasodilatation response to the apnea challenge in most bilateral stenosis individuals. Therefore, we showed the temporal dynamics of the hemodynamic response to breath-holding of HbO_2, HbR, and HbT in controls and how CAS modifies it according to stenosis severity. We also introduced a novel parameter to characterize the hemodynamic response delay based on the general linear model. We observed a uniform and significant increase in HbT delayed between 1 and 3 s across all channels for most healthy subjects. The unilateral stenosis patients responded globally but were not uniform and delayed between 3 and 6 seconds. In bilateral individuals, this pattern was also seen. However, over half of the bilateral patients had no vasodilatory response in a significant part of the brain. We also evaluated the brain's vasodilatory capabilities by quantifying the proportion of channels with a substantial response in the NIRS probe and revealed the bilateral patients' failure to respond to a vasodilatory challenge. When comparing the brain hemodynamics across hemispheres, we found no significant changes associated with the vasoreactivity test in both patient groups. While stenosis impairs the local regulation, the systemic regulation of the vascular system appears to ensure brain function. As a result, we demonstrated that the effects of carotid artery stenosis on cerebral systemic hemodynamics could be studied at rest and that vascular reorganization increases patients' hemodynamic connections across different brain regions with systemic origins (rather than neural origins) and is visible in blood oxygen extraction (not oxygen delivery). Finally, we demonstrated that network impairment caused by CAS is not uniform; the discrepancy is more significant in the anterior and superior areas of the brain.

In hospitalized patients diagnosed with COVID-19, we showed the potential of NIRS to determine the state of the peripheral microvasculature based on a vascular occlusion test. When COVID-19 patients were compared to healthy controls, we observed equivalent baseline saturation but impaired metabolism and microvascular reactivity in the braquiorradial muscle. In addition,

we discovered that the hyperemic region was more prominent in controls than in COVID-19 patients. We also investigated the effects of ARDS severity on the NIRS data during the vascular occlusion test and demonstrated that microvascular reactivity is dependent on ARDS severity.

Notably, the advances in this work pioneered NIRS as a potential tool to be used in hospitals and strengthened our collaboration with clinicians, vascular surgeons, and intensivists. This partnership will open the doors to new clinical challenges related to carotid stenosis and COVID-19, as well as other diseases in which NIRS can be helpful. We believe that NIRS monitoring should be considered a valuable tool in the clinic for vascular illnesses or conditions that indirectly induce vascular impairments. The fact that the technique is non-invasive, safe, and portable can facilitate its translation to surgical rooms and other critical environments. Furthermore, it is accurate and sensitive, making it reliable. Also, it is cheap enough to be scalable.

This study has some limitations. For example, in CAS and COVID-19 studies, we have a low number of volunteers recruited, moreover, the statistical significance may be below. In the CAS study, the NIRS system is only sensitive to hemodynamic changes in oxy- and deoxyhemoglobin. Therefore, we do not have access to absolute values, so the minimum and maximum values reached are unknown. This kind of information also has a significant clinical role, as it helps for the propose of reference values for brain hemodynamics in both healthy and CAS patients. Additionally, information about blood flow is not possible to be measured with NIRS, for this, it is needed to add another optical technique as diffuse correlation spectroscopy [41, 250] or speckle contrast optical spectroscopy [251, 252]. We also demonstrated that NIRS can measure "short" breath-holding stimulations (10 seconds), but we discovered that the recovery period should be longer than 30 seconds because some hemodynamic responses are very slow and may require more time to return to baseline, particularly in patients with bilateral CAS. This is a problem that primarily affects the block average analysis. For the COVID-19 study, all VOT results and discussions about the endothelial functionality are based on a small area of the muscle measured, without comparison to other regions.

We expect that this effort will be continued and expanded in the future. One crucial task will consist in increasing the number of patients in both protocols to drive statistically significant clinical results. As the microvascular blood flow is a direct hemodynamic parameter to evaluate regulation and NIRS is not sensitive to blood flow, we propose adding measurements from diffuse correlation spectroscopy (DCS) to improve this work. Because the resting-state protocol is not only simpler than task-based acquisition approaches in carotid artery stenosis, but it can also reveal functionally and spatially distinct modes with greater biological interpretability, we propose evaluating more network parameters that allow bringing more information about the disease's effects. In addition, we suggest that this study be expanded to include endarterectomy because NIRS can monitor the cerebral hemodynamic status in real-time without hindering the surgical process and can help identifying possible stroke events. Hence, we propose monitoring cerebral hemodynamics during clamping and posterior blood reperfusion to assess cerebral autoregulation. It is worth noting that we had this in mind, but the pandemics stopped us from finishing this part. Finally, we believe that this work will provide future generations with the chance to explore clinical concerns with NIRS in Brazil.

References

1. Bianconi, E. *et al.* An estimation of the number of cells in the human body. *Annals of Human Biology* **40.** Publisher: Taylor & Francis _eprint: https://doi.org/10.3109/03014460.2013.807878, 463–471. ISSN: 0301-4460 (Nov. 1, 2013).

2. Malpas, S. C. Neural influences on cardiovascular variability: possibilities and pitfalls. *American Journal of Physiology-Heart and Circulatory Physiology* **282.** Publisher: American Physiological Society, H6–H20. ISSN: 0363-6135 (Jan. 1, 2002).

3. Clifford, P. S. Local control of blood flow. *Advances in Physiology Education* **35.** Publisher: American Physiological Society, 5–15. ISSN: 1043-4046 (Mar. 1, 2011).

4. Sanders, K. M. & Koh, S. D. in *Current Topics in Membranes* (ed Hamill, O. P.) 511–540 (Academic Press, Jan. 1, 2007). doi:10.1016/S1063-5823(06)59020-9. <https://www.sciencedirect.com/science/article/pii/S1063582306590209> (visited on 12/31/2021).

5. Haddy, F. J. & Scott, J. B. Metabolically linked vasoactive chemicals in local regulation of blood flow. *Physiological Reviews* **48.** Publisher: American Physiological Society, 688–707. ISSN: 0031-9333 (Oct. 1, 1968).

6. Krüger-Genge, A., Blocki, A., Franke, R.-P. & Jung, F. Vascular Endothelial Cell Biology: An Update. *International Journal of Molecular Sciences* **20.** Number: 18 Publisher: Multidisciplinary Digital Publishing Institute, 4411 (Jan. 2019).

7. Pittman, R. N. *Regulation of Tissue Oxygenation* <http://www.ncbi.nlm.nih.gov/books/NBK54104/> (visited on 11/23/2021) (Morgan & Claypool Life Sciences, San Rafael (CA), 2011).

8. Roger, V. L. *et al.* Heart Disease and Stroke Statistics—2012 Update. *Circulation* **125,** e2–e220. ISSN: 0009-7322 (Jan. 3, 2012).

9. Ritchie, H. *Does the news reflect what we die from?* Our World in Data. <https://ourworldindata.org/does-the-news-reflect-what-we-die-from> (2022).

10. WHO. *Cardiovascular diseases* <https://www.who.int/westernpacific/health-topics/cardiovascular-diseases> (2021).

11. Brown, D. L. *et al.* Projected costs of ischemic stroke in the United States. *Neurology* **67.** Publisher: Wolters Kluwer Health, Inc. on behalf of the American Academy of Neurology Section: Articles, 1390–1395. ISSN: 0028-3878, 1526-632X (Oct. 24, 2006).

12. Flaherty, M. L. *et al.* Carotid Artery Stenosis as a Cause of Stroke. *Neuroepidemiology* **40,** 36–41. ISSN: 0251-5350 (2013).

13. Marshall, R. S. *et al.* Dissociation among hemodynamic measures in asymptomatic high grade carotid artery stenosis. *Journal of the neurological sciences* **367,** 143–147. ISSN: 0022-510X (Aug. 15, 2016).

14. Marshall, R. *et al.* Cerebral hemodynamics and cognitive impairment. *Neurology* **78,** 250–255. ISSN: 0028-3878 (Jan. 24, 2012).

15. Gupta, A. & Marshall, R. S. Moving beyond luminal stenosis: imaging strategies for stroke prevention in asymptomatic carotid stenosis. *Cerebrovascular Diseases (Basel, Switzerland)* **39,** 253–261. ISSN: 1421-9786 (2015).

16. Dempsey, R. J., Vemuganti, R., Varghese, T. & Hermann, B. P. A Review of Carotid Atherosclerosis and Vascular Cognitive Decline: A New Understanding of the Keys to Symptomology. *Neurosurgery* **67,** 484–494. ISSN: 0148-396X (Aug. 2010).

17. Balestrini, S. *et al.* Severe carotid stenosis and impaired cerebral hemodynamics can influence cognitive deterioration. *Neurology* **80,** 2145–2150. ISSN: 1526-632X (June 4, 2013).

18. Krejci, J., Mlejnek, D., Sochorova, D. & Nemec, P. Inflammatory Cardiomyopathy: A Current View on the Pathophysiology, Diagnosis, and Treatment. *BioMed Research International* **2016,** 4087632. ISSN: 2314-6133 (2016).

19. Kang, M. & An, J. in *StatPearls* (StatPearls Publishing, Treasure Island (FL), 2021). <http://www.ncbi.nlm.nih.gov/books/NBK459259/> (visited on 12/30/2021).

20. Fosse, J. H., Haraldsen, G., Falk, K. & Edelmann, R. Endothelial Cells in Emerging Viral Infections. *Frontiers in Cardiovascular Medicine* **8,** 95. ISSN: 2297-055X (2021).

21. Varga, Z. *et al.* Endothelial cell infection and endotheliitis in COVID-19. *The Lancet* **395,** 1417–1418. ISSN: 0140-6736 (May 2, 2020).

22. Ackermann, M. *et al.* Pulmonary Vascular Endothelialitis, Thrombosis, and Angiogenesis in Covid-19. *New England Journal of Medicine.* Publisher: Massachusetts Medical Society. doi:10/ggwtrb. <https://www.nejm.org/doi/10.1056/NEJMoa2015432> (visited on 12/30/2021) (May 21, 2020).

23. Wazny, V., Siau, A., Wu, K. X. & Cheung, C. Vascular underpinning of COVID-19. *Open Biology* **10.** Publisher: Royal Society, 200208.

24. Evans, P. C. *et al.* Endothelial dysfunction in COVID-19: a position paper of the ESC Working Group for Atherosclerosis and Vascular Biology, and the ESC Council of Basic Cardiovascular Science. *Cardiovascular Research* **116,** 2177–2184. ISSN: 0008-6363 (Dec. 1, 2020).

25. Mesquita, R. C. & Yodh, A. G. Diffuse optics: fundamentals and tissue applications. *Nano optics and atomics: transport of light and matter waves* **173.** <http://ebooks.iospress.nl/volumearticle/26855> (visited on 10/13/2016) (2011).

26. Mesquita, R. C. *et al.* Hemodynamic and metabolic diffuse optical monitoring in a mouse model of hindlimb ischemia. *Biomedical Optics Express* **1,** 1173–1187. ISSN: 2156-7085 (Oct. 15, 2010).

27. Ferrari, M. Progress of near-infrared spectroscopy and topography for brain and muscle clinical applications. *Journal of Biomedical Optics* **12,** 062104. ISSN: 1083-3668 (Nov. 1, 2007).

28. Yodh, A. & Chance, B. Spectroscopy and imaging with diffusing light. *Physics Today* **48,** 34–41 (1995).

29. Matcher, S. J., Cope, M. & Delpy, D. T. Use of the water absorption spectrum to quantify tissue chromophore concentration changes in near-infrared spectroscopy. *Physics in Medicine and Biology* **39,** 177–196. ISSN: 0031-9155, 1361-6560 (Jan. 1, 1994).

30. Pogue, B. W. & Patterson, M. S. Frequency-domain optical absorption spectroscopy of finite tissue volumes using diffusion theory. *Physics in Medicine and Biology* **39,** 1157–1180. ISSN: 0031-9155, 1361-6560 (July 1, 1994).

31. Fantini, S. Frequency-domain multichannel optical detector for noninvasive tissue spectroscopy and oximetry. *Optical Engineering* **34,** 32. ISSN: 0091-3286 (Jan. 1, 1995).

32. Durduran, T., Yodh, A. G., Chance, B. & Boas, D. A. Does the photon-diffusion coefficient depend on absorption? *Journal of the Optical Society of America A* **14,** 3358. ISSN: 1084-7529, 1520-8532 (Dec. 1, 1997).

33. Quiroga Soto, A. F. & Mesquita, R. C. *Espectroscopia óptica de difusão multiespectral para aplicações biomédicas* Dissertação de Mestrado (Aug. 7, 2016). <`http://www.bibliotecadigital.unicamp.br/document/?code=000972248&opt=4`> (visited on 10/13/2016).

34. Mesquita, R. C. *et al.* Direct measurement of tissue blood flow and metabolism with diffuse optics. *Philosophical Transactions of the Royal Society of London A: Mathematical, Physical and Engineering Sciences* **369,** 4390–4406. ISSN: 1364-503X, 1471-2962 (Nov. 28, 2011).

35. Scheeren, T. W. L., Schober, P. & Schwarte, L. A. Monitoring tissue oxygenation by near infrared spectroscopy (NIRS): background and current applications. *Journal of Clinical Monitoring and Computing* **26,** 279–287. ISSN: 1387-1307 (Aug. 2012).

36. Choe, R. *et al.* Optically Measured Microvascular Blood Flow Contrast of Malignant Breast Tumors. *PLoS ONE* **9** (ed Najbauer, J.) e99683. ISSN: 1932-6203 (June 26, 2014).

37. Chung, S. H. *et al.* Macroscopic optical physiological parameters correlate with microscopic proliferation and vessel area breast cancer signatures. *Breast Cancer Research* **17,** 72. ISSN: 1465-542X (May 27, 2015).

38. Favilla Christopher G. *et al.* Optical Bedside Monitoring of Cerebral Blood Flow in Acute Ischemic Stroke Patients During Head-of-Bed Manipulation. *Stroke* **45.** Publisher: American Heart Association, 1269–1274 (May 1, 2014).

39. Ferrari, M. & Quaresima, V. A brief review on the history of human functional near-infrared spectroscopy (fNIRS) development and fields of application. *NeuroImage* **63,** 921–935. ISSN: 10538119 (Nov. 2012).

40. Forero, E. J. *et al.* Use of near-infrared spectroscopy to probe occlusion severity in patients diagnosed with carotid atherosclerotic disease. *Medical Research Archives* **5.** ISSN: 2375-1924. <http://www.journals.ke-i.org/index.php/mra/article/view/1240> (visited on 03/15/2018) (June 15, 2017).

41. Forti, R. M. *et al.* Real-Time Monitoring of Neurocritical Patients with Diffuse Optical Spectroscopies. *JoVE (Journal of Visualized Experiments),* e61608. ISSN: 1940-087X (Nov. 19, 2020).

42. Kim, M. N. *et al.* Continuous Optical Monitoring of Cerebral Hemodynamics During Head-of-Bed Manipulation in Brain-Injured Adults. *Neurocritical Care* **20,** 443–453. ISSN: 1541-6933, 1556-0961 (May 8, 2013).

43. Buckley, E. M. *et al.* Cerebral hemodynamics in preterm infants during positional intervention measured with diffuse correlation spectroscopy and transcranial Doppler ultrasound. *Optics Express* **17.** Publisher: Optical Society of America, 12571–12581. ISSN: 1094-4087 (July 20, 2009).

44. Grant, P. E. *et al.* Increased Cerebral Blood Volume and Oxygen Consumption in Neonatal Brain Injury. *Journal of Cerebral Blood Flow & Metabolism* **29.** Publisher: SAGE Publications Ltd STM, 1704–1713. ISSN: 0271-678X (Oct. 1, 2009).

45. Mesquita, R. C. & Covolan, R. J. Estudo Funcional do Cérebro através de NIRS e Tomografia Óptica de Difusão. *Neurociências e Epilepsia,* 147 (2008).

46. Rodriguez, R. C. & Mesquita, R. C. *Utilização da fase para estimativa das propriedades ópticas absolutas do tecido biológico com espectroscopia óptica de difusão* Dissertação de Mestrado (Oct. 11, 2014). <`http://www.bibliotecadigital.unicamp.br/document/?code=000936315&opt=4`> (visited on 10/13/2016).

47. Forti, R. M. & Mesquita, R. C. *Determination of the dynamical properties in turbid media using diffuse correlation spectroscopy : applications to biological tissue* Dissertação de Mestrado (June 4, 2015). <`http://www.bibliotecadigital.unicamp.br/document/?code=000947656&opt=4`> (visited on 10/13/2016).

48. Bouguer, P. *Essai d'optique sur la gradation de la lumière* Google-Books-ID: JNkTAAAAQAAJ. 198 pp. (Jombert, 1729).

49. Lambert, J. H. *Photometria sive de mensura et gradibus luminis, colorum et umbrae* Google-Books-ID: JdkTAAAAQAAJ. 586 pp. (sumptibus vidvae E. Klett, typis C.P. Detleffsen, 1760).

50. Beer. Bestimmung der Absorption des rothen Lichts in farbigen Flüssigkeiten. *Annalen der Physik* **162.** _eprint: https://onlinelibrary.wiley.com/doi/pdf/10.1002/andp.18521620505, 78–88. ISSN: 1521-3889 (1852).

51. Durduran, T., Choe, R., Baker, W. B. & Yodh, A. G. Diffuse optics for tissue monitoring and tomography. *Reports on Progress in Physics* **73,** 076701. ISSN: 0034-4885 (June 2010).

52. Vo-Dinh, T. *Biomedical Photonics Handbook* <`https://spie.org/Publications/Book/511786`> (visited on 02/15/2022) ().

53. Balcerek, B. *et al.* A broad diversity in oxygen affinity to haemoglobin. *Scientific Reports* **10.** Bandiera_abtest: a Cc_license_type: cc_by Cg_type: Nature Research Journals Number: 1 Primary_atype: Research Publisher: Nature Publishing Group Subject_term: Medical research;Physiology Subject_term_id: medical-research;physiology, 16920. ISSN: 2045-2322 (Oct. 9, 2020).

54. Sandell, J. L. & Zhu, T. C. A review of in-vivo optical properties of human tissues and its impact on PDT. *Journal of Biophotonics* **4,** 773–787. ISSN: 1864063X (Nov. 2011).

55. Jacques, S. L. Optical properties of biological tissues: a review. *Physics in Medicine and Biology* **58,** R37–R61. ISSN: 0031-9155, 1361-6560 (June 7, 2013).

56. Pogue, B. W. *et al.* Characterization of hemoglobin, water, and NIR scattering in breast tissue: analysis of intersubject variability and menstrual cycle changes. *Journal of Biomedical Optics* **9,** 541. ISSN: 10833668 (2004).

57. Henyey, L. G. & Greenstein, J. L. Diffuse radiation in the Galaxy. *The Astrophysical Journal* **93,** 70–83. ISSN: 0004-637X (Jan. 1, 1941).

58. Cornette, W. M. & Shanks, J. G. Physically reasonable analytic expression for the single-scattering phase function. *Applied Optics* **31.** Publisher: Optical Society of America, 3152–3160. ISSN: 2155-3165 (June 1, 1992).

59. Mourant, J. R. *et al.* Light scattering from cells: the contribution of the nucleus and the effects of proliferative status. *Journal of Biomedical Optics* **5.** Publisher: SPIE, 131–137. ISSN: 1083-3668, 1560-2281 (Apr. 2000).

60. Cope, M. *The application of near infrared spectroscopy to non invasive monitoring of cerebral oxygenation in the newborn infant* PhD thesis (University College London, 1991). 342 pp.

61. Kienle, A. *et al.* Spatially resolved absolute diffuse reflectance measurements for noninvasive determination of the optical scattering and absorption coefficients of biological tissue. *Applied Optics* **35,** 2304–2314. ISSN: 2155-3165 (May 1, 1996).

62. Bhatt, M., Ayyalasomayajula, K. R. & Yalavarthy, P. K. Generalized Beer–Lambert model for near-infrared light propagation in thick biological tissues. *Journal of Biomedical Optics* **21.** Publisher: International Society for Optics and Photonics, 076012. ISSN: 1083-3668, 1560-2281 (July 2016).

63. Arridge, S. R., Cope, M. & Delpy, D. T. The theoretical basis for the determination of optical pathlengths in tissue: temporal and frequency analysis. *Physics in Medicine and Biology* **37,** 1531–1560. ISSN: 0031-9155, 1361-6560 (July 1, 1992).

64. Hiraoka, M. *et al.* A Monte Carlo investigation of optical pathlength in inhomogeneous tissue and its application to near-infrared spectroscopy. *Physics in Medicine and Biology* **38.** Publisher: IOP Publishing, 1859–1876. ISSN: 0031-9155 (Dec. 1993).

65. Baker, W. B. *et al.* Modified Beer-Lambert law for blood flow. *Biomedical Optics Express* **5.** Publisher: Optical Society of America, 4053–4075. ISSN: 2156-7085 (Nov. 1, 2014).

66. Baker, W. Optical Cerebral Blood Flow Monitoring of Mice to Men. *Publicly Accessible Penn Dissertations.* <`https://repository.upenn.edu/edissertations/1010`> (Jan. 1, 2015).

67. Mourant, J. R., Bigio, I. J., Jack, D. A., Johnson, T. M. & Miller, H. D. Measuring absorption coefficients in small volumes of highly scattering media: source-detector separations for which path lengths do not depend on scattering properties. *Applied Optics* **36,** 5655. ISSN: 0003-6935, 1539-4522 (Aug. 1, 1997).

68. Scholkmann, F. & Wolf, M. General equation for the differential pathlength factor of the frontal human head depending on wavelength and age. *Journal of Biomedical Optics* **18.** Publisher: International Society for Optics and Photonics, 105004. ISSN: 1083-3668, 1560-2281 (Oct. 2013).

69. Delpy, D. T. *et al.* Estimation of optical pathlength through tissue from direct time of flight measurement. *Physics in Medicine and Biology* **33.** Publisher: IOP Publishing, 1433–1442. ISSN: 0031-9155 (Dec. 1988).

70. Zhao, H. *et al.* Maps of optical differential pathlength factor of human adult forehead, somatosensory motor and occipital regions at multi-wavelengths in NIR. *Physics in Medicine and Biology* **47.** Publisher: IOP Publishing, 2075–2093. ISSN: 0031-9155 (June 2002).

71. Duncan, A. *et al.* Optical pathlength measurements on adult head, calf and forearm and the head of the newborn infant using phase resolved optical spectroscopy. *Physics in Medicine and Biology* **40.** Publisher: IOP Publishing, 295–304. ISSN: 0031-9155 (Feb. 1995).

72. Matcher, S. J., Elwell, C. E., Cooper, C. E., Cope, M. & Delpy, D. T. Performance Comparison of Several Published Tissue Near-Infrared Spectroscopy Algorithms. *Analytical Biochemistry* **227,** 54–68. ISSN: 0003-2697 (May 1, 1995).

73. Patterson, M. S., Schwartz, E. & Wilson, B. C. *Quantitative Reflectance Spectrophotometry For The Noninvasive Measurement Of Photosensitizer Concentration In Tissue During Photodynamic Therapy* in *Photodynamic Therapy: Mechanisms* Photodynamic Therapy: Mechanisms. **1065** (SPIE, June 13, 1989), 115–122. doi:10/gnzc3z. <https://www.spiedigitallibrary.org/conference-proceedings-of-spie/1065/0000/Quantitative-Reflectance-Spectrophotometry-For-The-Noninvasive-Measurement-Of-Photosensitizer-Concentration/10.1117/12.978011.full> (visited on 01/04/2022).

74. Suzuki, S., Takasaki, S., Ozaki, T. & Kobayashi, Y. *Tissue oxygenation monitor using NIR spatially resolved spectroscopy* in. Proceedings of SPIE - The International Society for Optical Engineering. **3597.** ISSN: 0277-786X (1999), 582–592.

75. Matcher, S. J., Cope, M. & Delpy, D. T. In vivo measurements of the wavelength dependence of tissue-scattering coefficients between 760 and 900 nm measured with time-resolved spectroscopy. *Applied Optics* **36.** Publisher: Optical Society of America, 386–396. ISSN: 2155-3165 (Jan. 1, 1997).

76. Mescher, A. *Junqueira's Basic Histology: Text and Atlas, Thirteenth Edition: Text and Atlas, Thirteenth Edition* 559 pp. ISBN: 978-0-07-180720-3 (McGraw Hill Professional, Feb. 22, 2013).

77. Sakadžić, S. *et al.* Large arteriolar component of oxygen delivery implies a safe margin of oxygen supply to cerebral tissue. *Nature Communications* **5.** Bandiera_abtest: a Cg_type: Nature Research Journals Number: 1 Primary_atype: Research Publisher: Nature Publishing Group Subject_term: Medical research;Metabolism;Neurophysiology Subject_term_id: medical-research;metabolism;neurophysiology, 5734. ISSN: 2041-1723 (Dec. 8, 2014).

78. Leow, M. K.-S. Configuration of the hemoglobin oxygen dissociation curve demystified: a basic mathematical proof for medical and biological sciences undergraduates. *Advances in*

Physiology Education **31.** Publisher: American Physiological Society, 198–201. ISSN: 1043-4046 (June 1, 2007).

79. Boas, D. A., Jones, S. R., Devor, A., Huppert, T. J. & Dale, A. A vascular anatomical network model of the spatio-temporal response to brain activation. *NeuroImage* **40,** 1116–1129. ISSN: 1053-8119 (Apr. 15, 2008).

80. Wolf, M. *et al.* Different Time Evolution of Oxyhemoglobin and Deoxyhemoglobin Concentration Changes in the Visual and Motor Cortices during Functional Stimulation: A Near-Infrared Spectroscopy Study. *NeuroImage* **16,** 704–712. ISSN: 1053-8119 (July 1, 2002).

81. Boas, D. A., Dale, A. M. & Franceschini, M. A. Diffuse optical imaging of brain activation: approaches to optimizing image sensitivity, resolution, and accuracy. *NeuroImage. Mathematics in Brain Imaging* **23,** S275–S288. ISSN: 1053-8119 (Jan. 1, 2004).

82. Boas, D. A. & Franceschini, M. A. Haemoglobin oxygen saturation as a biomarker: the problem and a solution. *Philosophical transactions. Series A, Mathematical, physical, and engineering sciences* **369,** 4407–4424. ISSN: 1364-503X (Nov. 28, 2011).

83. Scholkmann, F. *et al.* A review on continuous wave functional near-infrared spectroscopy and imaging instrumentation and methodology. *NeuroImage. Celebrating 20 Years of Functional Near Infrared Spectroscopy (fNIRS)* **85,** 6–27. ISSN: 1053-8119 (Jan. 15, 2014).

84. Strangman, G., Franceschini, M. A. & Boas, D. A. Factors affecting the accuracy of near-infrared spectroscopy concentration calculations for focal changes in oxygenation parameters. *NeuroImage* **18,** 865–879. ISSN: 1053-8119 (Apr. 1, 2003).

85. Uludağ, K., Steinbrink, J., Villringer, A. & Obrig, H. Separability and cross talk: optimizing dual wavelength combinations for near-infrared spectroscopy of the adult head. *NeuroImage* **22,** 583–589. ISSN: 1053-8119 (June 1, 2004).

86. Correia, T. M., Gibson, A. P. & Hebden, J. C. Identification of the optimal wavelengths for optical topography: a photon measurement density function analysis. *Journal of Biomedical Optics* **15.** Publisher: International Society for Optics and Photonics, 056002. ISSN: 1083-3668, 1560-2281 (Sept. 2010).

87. Okui, N. & Okada, E. Wavelength dependence of crosstalk in dual-wavelength measurement of oxy- and deoxy-hemoglobin. *Journal of Biomedical Optics* **10.** Publisher: International Society for Optics and Photonics, 011015. ISSN: 1083-3668, 1560-2281 (Jan. 2005).

88. Sato, H., Kiguchi, M., Kawaguchi, F. & Maki, A. Practicality of wavelength selection to improve signal-to-noise ratio in near-infrared spectroscopy. *NeuroImage* **21,** 1554–1562. ISSN: 1053-8119 (Apr. 1, 2004).

89. Yamashita, Y., Maki, A. & Koizumi, H. Wavelength dependence of the precision of non-invasive optical measurement of oxy-, deoxy-, and total-hemoglobin concentration. *Medical Physics* **28.** _eprint: https://aapm.onlinelibrary.wiley.com/doi/pdf/10.1118/1.1373401, 1108–1114. ISSN: 2473-4209 (2001).

90. Maira, G., Mazzillo, M., Libertino, S., Fallica, G. & Lombardo, S. Crucial aspects for the use of silicon photomultiplier devices in continuous wave functional near-infrared spectroscopy. *Biomedical Optics Express* **9,** 4679–4688. ISSN: 2156-7085 (Sept. 7, 2018).

91. Sanfilippo, D. *et al. Design and development of a fNIRS system prototype based on SiPM detectors* in *Silicon Photonics IX* Silicon Photonics IX. **8990** (SPIE, Mar. 8, 2014), 256–265. doi:10/gm2xs5. <https://www.spiedigitallibrary.org/conference-proceedings-of-spie/8990/899016/Design-and-development-of-a-fNIRS-system-prototype-based-on/10.1117/12.2037559.full> (visited on 10/08/2021).

92. Adamo, G. *et al.* Silicon Photomultipliers Signal-to-Noise Ratio in the Continuous Wave Regime. *IEEE Journal of Selected Topics in Quantum Electronics* **20.** Conference Name: IEEE Journal of Selected Topics in Quantum Electronics, 284–290. ISSN: 1558-4542 (Nov. 2014).

93. Okada, E. & Delpy, D. T. Near-infrared light propagation in an adult head model. II. Effect of superficial tissue thickness on the sensitivity of the near-infrared spectroscopy signal. *Applied Optics* **42.** Publisher: Optical Society of America, 2915–2921. ISSN: 2155-3165 (June 1, 2003).

94. Brigadoi, S., Salvagnin, D., Fischetti, M. & Cooper, R. J. Array Designer: automated optimized array design for functional near-infrared spectroscopy. *Neurophotonics* **5.** Publisher: SPIE, 035010. ISSN: 2329-423X, 2329-4248 (Sept. 2018).

95. Machado, A. *et al.* Optimal positioning of optodes on the scalp for personalized functional near-infrared spectroscopy investigations. *Journal of Neuroscience Methods* **309,** 91–108. ISSN: 0165-0270 (Nov. 1, 2018).

96. Vidal-Rosas, E. E. *et al.* Evaluating a new generation of wearable high-density diffuse optical tomography technology via retinotopic mapping of the adult visual cortex. *Neurophotonics* **8.** Publisher: SPIE, 025002. ISSN: 2329-423X, 2329-4248 (Apr. 2021).

97. Zimeo Morais, G. A., Balardin, J. B. & Sato, J. R. fNIRS Optodes' Location Decider (fOLD): a toolbox for probe arrangement guided by brain regions-of-interest. *Scientific Reports* **8.** Bandiera_abtest: a Cc_license_type: cc_by Cg_type: Nature Research Journals Number: 1 Primary_atype: Research Publisher: Nature Publishing Group Subject_term: Cognitive neuroscience;Imaging and sensing Subject_term_id: cognitive-neuroscience;imaging-and-sensing, 3341. ISSN: 2045-2322 (Feb. 20, 2018).

98. Franceschini, M. A., Fantini, S., Thompson, J. H., Culver, J. P. & Boas, D. A. Hemodynamic evoked response of the sensorimotor cortex measured noninvasively with near-infrared optical imaging. *Psychophysiology* **40,** 548–560. ISSN: 0048-5772 (July 2003).

99. Ferrari, M. A Mini-Review on Functional Near-Infrared Spectroscopy (fNIRS): Where Do We Stand, and Where Should We Go? *Photonics* **6.** Place: Basel, Switzerland Publisher: MDPI AG. doi:10/gh5997. <https://www.proquest.com/docview/2550222096/abstract/314F66B45D184B0DPQ/1> (visited on 10/11/2021) (2019).

100. Hirth, C., Obrig, H., Valdueza, J., Dirnagl, U. & Villringer, A. in *Oxygen Transport to Tissue XVIII* (eds Nemoto, E. M. *et al.*) 461–469 (Springer US, Boston, MA, 1997). ISBN: 978-1-4615-5865-1. doi:10.1007/978-1-4615-5865-1_59. <https://doi.org/10.1007/978-1-4615-5865-1_59> (visited on 11/03/2021).

101. Huppert, T. J., Hoge, R. D., Diamond, S. G., Franceschini, M. A. & Boas, D. A. A temporal comparison of BOLD, ASL, and NIRS hemodynamic responses to motor stimuli in adult humans. *NeuroImage* **29,** 368–382. ISSN: 1053-8119 (Jan. 15, 2006).

102. Leff, D. R. *et al.* Diffuse optical imaging of the healthy and diseased breast: A systematic review. *Breast Cancer Research and Treatment* **108,** 9–22. ISSN: 0167-6806, 1573-7217 (Mar. 2008).

103. Khan, M. N. A., Bhutta, M. R. & Hong, K.-S. Task-Specific Stimulation Duration for fNIRS Brain-Computer Interface. *IEEE Access* **8.** Conference Name: IEEE Access, 89093–89105. ISSN: 2169-3536 (2020).

104. Tian, F., Chance, B. & Liu, H. Investigation of the prefrontal cortex in response to duration-variable anagram tasks using functional near-infrared spectroscopy. *Journal of Biomedical Optics* **14.** Publisher: SPIE, 054016. ISSN: 1083-3668, 1560-2281 (Sept. 2009).

105. Kirilina, E. *et al.* Identifying and quantifying main components of physiological noise in functional near infrared spectroscopy on the prefrontal cortex. *Frontiers in Human Neuroscience* **7,** 864. ISSN: 1662-5161 (2013).

106. Julien, C. The enigma of Mayer waves: Facts and models. *Cardiovascular Research* **70,** 12–21. ISSN: 0008-6363 (Apr. 1, 2006).

107. Mayer, S. *Studien zur Physiologie des Herzens und der Blutgefässe: uber spontane Blutdruckschwankungen* ZSCC: NoCitationData[s0]. <`https://books.google.com.br/books?id=n4_iZwEACAAJ`> (1876).

108. Yücel, M. A. *et al.* Mayer waves reduce the accuracy of estimated hemodynamic response functions in functional near-infrared spectroscopy. *Biomedical Optics Express* **7,** 3078–3088. ISSN: 2156-7085 (July 22, 2016).

109. Tong, Y. & Frederick, B. d. Time lag dependent multimodal processing of concurrent fMRI and near-infrared spectroscopy (NIRS) data suggests a global circulatory origin for low-frequency oscillation signals in human brain. *NeuroImage* **53,** 553–564. ISSN: 1053-8119 (Nov. 1, 2010).

110. Nafz, B., Wagner, C. D. & Persson, P. B. Endogenous nitric oxide buffers blood pressure variability between 0.2 and 0.6 Hz in the conscious rat. *American Journal of Physiology-Heart and Circulatory Physiology* **272.** Publisher: American Physiological Society, H632–H637. ISSN: 0363-6135 (Feb. 1, 1997).

111. Novi, S. L. *et al.* Functional near-infrared spectroscopy for speech protocols: characterization of motion artifacts and guidelines for improving data analysis. *Neurophotonics* **7.** Publisher: SPIE, 015001. ISSN: 2329-423X, 2329-4248 (Jan. 2020).

112. Pinti, P., Scholkmann, F., Hamilton, A., Burgess, P. & Tachtsidis, I. Current Status and Issues Regarding Pre-processing of fNIRS Neuroimaging Data: An Investigation of Diverse Signal Filtering Methods Within a General Linear Model Framework. *Frontiers in Human Neuroscience* **12.** Publisher: Frontiers. ISSN: 1662-5161. doi:10/fkw7. <https://www.frontiersin.org/articles/10.3389/fnhum.2018.00505/full> (visited on 07/08/2021) (2019).

113. Klein, F. & Kranczioch, C. Signal Processing in fNIRS: A Case for the Removal of Systemic Activity for Single Trial Data. *Frontiers in Human Neuroscience* **13,** 331. ISSN: 1662-5161 (2019).

114. Huppert, T. J., Diamond, S. G., Franceschini, M. A. & Boas, D. A. HomER: a review of time-series analysis methods for near-infrared spectroscopy of the brain. *Applied optics* **48,** D280–D298. ISSN: 0003-6935 (Apr. 1, 2009).

115. Virtanen, J., Noponen, T. E. J. & Meriläinen, P. Comparison of principal and independent component analysis in removing extracerebral interference from near-infrared spectroscopy signals. *Journal of Biomedical Optics* **14.** Publisher: SPIE, 054032. ISSN: 1083-3668, 1560-2281 (Sept. 2009).

116. Zhang, X., Noah, J. A. & Hirsch, J. Separation of the global and local components in functional near-infrared spectroscopy signals using principal component spatial filtering. *Neurophotonics* **3.** Publisher: SPIE, 015004. ISSN: 2329-423X, 2329-4248 (Feb. 2016).

117. Zhang, Y., Brooks, D. H., Franceschini, M. A. & Boas, D. A. Eigenvector-based spatial filtering for reduction of physiological interference in diffuse optical imaging. *Journal of Biomedical Optics* **10.** Publisher: SPIE, 011014. ISSN: 1083-3668, 1560-2281 (Jan. 2005).

118. Wyser, D. *et al.* Short-channel regression in functional near-infrared spectroscopy is more effective when considering heterogeneous scalp hemodynamics. *Neurophotonics* **7,** 035011. ISSN: 2329-423X (July 2020).

119. Takahashi, T. *et al.* Influence of skin blood flow on near-infrared spectroscopy signals measured on the forehead during a verbal fluency task. *NeuroImage* **57,** 991–1002. ISSN: 1095-9572 (Aug. 1, 2011).

120. Gagnon, L. *et al.* Short separation channel location impacts the performance of short channel regression in NIRS. *NeuroImage* **59,** 2518–2528. ISSN: 1095-9572 (Feb. 1, 2012).

121. Sato, T. *et al.* Reduction of global interference of scalp-hemodynamics in functional near-infrared spectroscopy using short distance probes. *NeuroImage* **141,** 120–132. ISSN: 1095-9572 (Nov. 1, 2016).

122. Nguyen, H.-D., Yoo, S.-H., Bhutta, M. R. & Hong, K.-S. Adaptive filtering of physiological noises in fNIRS data. *Biomedical Engineering Online* **17,** 180. ISSN: 1475-925X (Dec. 4, 2018).

123. Dong, S. & Jeong, J. Improvement in Recovery of Hemodynamic Responses by Extended Kalman Filter With Non-Linear State-Space Model and Short Separation Measurement. *IEEE transactions on bio-medical engineering* **66,** 2152–2162. ISSN: 1558-2531 (Aug. 2019).

124. Noah, J. A. *et al.* Comparison of short-channel separation and spatial domain filtering for removal of non-neural components in functional near-infrared spectroscopy signals. *Neurophotonics* **8.** Publisher: SPIE, 015004. ISSN: 2329-423X, 2329-4248 (Feb. 2021).

125. Zhang, F. *et al.* Correcting physiological noise in whole-head functional near-infrared spectroscopy. *Journal of Neuroscience Methods* **360,** 109262. ISSN: 0165-0270 (Aug. 1, 2021).

126. Zhou, X., Sobczak, G., McKay, C. M. & Litovsky, R. Y. Comparing fNIRS signal qualities between approaches with and without short channels. *PloS One* **15,** e0244186. ISSN: 1932-6203 (2020).

127. Friston, K. J. *et al.* Statistical parametric maps in functional imaging: A general linear approach. *Human Brain Mapping* **2.** _eprint: https://onlinelibrary.wiley.com/doi/pdf/10.1002/hbm.46002 189–210. ISSN: 1097-0193 (1994).

128. Abdelnour, A. F. & Huppert, T. Real-time imaging of human brain function by near-infrared spectroscopy using an adaptive general linear model. *NeuroImage* **46,** 133–143. ISSN: 1053-8119 (May 15, 2009).

129. Cannestra, A. F., Pouratian, N., Shomer, M. H. & Toga, A. W. Refractory Periods Observed by Intrinsic Signal and Fluorescent Dye Imaging. *Journal of Neurophysiology* **80.** Publisher: American Physiological Society, 1522–1532. ISSN: 0022-3077 (Sept. 1, 1998).

130. Von Lühmann, A., Ortega-Martinez, A., Boas, D. A. & Yücel, M. A. Using the General Linear Model to Improve Performance in fNIRS Single Trial Analysis and Classification: A Perspective. *Frontiers in Human Neuroscience* **14,** 30. ISSN: 1662-5161 (2020).

131. Pinti, P. *et al.* A novel GLM-based method for the Automatic IDentification of functional Events (AIDE) in fNIRS data recorded in naturalistic environments. *Neuroimage* **155,** 291–304. ISSN: 1053-8119 (July 15, 2017).

132. Santosa, H., Fishburn, F., Zhai, X. & Huppert, T. J. Investigation of the sensitivity-specificity of canonical- and deconvolution-based linear models in evoked functional near-infrared spectroscopy. *Neurophotonics* **6.** Publisher: SPIE, 025009. ISSN: 2329-423X, 2329-4248 (May 2019).

133. Huppert, T. J. Commentary on the statistical properties of noise and its implication on general linear models in functional near-infrared spectroscopy. *Neurophotonics* **3,** 010401. ISSN: 2329-423X (Jan. 2016).

134. Song, P. *et al.* Global and regional prevalence, burden, and risk factors for carotid atherosclerosis: a systematic review, meta-analysis, and modelling study. *The Lancet Global Health* **8.** Publisher: Elsevier, e721–e729. ISSN: 2214-109X (May 1, 2020).

135. Parish, S. *et al.* Assessment of the Role of Carotid Atherosclerosis in the Association Between Major Cardiovascular Risk Factors and Ischemic Stroke Subtypes. *JAMA Network Open* **2,** e194873. ISSN: 2574-3805 (May 31, 2019).

136. Virani, S. S. *et al.* Heart Disease and Stroke Statistics—2021 Update. *Circulation* **143.** Publisher: American Heart Association, e254–e743 (Feb. 23, 2021).

137. De Santana, N. M. *et al.* The burden of stroke in Brazil in 2016: an analysis of the Global Burden of Disease study findings. *BMC Research Notes* **11,** 735. ISSN: 1756-0500 (Oct. 16, 2018).

138. Null null, n. *et al.* Executive Summary: Heart Disease and Stroke Statistics—2010 Update. *Circulation* **121.** Publisher: American Heart Association, 948–954 (Feb. 23, 2010).

139. Porcu, M. *et al.* Carotid plaque imaging profiling in subjects with risk factors (diabetes and hypertension). *Cardiovascular Diagnosis and Therapy* **10,** 1005–1018. ISSN: 2223-3652 (Aug. 2020).

140. Vos, T. *et al.* Global, regional, and national incidence, prevalence, and years lived with disability for 310 diseases and injuries, 1990–2015: a systematic analysis for the Global Burden of Disease Study 2015. *The Lancet* **388.** Publisher: Elsevier, 1545–1602. ISSN: 0140-6736, 1474-547X (Oct. 8, 2016).

141. Gupta, A., Baradaran, H. & Schweitzer, A. D. Carotid Plaque MRI and Stroke Risk: A Systematic Review and Meta-analysis. *Journal of Vascular Surgery* **59.** Publisher: Elsevier, 1175. ISSN: 0741-5214, 1097-6809 (Apr. 1, 2014).

142. Petty, G. W. *et al.* Ischemic Stroke Subtypes. *Stroke* **30.** Publisher: American Heart Association, 2513–2516 (Dec. 1, 1999).

143. Buratti, L. *et al.* Thresholds of impaired cerebral hemodynamics that predict short-term cognitive decline in asymptomatic carotid stenosis. *Journal of Cerebral Blood Flow & Metabolism* **36,** 1804–1812. ISSN: 0271-678X (Oct. 2016).

144. Shakur, S. F. *et al.* Effects of Extracranial Carotid Stenosis on Intracranial Blood Flow. *Stroke* **45.** Publisher: American Heart Association, 3427–3429 (Nov. 1, 2014).

145. Stary, H. C. Natural History and Histological Classification of Atherosclerotic Lesions: An Update. *Arteriosclerosis, Thrombosis, and Vascular Biology* **20,** 1177–1178. ISSN: 1079-5642, 1524-4636 (May 1, 2000).

146. Libby, P. Inflammation in atherosclerosis. *Nature* **420.** Bandiera_abtest: a Cg_type: Nature Research Journals Number: 6917 Primary_atype: Reviews Publisher: Nature Publishing Group, 868–874. ISSN: 1476-4687 (Dec. 2002).

147. Mughal, M. M. *et al.* Symptomatic and asymptomatic carotid artery plaque. **9,** 1315–1330 (2011).

148. Avelar, W. M. *et al.* Asymptomatic Carotid Stenosis is Associated with Gray and White Matter Damage. *International Journal of Stroke* **10.** Publisher: SAGE Publications, 1197–1203. ISSN: 1747-4930 (Dec. 1, 2015).

149. Guillaumon, A. T. *et al.* Endarterectomia carotídea sob bloqueio loco-regional. *Jornal Vascular Brasileiro* **4,** 249–254. ISSN: 1677-5449 (Sept. 2005).

150. Aktuerk, D., Mishra, P. K., Luckraz, H., Garnham, A. & Khazi, F. M. Cerebral oxygenation monitoring in patients with bilateral carotid stenosis undergoing urgent cardiac surgery: Observational case series. *Annals of Cardiac Anaesthesia* **19,** 59–62. ISSN: 0971-9784 (2016).

151. Zogogiannis, I. D. *et al.* Evaluation of an intraoperative algorithm based on near-infrared refracted spectroscopy monitoring, in the intraoperative decision for shunt placement, in patients undergoing carotid endarterectomy. *Middle East Journal of Anaesthesiology* **21,** 367–373. ISSN: 0544-0440 (Oct. 2011).

152. Kakumoto, K., Harada, K., Sankoda, Y., Taniguchi, S. & Fukuyama, K. Near-infrared spectroscopy cerebral oximetry as a predictor of neurological intolerance during carotid artery stenting with proximal protection. *Journal of Clinical Neuroscience* **58,** 89–93. ISSN: 0967-5868 (Dec. 1, 2018).

153. Manwaring, M. L. *et al.* Correlation of Cerebral Oximetry With Internal Carotid Artery Stump Pressures in Carotid Endarterectomy. *Vascular and Endovascular Surgery* **44.** Publisher: SAGE Publications Inc, 252–256. ISSN: 1538-5744 (May 1, 2010).

154. Ceyhan, D. & Ovali, C. The Effect of Cerebral Oximeter Use on the Shunt Placement Concerning Carotid Endarterectomy Surgery. *Annals of Cardiac Anaesthesia* **22,** 158–161. ISSN: 0971-9784 (2019).

155. Ali, A. M. *et al.* Cerebral monitoring in patients undergoing carotid endarterectomy using a triple assessment technique. *Interactive CardioVascular and Thoracic Surgery* **12,** 454–457. ISSN: 1569-9293 (Mar. 1, 2011).

156. Park, H. S. *et al.* Amplitude of Tissue Oxygenation Index Change Predicts Cerebral Hyperperfusion Syndrome During Carotid Artery Stenting. *World Neurosurgery* **99,** 548–555. ISSN: 1878-8750 (Mar. 1, 2017).

157. Jonsson, M., Lindström, D., Wanhainen, A., Gidlund, K. D. & Gillgren, P. Near Infrared Spectroscopy as a Predictor for Shunt Requirement During Carotid Endarterectomy. *European Journal of Vascular and Endovascular Surgery* **53.** Publisher: Elsevier, 783–791. ISSN: 1078-5884, 1532-2165 (June 1, 2017).

158. Pennekamp, C. W. A. *et al.* Near-infrared Spectroscopy to Indicate Selective Shunt Use During Carotid Endarterectomy. *European Journal of Vascular and Endovascular Surgery* **46,** 397–403. ISSN: 1078-5884 (Oct. 1, 2013).

159. Kondov, S. *et al.* Outcome of Near-Infrared Spectroscopy–Guided Selective Shunting During Carotid Endarterectomy in General Anesthesia. *Annals of Vascular Surgery* **61,** 170–177. ISSN: 0890-5096 (Nov. 1, 2019).

160. Pedrini, L. *et al.* Is Near-Infrared Spectroscopy a Reliable Method to Evaluate Clamping Ischemia during Carotid Surgery? *Stroke Research and Treatment* **2012,** 156975. ISSN: 2090-8105 (2012).

161. Herrera Campos, C. R., Beltramini, G. C., Avelar, W. M., Lima, F. O. & Li, L. M. Cerebral vasomotor reactivity assessment using Transcranial Doppler and MRI with apnea test. *Brazilian Journal of Medical and Biological Research* **49.** Publisher: Associação Brasileira de Divulgação Científica. ISSN: 0100-879X, 1414-431X. doi:10/f88nvj. <http://www.scielo.br/j/bjmbr/a/QjYNzV3LkyRFSLBgWhhPTCp/?lang=en> (visited on 01/22/2022) (Oct. 24, 2016).

162. Reinhard, M. *et al.* Cerebral Autoregulation in Carotid Artery Occlusive Disease Assessed From Spontaneous Blood Pressure Fluctuations by the Correlation Coefficient Index. *Stroke* **34,** 2138–2144 (Sept. 1, 2003).

163. Vernieri, F. *et al.* Transcranial Doppler and Near-Infrared Spectroscopy Can Evaluate the Hemodynamic Effect of Carotid Artery Occlusion. *Stroke* **35.** Publisher: American Heart Association, 64–70 (Jan. 1, 2004).

164. Lee, J. K. *et al.* Cerebrovascular Reactivity Measured by Near-Infrared Spectroscopy. *Stroke* **40,** 1820–1826. ISSN: 0039-2499, 1524-4628 (May 1, 2009).

165. Urback, A. L., MacIntosh, B. J. & Goldstein, B. I. Cerebrovascular reactivity measured by functional magnetic resonance imaging during breath-hold challenge: A systematic review. *Neuroscience & Biobehavioral Reviews* **79,** 27–47. ISSN: 0149-7634 (Aug. 1, 2017).

166. Sleight, E., Stringer, M. S., Marshall, I., Wardlaw, J. M. & Thrippleton, M. J. Cerebrovascular Reactivity Measurement Using Magnetic Resonance Imaging: A Systematic Review. *Frontiers in Physiology* **12,** 643468. ISSN: 1664-042X (Feb. 25, 2021).

167. Gupta, A. *et al.* Oxygen Extraction Fraction and Stroke Risk in Patients with Carotid Stenosis or Occlusion: A Systematic Review and Meta-Analysis. *American Journal of Neuroradiology* **35.** Publisher: American Journal of Neuroradiology Section: Brain, 250–255. ISSN: 0195-6108, 1936-959X (Feb. 1, 2014).

168. Grubb Robert L., J. *et al.* Importance of Hemodynamic Factors in the Prognosis of Symptomatic Carotid Occlusion. *JAMA* **280,** 1055–1060. ISSN: 0098-7484 (Sept. 23, 1998).

169. Molinari, F., Liboni, W., Grippi, G. & Negri, E. Relationship between oxygen supply and cerebral blood flow assessed by transcranial Doppler and near – infrared spectroscopy in healthy subjects during breath – holding. *Journal of NeuroEngineering and Rehabilitation* **3,** 16. ISSN: 1743-0003 (July 19, 2006).

170. Holper, L., Scholkmann, F. & Seifritz, E. Prefrontal hemodynamic after-effects caused by rebreathing may predict affective states – A multimodal functional near-infrared spectroscopy study. *Brain Imaging and Behavior* **11,** 461–472. ISSN: 1931-7565 (Apr. 1, 2017).

171. Vagné, V. *et al.* Quantitative assessment of near-infrared spectroscopy time course under hypercapnia using an a priori model-based fitting. *Computers in Biology and Medicine* **118,** 103638. ISSN: 0010-4825 (Mar. 1, 2020).

172. Zirak, P., Delgado-Mederos, R., Martí-Fàbregas, J. & Durduran, T. Effects of acetazolamide on the micro- and macro-vascular cerebral hemodynamics: a diffuse optical and transcranial doppler ultrasound study. *Biomedical Optics Express* **1.** Publisher: Optical Society of America, 1443–1459. ISSN: 2156-7085 (Dec. 1, 2010).

173. Markus, H. S. & Harrison, M. J. Estimation of cerebrovascular reactivity using transcranial Doppler, including the use of breath-holding as the vasodilatory stimulus. *Stroke* **23.** Publisher: American Heart Association, 668–673 (May 1, 1992).

174. Müller, M., Voges, M., Piepgras, U. & Schimrigk, K. Assessment of Cerebral Vasomotor Reactivity by Transcranial Doppler Ultrasound and Breath-Holding. *Stroke* **26.** Publisher: American Heart Association, 96–100 (Jan. 1, 1995).

175. Nakagawa, I. *et al.* Hyperventilation and breath-holding test with indocyanine green kinetics predicts cerebral hyperperfusion after carotid artery stenting. *Journal of Cerebral Blood Flow & Metabolism* **39,** 901–912. ISSN: 0271-678X (May 2019).

176. Smielewski, P., Czosnyka, M., Pickard, J. D. & Kirkpatrick, P. Clinical Evaluation of Near-Infrared Spectroscopy for Testing Cerebrovascular Reactivity in Patients With Carotid Artery Disease. *Stroke* **28,** 331–338. ISSN: 0039-2499, 1524-4628 (Feb. 1, 1997).

177. Vasdekis, S. N. *et al.* Cerebrovascular reacivity assessment in patients with carotid artery disease: a combined TCD and NIRS study. *Journal of Neuroimaging: Official Journal of the American Society of Neuroimaging* **22,** 261–265. ISSN: 1552-6569 (July 2012).

178. Vernieri, F. *et al.* Hemoglobin oxygen saturation as a marker of cerebral hemodynamics in carotid artery occlusion. *Journal of Neurology* **253,** 1459–1465. ISSN: 1432-1459 (Nov. 1, 2006).

179. Zirak, P., Delgado-Mederos, R., Dinia, L., Martí-Fàbregas, J. & Durduran, T. Microvascular versus Macrovascular Cerebral Vasomotor Reactivity in Patients with Severe Internal Carotid Artery Stenosis or Occlusion. *Academic Radiology* **21,** 168–174. ISSN: 1076-6332 (2014).

180. Reinhard, M., Rutsch, S. & Hetzel, A. Cerebral autoregulation in acute ischemic stroke. *Perspectives in Medicine* **1,** 194–197. ISSN: 2211-968X (Sept. 1, 2012).

181. Reinhard, M. *et al.* Oscillatory cerebral hemodynamics—the macro- vs. microvascular level. *Journal of the Neurological Sciences* **250,** 103–109. ISSN: 0022-510X (Dec. 1, 2006).

182. Smielewski, P., Czosnyka, M., Pickard, J. D. & Kirkpatrick, P. Assessment of cerebrovascular reactivity in patients with carotid artery disease using near-infrared spectroscopy. *Acta Neurochirurgica. Supplement* **71,** 263–265. ISSN: 0065-1419 (1998).

183. Reinhard, M. *et al.* Spatial mapping of dynamic cerebral autoregulation by multichannel near-infrared spectroscopy in high-grade carotid artery disease. *Journal of Biomedical Optics* **19.** Publisher: SPIE, 097005. ISSN: 1083-3668, 1560-2281 (Sept. 2014).

184. Norrving, B., Nilsson, B. & Risberg, J. rCBF in patients with carotid occlusion. Resting and hypercapnic flow related to collateral pattern. *Stroke* **13.** Publisher: American Heart Association, 155–162 (Mar. 1, 1982).

185. Tsivgoulis, G., Sharma, V. K., Lao, A. Y., Malkoff, M. D. & Alexandrov, A. V. Validation of Transcranial Doppler With Computed Tomography Angiography in Acute Cerebral Ischemia. *Stroke* **38.** Publisher: American Heart Association, 1245–1249 (Apr. 1, 2007).

186. Demchuk, A. M. *et al.* Specific Transcranial Doppler Flow Findings Related to the Presence and Site of Arterial Occlusion. *Stroke* **31.** Publisher: American Heart Association, 140–146 (Jan. 1, 2000).

187. Zhu, G., Yuan, Q., Yang, J. & Yeo, J. H. The role of the circle of Willis in internal carotid artery stenosis and anatomical variations: a computational study based on a patient-specific three-dimensional model. *BioMedical Engineering OnLine* **14,** 107. ISSN: 1475-925X (Nov. 25, 2015).

188. Fang, H. *et al.* Compensatory patterns of collateral flow in stroke patients with unilateral and bilateral carotid stenosis. *BMC Neurology* **16,** 39. ISSN: 1471-2377 (Mar. 18, 2016).

189. Fukunaga, M. *et al.* Large-amplitude, spatially correlated fluctuations in BOLD fMRI signals during extended rest and early sleep stages. *Magnetic Resonance Imaging* **24,** 979–992. ISSN: 0730-725X (2006).

190. Greicius, M. D. *et al.* Persistent default-mode network connectivity during light sedation. *Human Brain Mapping* **29.** _eprint: https://onlinelibrary.wiley.com/doi/pdf/10.1002/hbm.20537, 839–847. ISSN: 1097-0193 (2008).

191. Picchioni, D. *et al.* Infraslow EEG oscillations organize large-scale cortical–subcortical interactions during sleep: A combined EEG/fMRI study. *Brain Research* **1374,** 63–72. ISSN: 0006-8993 (2011).

192. Vanhatalo, S. *et al.* Infraslow oscillations modulate excitability and interictal epileptic activity in the human cortex during sleep. *Proceedings of the National Academy of Sciences* **101.** Publisher: National Academy of Sciences Section: Biological Sciences, 5053–5057. ISSN: 0027-8424, 1091-6490 (Apr. 6, 2004).

193. Gupta, L. *et al.* Towards prognostic biomarkers from BOLD fluctuations to differentiate a first epileptic seizure from new-onset epilepsy. *Epilepsia* **58.** _eprint: https://onlinelibrary.wiley.com/doi 476–483. ISSN: 1528-1167 (2017).

194. Malliani, A., Pagani, M. & Lombardi, F. Physiology and clinical implications of variability of cardiovascular parameters with focus on heart rate and blood pressure. *American Journal of Cardiology* **73.** ZSCC: 0000164 Publisher: Elsevier, C3–C9. ISSN: 0002-9149, 1879-1913 (Apr. 7, 1994).

195. Lundberg, N. Continuous recording and control of ventricular fluid pressure in neurosurgical practice. *Acta Psychiatrica Scandinavica. Supplementum* **36.** ZSCC: 0001730, 1–193. ISSN: 0065-1591 (1960).

196. Obrig, H. *et al.* Spontaneous Low Frequency Oscillations of Cerebral Hemodynamics and Metabolism in Human Adults. *NeuroImage* **12,** 623–639. ISSN: 1053-8119 (2000).

197. Buzsáki, G. & Draguhn, A. Neuronal Oscillations in Cortical Networks. *Science* **304.** ZSCC: 0005214 Publisher: American Association for the Advancement of Science Section: Review, 1926–1929. ISSN: 0036-8075, 1095-9203 (June 25, 2004).

198. Katura, T., Tanaka, N., Obata, A., Sato, H. & Maki, A. Quantitative evaluation of interrelations between spontaneous low-frequency oscillations in cerebral hemodynamics and systemic cardiovascular dynamics. *NeuroImage* **31.** ZSCC: 0000162, 1592–1600. ISSN: 1053-8119 (July 15, 2006).

199. Sassaroli, A., Pierro, M., Bergethon, P. R. & Fantini, S. Low-Frequency Spontaneous Oscillations of Cerebral Hemodynamics Investigated With Near-Infrared Spectroscopy: A Review. *IEEE Journal of Selected Topics in Quantum Electronics* **18.** ZSCC: 0000050 Conference Name: IEEE Journal of Selected Topics in Quantum Electronics, 1478–1492. ISSN: 1558-4542 (July 2012).

200. Schytz, H. W. *et al.* Spontaneous Low-Frequency Oscillations in Cerebral Vessels: Applications in Carotid Artery Disease and Ischemic Stroke. *Journal of Stroke and Cerebrovascular Diseases* **19,** 465–474. ISSN: 10523057 (Nov. 2010).

201. Marshall, R. S., Asllani, I., Pavol, M. A., Cheung, Y.-K. & Lazar, R. M. Altered cerebral hemodyamics and cortical thinning in asymptomatic carotid artery stenosis. *PLoS ONE* **12,** e0189727. ISSN: 1932-6203 (Dec. 14, 2017).

202. Asllani, I. *et al.* Measurement of cortical thickness asymmetry in carotid occlusive disease. *NeuroImage : Clinical* **12,** 640–644. ISSN: 2213-1582 (Sept. 19, 2016).

203. Cohen, A. D. *et al.* Improving the Breath-Holding CVR Measurement Using the Multiband Multi-Echo EPI Sequence. *Frontiers in Physiology* **12.** ISSN: 1664-042X. doi:10/gn6q8w. <https://www.frontiersin.org/article/10.3389/fphys.2021.619714> (visited on 01/18/2022) (2021).

204. Diehl, R. R., Diehl, B., Sitzer, M. & Hennerici, M. Spontaneous oscillations in cerebral blood flow velocity in normal humans and in patients with carotid artery disease. *Neuroscience Letters* **127,** 5–8. ISSN: 0304-3940 (June 10, 1991).

205. Fox, M. D. & Raichle, M. E. Spontaneous fluctuations in brain activity observed with functional magnetic resonance imaging. *Nature Reviews Neuroscience* **8.** Bandiera_abtest: a Cg_type: Nature Research Journals Number: 9 Primary_atype: Reviews Publisher: Nature Publishing Group, 700–711. ISSN: 1471-0048 (Sept. 2007).

206. Porcu, M. *et al.* Reorganization of brain networks following carotid endarterectomy: an exploratory study using resting state functional connectivity with a focus on the changes in Default Mode Network connectivity. *European Journal of Radiology* **110,** 233–241. ISSN: 0720-048X (Jan. 1, 2019).

207. Drew, P. J., Mateo, C., Turner, K. L., Yu, X. & Kleinfeld, D. Ultra-slow Oscillations in fMRI and Resting-State Connectivity: Neuronal and Vascular Contributions and Technical Confounds. *Neuron* **107,** 782–804. ISSN: 0896-6273 (2020).

208. Schaeffer, S. & Iadecola, C. Revisiting the neurovascular unit. *Nature Neuroscience* **24,** 1198–1209. ISSN: 1546-1726 (Sept. 2021).

209. Novi, S. L., Rodrigues, R. B. M. L. & Mesquita, R. C. Resting state connectivity patterns with near-infrared spectroscopy data of the whole head. *Biomedical Optics Express* **7.** ZSCC: 0000020 Publisher: Optical Society of America, 2524–2537. ISSN: 2156-7085 (July 1, 2016).

210. Carbonell, F., Bellec, P. & Shmuel, A. Global and System-Specific Resting-State fMRI Fluctuations Are Uncorrelated: Principal Component Analysis Reveals Anti-Correlated Networks. *Brain Connectivity* **1,** 496–510. ISSN: 2158-0014 (Dec. 2011).

211. Aasted, C. M. *et al.* Anatomical guidance for functional near-infrared spectroscopy: AtlasViewer tutorial. *Neurophotonics* **2,** 020801. ISSN: 2329-423X, 2329-4248 (May 2015).

212. Johns Hopkins, U. o. M. *Johns Hopkins Coronavirus Resource Center.* Johns Hopkins Coronavirus Resource Center. <`https://coronavirus.jhu.edu/`> (2021).

213. WHO. COVID-19 Public Health Emergency of International Concern (PHEIC) global research and innovation forum : Publisher: UN, <`https://digitallibrary.un.org/record/3859866`> (visited on 11/18/2021) (2020).

214. Lu, R. *et al.* Genomic characterisation and epidemiology of 2019 novel coronavirus: implications for virus origins and receptor binding. *The Lancet* **395.** Publisher: Elsevier, 565–574. ISSN: 0140-6736, 1474-547X (Feb. 22, 2020).

215. Of the International, C. The species Severe acute respiratory syndrome-related coronavirus: classifying 2019-nCoV and naming it SARS-CoV-2. *Nature Microbiology* **5,** 536–544. ISSN: 2058-5276 (2020).

216. Wu, Z. & McGoogan, J. M. Characteristics of and Important Lessons From the Coronavirus Disease 2019 (COVID-19) Outbreak in China: Summary of a Report of 72314 Cases From the Chinese Center for Disease Control and Prevention. *JAMA* **323,** 1239–1242. ISSN: 0098-7484 (Apr. 7, 2020).

217. Omer, S. B., Malani, P. & del Rio, C. The COVID-19 Pandemic in the US: A Clinical Update. *JAMA* **323,** 1767–1768. ISSN: 0098-7484 (May 12, 2020).

218. Richardson, S. *et al.* Presenting Characteristics, Comorbidities, and Outcomes Among 5700 Patients Hospitalized With COVID-19 in the New York City Area. *JAMA* **323,** 2052–2059. ISSN: 0098-7484 (May 26, 2020).

219. Ortiz-Prado, E. *et al.* Clinical, molecular, and epidemiological characterization of the SARS-CoV-2 virus and the Coronavirus Disease 2019 (COVID-19), a comprehensive literature review. *Diagnostic Microbiology and Infectious Disease* **98,** 115094. ISSN: 0732-8893 (Sept. 1, 2020).

220. Wu, C. *et al.* Risk Factors Associated With Acute Respiratory Distress Syndrome and Death in Patients With Coronavirus Disease 2019 Pneumonia in Wuhan, China. *JAMA Internal Medicine* **180,** 934–943. ISSN: 2168-6106 (July 1, 2020).

221. Agrifoglio, A. *et al.* Acute respiratory distress syndrome - the Berlin definition: impact on an ICU of a university hospital. *Critical Care* **17,** P94. ISSN: 1364-8535 (Mar. 19, 2013).

222. Huang, C. *et al.* Clinical features of patients infected with 2019 novel coronavirus in Wuhan, China. *The Lancet* **395,** 497–506. ISSN: 0140-6736 (Feb. 15, 2020).

223. Guan, W.-j. *et al.* Clinical Characteristics of Coronavirus Disease 2019 in China. *New England Journal of Medicine* **382.** Publisher: Massachusetts Medical Society _eprint: https://doi.org/10.105 1708–1720. ISSN: 0028-4793 (Apr. 30, 2020).

224. Zhou, F. *et al.* Clinical course and risk factors for mortality of adult inpatients with COVID-19 in Wuhan, China: a retrospective cohort study. *The Lancet* **395,** 1054–1062. ISSN: 0140-6736 (Mar. 28, 2020).

225. Poston, J. T., Patel, B. K. & Davis, A. M. Management of Critically Ill Adults With COVID-19. *JAMA* **323,** 1839–1841. ISSN: 0098-7484 (May 12, 2020).

226. Rubenfeld, G. D. *et al.* Incidence and Outcomes of Acute Lung Injury. *New England Journal of Medicine* **353.** Publisher: Massachusetts Medical Society _eprint: https://doi.org/10.1056/NEJMoa0 1685–1693. ISSN: 0028-4793 (Oct. 20, 2005).

227. Mikkelsen, M. E. *et al.* THE EPIDEMIOLOGY OF ACUTE RESPIRATORY DISTRESS SYNDROME IN PATIENTS PRESENTING TO THE EMERGENCY DEPARTMENT WITH SEVERE SEPSIS. *Shock (Augusta, Ga.)* **40,** 375–381. ISSN: 1073-2322 (Nov. 2013).

228. Bienvenu, O. J. *et al.* Depressive Symptoms and Impaired Physical Function after Acute Lung Injury. *American Journal of Respiratory and Critical Care Medicine* **185.** Publisher: American Thoracic Society - AJRCCM, 517–524. ISSN: 1073-449X (Mar. 1, 2012).

229. Linko, R. *et al.* One-year mortality, quality of life and predicted life-time cost-utility in critically ill patients with acute respiratory failure. *Critical Care* **14,** R60. ISSN: 1364-8535 (Apr. 12, 2010).

230. Orbegozo Cortés, D. *et al.* Microvascular reactivity is altered early in patients with acute respiratory distress syndrome. *Respiratory Research* **17,** 59. ISSN: 1465-993X (May 17, 2016).

231. Azevedo, L. C. *et al.* Clinical outcomes of patients requiring ventilatory support in Brazilian intensive care units: a multicenter, prospective, cohort study. *Critical Care* **17,** R63. ISSN: 1364-8535 (Apr. 4, 2013).

232. Thille, A. W. *et al.* Chronology of histological lesions in acute respiratory distress syndrome with diffuse alveolar damage: a prospective cohort study of clinical autopsies. *The Lancet Respiratory Medicine* **1,** 395–401. ISSN: 2213-2600 (July 1, 2013).

233. Orfanos, S. E., Mavrommati, I., Korovesi, I. & Roussos, C. in *Applied Physiology in Intensive Care Medicine* (eds Pinsky, M. R., Brochard, L. & Mancebo, J.) 171–183 (Springer, Berlin, Heidelberg, 2006). ISBN: 978-3-540-37363-6. doi:10.1007/3-540-37363-2_30. <https://doi.org/10.1007/3-540-37363-2_30> (visited on 11/19/2021).

234. Cross, L. J. M. & Matthay, M. A. Biomarkers in Acute Lung Injury: Insights into the Pathogenesis of Acute Lung Injury. *Critical Care Clinics* **27.** Publisher: Elsevier, 355–377. ISSN: 0749-0704, 1557-8232 (Apr. 1, 2011).

235. Moussa, M. D. *et al.* Evaluation of endothelial damage in sepsis-related ARDS using circulating endothelial cells. *Intensive Care Medicine* **41,** 231–238. ISSN: 1432-1238 (Feb. 1, 2015).

236. De Backer, D., Donadello, K. & Cortes, D. O. Monitoring the microcirculation. *Journal of Clinical Monitoring and Computing* **26,** 361–366. ISSN: 1573-2614 (Oct. 1, 2012).

237. De Backer, D. & Durand, A. Monitoring the microcirculation in critically ill patients. *Best Practice & Research Clinical Anaesthesiology. Hemodynamic Monitoring Devices* **28,** 441–451. ISSN: 1521-6896 (Dec. 1, 2014).

238. Parežnik, R., Knezevic, R., Voga, G. & Podbregar, M. Changes in muscle tissue oxygenation during stagnant ischemia in septic patients. *Intensive Care Medicine* **32,** 87–92. ISSN: 1432-1238 (Jan. 1, 2006).

239. Gómez, H. *et al.* Use of non-invasive NIRS during a vascular occlusion test to assess dynamic tissue O2 saturation response. *Intensive Care Medicine* **34,** 1600. ISSN: 1432-1238 (June 4, 2008).

240. Bezemer, R., Lima, A., Klijn, E., Bakker, J. & Ince, C. Assessment of tissue oxygen saturation during a vascular occlusion test using near-infrared spectroscopy: role of the probe spacing and measurement site studied in healthy volunteers. *Critical Care* **13,** P244. ISSN: 1364-8535 (Mar. 13, 2009).

241. Van Beekvelt, M. C. P., Colier, W. N. J. M., Wevers, R. A. & Van Engelen, B. G. M. Performance of near-infrared spectroscopy in measuring local O2 consumption and blood flow in skeletal muscle. *Journal of Applied Physiology* **90.** Publisher: American Physiological Society, 511–519. ISSN: 8750-7587 (Feb. 1, 2001).

242. Bopp, C. M., Townsend, D. K. & Barstow, T. J. Characterizing near-infrared spectroscopy responses to forearm post-occlusive reactive hyperemia in healthy subjects. *European Journal of Applied Physiology* **111,** 2753. ISSN: 1439-6327 (Mar. 16, 2011).

243. ClinicalTrials.gov. *Identifier NCT04689477 and NCT04692129* <`https://clinicaltrials.gov/`> (2021).

244. Cortese, L. *et al.* Performance Assessment of a Commercial Continuous-Wave Near-Infrared Spectroscopy Tissue Oximeter for Suitability for Use in an International, Multi-Center Clin-

ical Trial. *Sensors* **21.** Number: 21 Publisher: Multidisciplinary Digital Publishing Institute, 6957 (Jan. 2021).

245. Rice, T. W. *et al.* Comparison of the Spo2/Fio2 Ratio and the Pao2/Fio2 Ratio in Patients With Acute Lung Injury or ARDS. *Chest* **132,** 410–417. ISSN: 0012-3692 (Aug. 1, 2007).

246. Fernández, S. *et al.* Distinctive Biomarker Features in the Endotheliopathy of COVID-19 and Septic Syndromes. *Shock (Augusta, Ga.)* **57,** 95–105. ISSN: 1073-2322 (Jan. 2022).

247. Calabretta, E. *et al.* COVID-19-induced endotheliitis: emerging evidence and possible therapeutic strategies. *British Journal of Haematology* **193.** _eprint: https://onlinelibrary.wiley.com/doi/pdf 43–51. ISSN: 1365-2141 (2021).

248. Dirican, A., Ildir, S., Uzar, T., Karaman, I. & Ozkaya, S. The role of endotheliitis in COVID-19: Real-world experience of 11 190 patients and literature review for a pathophysiological map to clinical categorisation. *International Journal of Clinical Practice* **75.** _eprint: https://onlinelibrary.wiley.com/doi/pdf/10.1111/ijcp.14843, e14843. ISSN: 1742-1241 (2021).

249. Mesquida, J. *et al.* Peripheral microcirculatory alterations are associated with the severity of acute respiratory distress syndrome in COVID-19 patients admitted to intermediate respiratory and intensive care units. *Critical Care* **25,** 381. ISSN: 1364-8535 (Nov. 8, 2021).

250. Forti, R. M. *et al.* Real-Time Non-invasive Assessment of Cerebral Hemodynamics With Diffuse Optical Spectroscopies in a Neuro Intensive Care Unit: An Observational Case Study. *Frontiers in Medicine* **7,** 147. ISSN: 2296-858X (2020).

251. Dragojević, T. *et al.* Compact, multi-exposure speckle contrast optical spectroscopy (SCOS) device for measuring deep tissue blood flow. *Biomedical Optics Express* **9,** 322–334. ISSN: 2156-7085 (Dec. 20, 2017).

252. Bi, R., Dong, J. & Lee, K. Multi-channel deep tissue flowmetry based on temporal diffuse speckle contrast analysis. *Optics Express* **21.** Publisher: Optica Publishing Group, 22854–22861. ISSN: 1094-4087 (Sept. 23, 2013).

Appendix A

Summary result of time delay

This appendix contains a summary of all carotid artery stenosis time delay results.

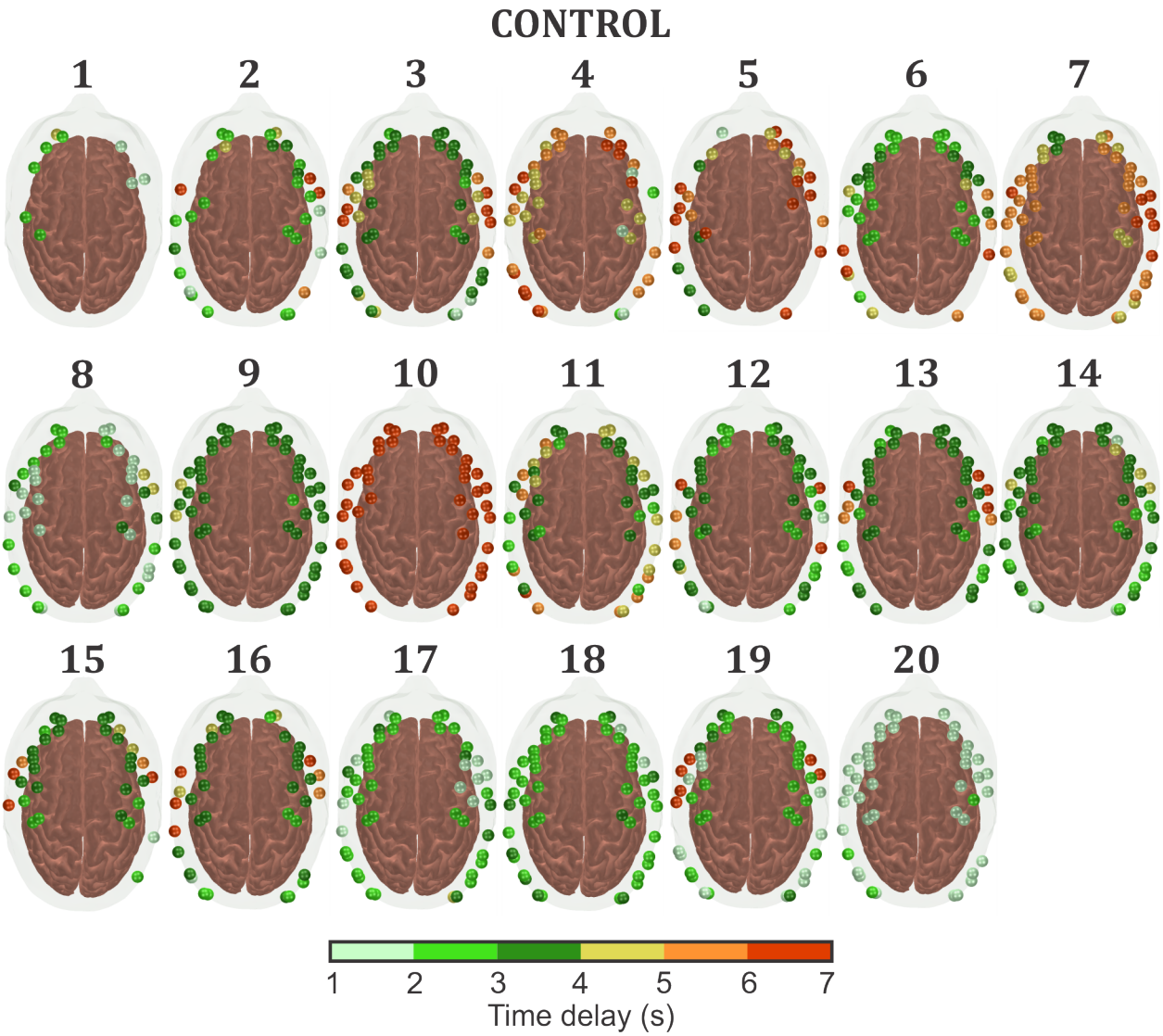

Figure A.1: **Control responses to the breath-holding** challenge from all subjects. Each sphere on the head represents a NIRS channel that showed a significant vasodilatory response (as measured by a significant increase in HbT) following apnea. The color bar represents the time delays of the modeled HRF that maximizes the fit of the measured time courses

Figure A.2: **Unilateral responses to the breath-holding** challenge from all subjects. Each sphere on the head represents a NIRS channel that showed a significant vasodilatory response (as measured by a significant increase in HbT) following apnea. The color bar represents the time delays of the modeled HRF that maximizes the fit of the measured time courses

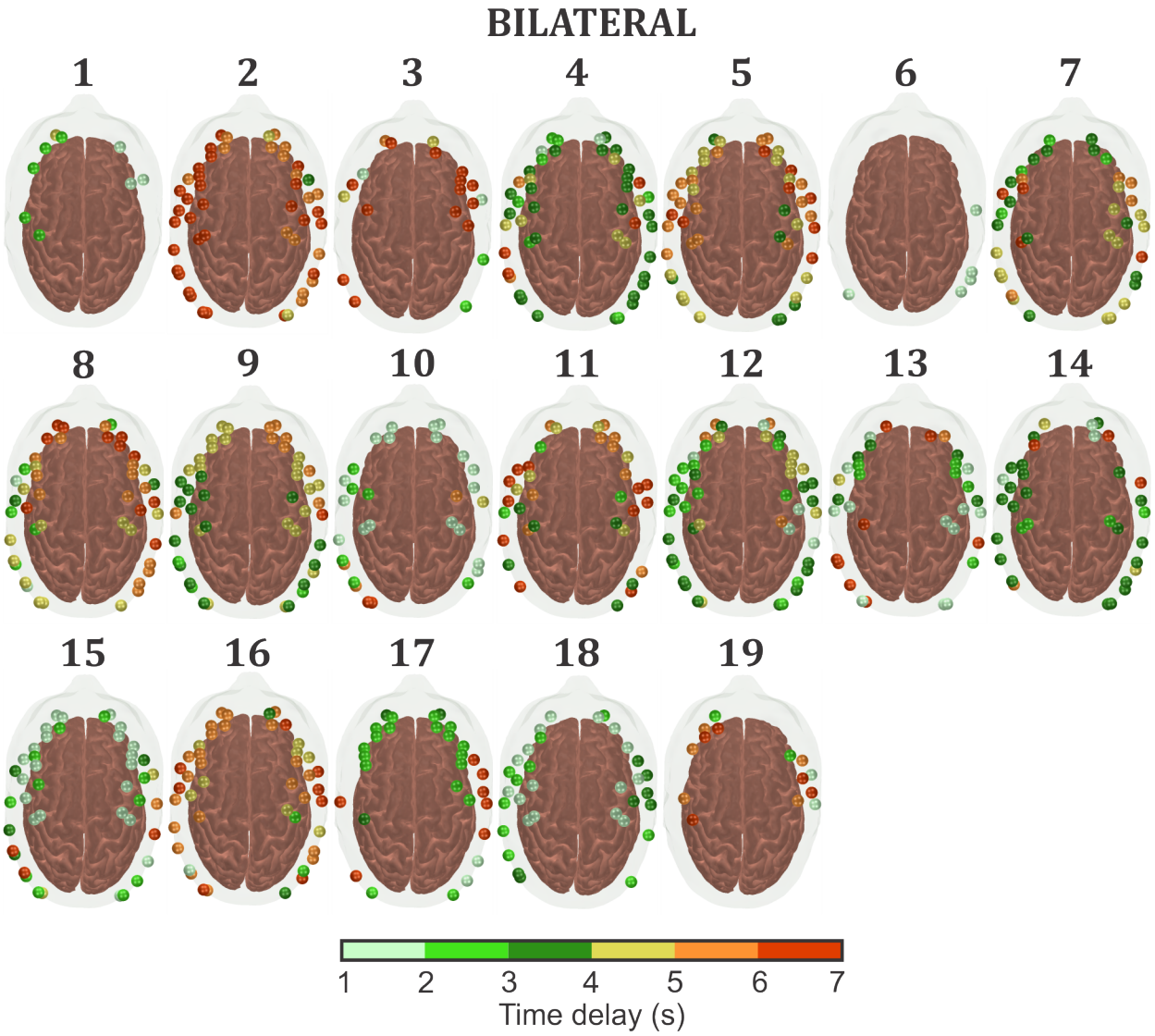

Figure A.3: **Bilateral responses to the breath-holding** challenge from all subjects. Each sphere on the head represents a NIRS channel that showed a significant vasodilatory response (as measured by a significant increase in HbT) following apnea. The color bar represents the time delays of the modeled HRF that maximizes the fit of the measured time courses

Appendix B

Consent of Carotid Stenosis project

TERMO DE CONSENTIMENTO LIVRE E ESCLARECIDO

Projeto: Avaliação hemodinâmica em pacientes com doença carotídea baseada em técnicas ópticas de difusão.

CAAE: 31592420.3.0000.5404

Pesquisadores: *Andrés F. Q. Soto, Rodrigo M. Forti, Sérgio L. Novi Jr., Giovani G. Martins, G. F. D. Leite, L. F. Bortoletto, Wagner M. Avelar, Alessandro A. V. Oliveira e Sousa, Martin A. G. A. Geiger, Alex A. Cantador, Ana T. Guillaumon, Rickson C. Mesquita.*

Você está sendo convidado a participar como voluntário de uma pesquisa clínica. A participação não é obrigatória, e não haverá nenhum tipo de penalização ou prejuízo se você não aceitar participar ou retirar sua autorização em qualquer momento. Após aceitar, você poderá desistir durante qualquer etapa da pesquisa. Para garantir seus direitos como participante, o pesquisador fornecerá todas as informações necessárias através deste documento chamado "Termo de Consentimento Livre e Esclarecido", o qual será elaborado em duas vias, ambas assinadas por você e pelo pesquisador. Ao finalizar os esclarecimentos, uma via assinada será entregue para cada parte.

Por favor, leia com atenção e calma, aproveitando para esclarecer suas dúvidas. Se houver perguntas antes ou mesmo depois de assiná-lo, você poderá esclarecê-las com o pesquisador. Se preferir, pode levar este Termo com você para consultar seus familiares ou outras pessoas antes de decidir participar.

Justificativa e objetivos:
A finalidade geral desta pesquisa é entender como a doença de estenose carotídea afeta o funcionamento cerebral, e como este eventual problema no funcionamento cerebral pode ser medido com uma técnica óptica de baixo custo. O estudo poderá fornecer novas informações fisiológicas aos médicos, o que tem grande potencial para melhorar os procedimentos clínicos.

As técnicas ópticas utilizadas neste estudo são conhecidas geralmente como NIRS (Espectroscopia do infravermelho próximo) e DCS (espectroscopia de correlação de difusão). O exame NIRS/DCS usa luz infravermelha para inferir informações sobre as mudanças da oxigenação e fluxo sanguíneo no cérebro.

Procedimentos:
Aceitando a participação no estudo, usaremos suas informações para encaixá-lo no grupo alvo ou no grupo controle. Dependendo da sua condição clínica, você poderá ser convidado para realizar o exame óptico até quatro (4) vezes durante as consultas e os procedimentos de rotina do seu tratamento ou visita com o médico. Se houver a possibilidade de interferência na rotina clínica o exame óptico será cancelado. Deste modo o pesquisador poderá consultar seus exames e histórico clínico através de seu prontuário médico fornecido pelo hospital e estabelecerá o número de participações, porém, não será feita nenhuma convocação adicional em datas e horários fora dos atendimentos do paciente. Caso necessário, algumas informações serão confirmadas diretamente com você ou seu acompanhante. Não será necessária a hospitalização para a realização do estudo.

O procedimento de estudo a ser realizado é semelhante à preparação para um exame de eletroencefalografia (EEG). O pesquisador colocará uma touca na sua cabeça, ajustada no

Rubrica do pesquisador: _____ Rubrica do participante: _____

pescoço. Em seguida, o pesquisador moverá o cabelo de modo a limpar os orifícios da toca, e em então, um conjunto de fibras ópticas para iluminar e/ou coletar a luz infravermelha será posicionado. A luz utilizada não produz nenhum risco à saúde. A touca e as fibras ópticas poderão causar um certo desconforto, mas serão reajustadas caso o desconforto seja excessivo. Se, após o ajuste, o desconto ainda for muito grande, as fibras serão removidas e o estudo será finalizado. Durante o estudo também utilizaremos aparelhos clínicos para medir sua pressão arterial, concentração de CO_2 expirado e velocidade do fluxo sanguíneo nas artérias cerebrais. Ao final da etapa de preparação, os pesquisadores apresentarão as instruções do exame.

O exame será realizado em duas etapas. Na primeira etapa você deverá permanecer em repouso, com olhos fechados, em silêncio e sem dormir por no máximo 10 minutos. Durante a segunda etapa do experimento você será indicado a segurar a sua respiração por um período de até 30 segundos, com intervalos de repouso de 90 a 120 segundos. Este protocolo poderá ser repetido até 6 vezes. O estudo terá duração de até 2 horas.

Desconfortos e riscos:
O exame NIRS tem sido usado em diferentes situações de pesquisa desde 1990, desde recém-nascidos até idosos, incluindo voluntários sadios e pacientes com distúrbios e doenças neurológicas. Não há nenhum risco previsto da técnica, pois a potência da luz utilizada é muito baixa para produzir algum dano no tecido. Além disso, a técnica NIRS não utiliza raios-X ou radiação ionizante, então não existem efeitos nocivos associados a este estudo.

Você poderá sentir um pouco de desconforto devido à pressão das fibras sobre a sua cabeça. Caso o desconforto seja grande, você poderá avisar aos pesquisadores e eles verificarão o arranjo para melhorar o conforto.

Benefícios:
Você não obterá nenhuma vantagem direta com a sua participação nesse estudo. Contudo, os resultados da pesquisa podem, a longo prazo, trazer melhorias nos diagnósticos e tratamentos clínicos para pacientes com aterosclerose de carótida, bem como melhorar nosso entendimento acerca do funcionamento vascular. Os resultados do exame ficarão à disposição caso você e/ou seu médico queira saber os resultados no futuro.

Sigilo e privacidade:
Você tem a garantia de que sua identidade será mantida em sigilo e nenhuma informação será dada a outras pessoas que não façam parte da equipe de pesquisadores. Na divulgação dos resultados desse estudo, seu nome não será citado. Os resultados do estudo poderão fazer parte do prontuário médico, mesmo que retrospectivamente.

Ressarcimento e Indenização:
Você não será reembolsado pela sua participação na pesquisa, uma vez que a mesma não vai gerar nenhum gasto. Você terá a garantia ao direito à indenização diante de eventuais danos decorrentes da pesquisa.

Contato:
Em caso de dúvidas sobre a pesquisa, você poderá entrar em contato com o pesquisador Rickson Coelho Mesquita no Laboratório de Física Médica do Hospital das Clínicas da UNICAMP, localizado na Rua Tessália Vieira de Camargo, 126, telefone (19) 3521-0137, e-mail: rickson@ifi.unicamp.br.

Rubrica do pesquisador: _____ Rubrica do participante: _____

Em caso de denúncias ou reclamações sobre sua participação e sobre questões éticas do estudo, você poderá entrar em contato com a secretaria do Comitê de Ética em Pesquisa (CEP) da UNICAMP das 08:30hs às 11:30hs e das 13:00hs as 17:00hs na Rua: Tessália Vieira de Camargo, 126; CEP 13083-887 Campinas – SP; telefone (19) 3521-8936 ou (19) 3521-7187; e-mail: cep@fcm.unicamp.br.

O Comitê de Ética em Pesquisa (CEP).

O papel do CEP é avaliar e acompanhar os aspectos éticos de todas as pesquisas envolvendo seres humanos. A Comissão Nacional de Ética em Pesquisa (CONEP), tem por objetivo desenvolver a regulamentação sobre proteção dos seres humanos envolvidos nas pesquisas. Desempenha um papel coordenador da rede de Comitês de Ética em Pesquisa (CEPs) das instituições, além de assumir a função de órgão consultor na área de ética em pesquisas.

Consentimento livre e esclarecido:

Após ter recebido esclarecimentos sobre a natureza da pesquisa, seus objetivos, métodos, benefícios previstos, potenciais riscos e o incômodo que esta possa acarretar, aceito participar e declaro estar recebendo uma via original deste documento assinada pelo pesquisador e por mim, tendo todas as folhas por nós, rubricadas:

Nome do (a) participante: _____

Contato telefônico: _____

E-mail (opcional): _____

_____ Data: ____/_____/_____.
(Assinatura do participante ou nome e assinatura do seu RESPONSÁVEL LEGAL)

Responsabilidade do Pesquisador:
Asseguro ter cumprido as exigências da resolução 466/2012 CNS/MS e complementares na elaboração do protocolo e na obtenção deste Termo de Consentimento Livre e Esclarecido. Asseguro, também, ter explicado e fornecido uma via deste documento ao participante. Informo que o estudo foi aprovado pelo CEP perante o qual o projeto foi apresentado. Comprometo-me a utilizar o material e os dados obtidos nesta pesquisa exclusivamente para as finalidades previstas neste documento ou conforme o consentimento dado pelo participante.

_____ Data: ____/_____/_____.
(Assinatura do pesquisador)

Rubrica do pesquisador: _____ Rubrica do participante: _____

Appendix C

Consent of COVID-19 project

TERMO DE CONSENTIMENTO LIVRE E ESCLARECIDO

Projeto: Caracterização não invasiva da reatividade microvascular em pacientes com COVID-19 e outras doenças respiratórias graves com a espectroscopia do infravermelho próximo

CAAE: 34454920.7.0000.5404

Pesquisadores: Rickson C. Mesquita, Rodrigo M. Forti, Andrés F. Q. Soto, Italo K. Aventurato, Gabriela Lívio Emídio, Lígia dos Santos Roceto Ratti, Antonio L. E. Falcão

Você está sendo convidado a participar como voluntário de uma pesquisa clínica. A participação não é obrigatória, e não haverá nenhum tipo de penalização ou prejuízo no tratamento se você não aceitar participar. Após aceitar, você poderá desistir durante qualquer etapa da pesquisa, também sem qualquer prejuízo. Para garantir seus direitos como participante, o pesquisador fornecerá todas as informações necessárias através deste documento chamado "Termo de Consentimento Livre e Esclarecido", o qual está elaborado em duas vias, ambas assinadas por você e pelo pesquisador. Ao finalizar os esclarecimentos, uma via assinada será entregue para cada parte. Nos casos onde houver dificuldade na obtenção da assinatura em uma cópia de papel deste termo devido à pandemia da COVID-19, este termo poderá também ser assinado digitalmente. Nos casos em que houver necessidade da assinatura digital deste termo de consentimento, ambas as partes devem salvar uma cópia impressa ou digital da versão assinada deste documento.

Por favor, leia com atenção e calma, aproveitando para esclarecer suas dúvidas. Se houver perguntas antes ou mesmo depois de assiná-lo, você poderá esclarecê-las com o pesquisador. Se preferir, pode levar este Termo com você para consultar seus familiares ou outras pessoas antes de decidir participar.

Justificativa e objetivos:
O objetivo geral deste projeto de pesquisa é introduzir e testar clinicamente um sistema não invasivo para monitorar pacientes internados em unidades de terapia intensiva (UTI) devido a síndrome respiratória aguda. O estudo poderá fornecer novas informações com grande potencial para melhorar os procedimentos clínicos, e os resultados obtidos poderão ajudar os médicos a entenderem melhor os efeitos da COVID-19 e outras doenças respiratórias agudas. A técnica utilizada neste estudo é conhecida como NIRS (Espectroscopia do infravermelho próximo), e ela usa luz infravermelha de baixa potência para medir a oxigenação no músculo.

Procedimentos:
Aceitando a participação no estudo, usaremos suas informações para termos controles sobre as variáveis que podem afetar os resultados deste estudo. Deste modo, os pesquisadores responsáveis por esse estudo terão acesso ao seu histórico clínico através do prontuário fornecido pelo hospital. Mais especificamente, antes do início de todos os testes coletaremos seus dados demográficos, os valores dos seus sinais vitais, os dados do ventilador mecânico, entre outros parâmetros clínicos. Caso necessário, algumas informações serão confirmadas diretamente com você ou seu responsável legal. Dependendo da

sua condição clínica, você poderá ser convocado para realizar o teste óptico mais de uma vez durante a sua internação. Repetiremos o teste no máximo duas vezes por dia durante o tempo que você estiver internado no hospital.

Um sensor de NIRS será posicionado no seu antebraço, juntamente com uma braçadeira para realização de um teste de oclusão vascular. O teste de oclusão vascular consiste em inflarmos a braçadeira para temporariamente obstruir o fluxo sanguíneo do braço (similar a uma medida de pressão arterial). O protocolo consiste em um período de repouso inicial de 5 minutos, seguido por um período de 3 minutos onde inflaremos a braçadeira com uma pressão acima da sua pressão arterial. O período de oclusão será seguido por um segundo período de repouso de 5 minutos. Durante o teste o você não precisará realizar nenhuma ação, e terá apenas de ficar em repouso enquanto realizamos o teste, que durará cerca de 10 a 15 minutos.

Desconfortos e riscos:
NIRS tem sido usado em diferentes situações de pesquisa desde 1990, desde recém-nascidos até idosos, incluindo voluntários sadios e pacientes com distúrbios e doenças neurológicas. Não há nenhum risco previsto da técnica, pois a potência da luz utilizada é muito baixa para produzir algum dano ao tecido. Durante o teste, você poderá sentir algum desconforto temporário devido a pressão da braçadeira. Se o desconforto for excessivo, pararemos o teste instantaneamente. Todos os testes serão realizados por profissionais da saúde, e todos os cuidados necessários para evitar a transmissão da COVID-19 serão tomados. Isto é, os profissionais da saúde estarão sempre com todos os equipamentos de proteção necessários e todos os equipamentos utilizados durante o estudo serão sempre desinfectados antes e depois de todos os testes realizados. Em caso de qualquer evento adverso relacionado à pesquisa, você terá direito a assistência médica imediata, gratuita e pelo tempo necessário.

Benefícios:
Você não obterá nenhuma vantagem direta com a sua participação nesse estudo. Contudo, os resultados da pesquisa podem, a longo prazo, trazer melhorias nos diagnósticos e tratamentos clínicos para pacientes com síndrome respiratórias aguda graves causada pelo COVID-19 e outras doenças. Os resultados do exame ficarão à disposição caso você e/ou seu médico tenham interesse no futuro.

Sigilo e privacidade:
Você tem a garantia de que sua identidade será mantida em sigilo e nenhuma informação pessoal será dada a outras pessoas que não façam parte da equipe de pesquisadores. Na divulgação dos resultados desse estudo, seu nome não será citado. Os resultados do estudo poderão fazer parte do prontuário médico, mesmo que retrospetivamente. Este estudo faz parte de uma colaboração internacional, e os dados coletados e analisados serão compartilhados com os outros parceiros, porém sempre garantindo a sua privacidade.

Ressarcimento e Indenização:
Você não será reembolsado pela sua participação na pesquisa, uma vez que a mesma não vai gerar nenhum gasto. Embora seja muito pouco provável que algum dano seja causado no decorrer da pesquisa, caso algo aconteça você terá a garantia ao direito a uma indenização diante de eventuais danos.

Contato:
Em caso de dúvidas sobre a pesquisa, você poderá entrar em contato com o pesquisador Rickson Coelho Mesquita no Laboratório de Física Médica do Hospital das Clínicas da UNICAMP, localizado na Rua Tessália Vieira de Camargo, 126, telefone (19) 3521-0137, e-mail: rickson@ifi.unicamp.br.
Em caso de denúncias ou reclamações sobre sua participação e sobre questões éticas do estudo, você poderá entrar em contato com a secretaria do Comitê de Ética em Pesquisa (CEP) da UNICAMP das 08:30hs às 11:30hs e das 13:00hs as 17:00hs na Rua: Tessália Vieira de Camargo, 126; CEP 13083-887 Campinas – SP; telefone (19) 3521-8936 ou (19) 3521-7187; e-mail: cep@fcm.unicamp.br.

O Comitê de Ética em Pesquisa (CEP):
O papel do CEP é avaliar e acompanhar os aspectos éticos de todas as pesquisas envolvendo seres humanos. A Comissão Nacional de Ética em Pesquisa (CONEP), tem por objetivo desenvolver a regulamentação sobre proteção dos seres humanos envolvidos nas pesquisas. Desempenha um papel coordenador da rede de Comitês de Ética em Pesquisa (CEPs) das instituições, além de assumir a função de órgão consultor na área de ética em pesquisas.

Consentimento livre e esclarecido:
Após ter recebido esclarecimentos sobre a natureza da pesquisa, seus objetivos, métodos, benefícios previstos, potenciais riscos e o incômodo que esta possa acarretar, aceito participar e declaro estar recebendo uma via original deste documento assinada pelo pesquisador e por mim, tendo todas as folhas por nós rubricadas:

Nome do (a) participante: _____

Contato telefônico: _____

E-mail (opcional): _____

_____ Data: ____/_____/_____.

(Assinatura do participante ou nome e assinatura do seu RESPONSÁVEL LEGAL)

Responsabilidade do Pesquisador:
Asseguro ter cumprido as exigências da resolução 466/2012 CNS/MS e complementares na elaboração do protocolo e na obtenção deste Termo de Consentimento Livre e Esclarecido. Asseguro, também, ter explicado e fornecido uma via deste documento ao participante. Informo que o estudo foi aprovado pelo CEP perante o qual o projeto foi apresentado. Comprometo-me a utilizar o material e os dados obtidos nesta pesquisa exclusivamente para as finalidades previstas neste documento ou conforme o consentimento dado pelo participante.

_____ Data: ____/_____/_____.

(Assinatura do pesquisador)